Nanostructured Materials for Solar Energy Applications

Vårin Renate Andvik Holm

Thesis for the Degree of Philosophiae Doctor (PhD)
University of Bergen, Norway
2018

UNIVERSITY OF BERGEN

Nanostructured Materials for Solar Energy Applications

Vårin Renate Andvik Holm

Thesis for the Degree of Philosophiae Doctor (PhD)
at the University of Bergen

2018

Date of defence: 23.03.2018

Year: 2018

Title: Nanostructured Materials for Solar Energy Applications

Name: Vårin Renate Andvik Holm

Print: Skipnes Kommunikasjon / University of Bergen

Contents

List of articles

All published and submitted articles are done so in international, peer reviewed journals, listed in the Web of Science and PubMed:

(A) **V. R. A. Holm**, M. M. Greve and B. Holst. A theoretical investigation of the optical properties of metal nanoparticles in water for photo thermal conversion enhancement, *Energy Conversion and Management*, **149**, pp. 536-542 (2017)

(B) **V. R. A. Holm**, M. M. Greve and B. Holst. Temperature induced color change in gold nanoparticle arrays: Investigating the annealing effect on the localized surface plasmon resonance, *Journal of Vacuum Science & Technology B, Nanotechnology and Microelectronics: Materials, Processing, Measurement, and Phenomena*, **34**, 6, p. 06K501 (2016)

(C) R. Flatabø, **V. R. A. Holm**, H. Eidsvåg, B. Holst and M. M. Greve. Light absorption and scattering of 40 - 170 nm gold nanoparticles on glass substrates, *Journal of Vacuum Science and Technology B, Nanotechnology and Microelectronics: Materials, Processing, Measurement, and Phenomena*, **35**, 6, p. 06G403 (2017)

(D) [Submitted] **V. R. A. Holm**, B. Y. Zheng, P. M. Denby, B. Holst, N. J. Halas and M. M. Greve. Work function-driven hot electron extraction in a bimetallic plasmonic MIM device, *ACS Photonics* (2017).

(E) N. Akhtar, **V. R. A. Holm**, P. J. Thomas, B. Svardal, S. H. Askeland and B. Holst. Underwater Superoleophobic Sapphire (0001) Surfaces, *The Journal of Physical Chemistry C*, **119**, 27, pp. 15333-15338 (2015)

(F) [Manuscript] M. M. Greve, **V. R. A. Holm**, B. Holst and T. Reisinger. How to design a simple, small scale, nano lithography research laboratory.

Non peer reviewed Publications:

(G) **V. R. A. Holm**. Vi er bare i startfasen, *Bergens Tidene*, p. 20 **16.07.2017**

Referee for:

(H) *Energy Conversion and Management* (2017)

List of conference presentations

(1) **V. R. A. Holm**. An all metal solar cell, Oral presentation at *The Norwegian PhD Network on Nanotechnology for Microsystems Workshop 2014*, Tønsberg, Norway (2014).

(2) **V. R. A. Holm**, R. Flatabø, M. M. Greve and B. Holst. An all metal solar cell, Poster presentation at *The NorTex Nano Summit 2014*, Houston, Texas (2014).

(3) **V. R. A. Holm**, R. Flatabø, M. M. Greve and B. Holst. University of Bergen Nano Physics Group Selected Activities, Poster presentation at *The NorTex Nano Summit 2014*, Houston, Texas (2014).

(4) **V. R. A. Holm**, M. M. Greve and B. Holst. Blue to red observation of a reversed color change in an array of gold nano particles; a systematic investigation, Poster presentation at *The Norwegian PhD Network on Nanotechnology for Microsystems Workshop 2015*, Oslo, Norway (2015).

(5) **V. R. A. Holm**, M. M. Greve and B. Holst. Investigating the cause of a color change in annealed gold nano particle arrays, Poster presentation at *The 60th Conference on Electron Ion And Photon Beam Technology And Nanofabrication 2016*, Pittsburgh, Pennsylvania (2016).

(6) **V. R. A. Holm**. Finding a nano structure on a macroscopic surface: A method for how to measure the same nano particle with an AFM and a SEM, Oral presentation *The Norwegian PhD Network on Nanotechnology for Microsystems Workshop 2016*, Trondheim, Norway (2016).

(7) **V. R. A. Holm**, M. M. Greve and B. Holst. A theoretical investigation of the optical properties of metal nanoparticles in water for photo thermal conversion enhancement, Poster presentation at *The Norwegian PhD Network on Nanotechnology for Microsystems Workshop 2017*, Bergen, Norway (2017).

Preface: Only the start

We are still making new discoveries thanks to nanotechnology research.

Let me tell you a story about a small nanosphere, who one day will live in a coat of paint on the outer wall of your house. Let's call him Noa, little naNoa. His neighbors live on the window surface, and on the roof. They live in these places because they produce electricity for you. Other nanospheres live in these same places to create beautiful colors, or to repel the water when it rains, but Noa's job is to catch sun rays and turn them into electricity. He knows that no one can create energy. It's only possible to change the energy from one form to another. This is something Noa is very good at.

When the sun's rays reach him, the electrons in his stomach tickles. Green is his favorite color. That's when the light tickles the most! In fact, it tickles so much, that the electrons jumps out of his stomach and lands on the floor below him. The floor and the ceiling in the coat of paint is made of very thin metal sheets, and when the electrons land there, they quickly glide off to the battery. Noa doesn't care that he has lost an electron, he just finds a new one in the ceiling, and continues to sunbathe.

The difference between us and Noa is that he is very small. In fact, ten million times smaller than us. Noa is only 50 nanometers long, and you need special tools to make him. Fortunately, we have such tools at the University of Bergen Nanolab. Noa won't experience the laws of physics in the same way on the nanometer-scale. Sunlight looks like huge electromagnetic waves coming towards him, and makes his electrons swing up and down. How much depends on his size.

Large waves will rock a small boat violently, but the big cruise ship laying next to it will hardly notice the waves. In a similar way, the size of the nanospheres matters a lot when it comes to how they experience light. Visible light has a wavelength of 390-700 nanometers, and some colors make the electrons swing more than others. Noa's mom likes blue, because she is a bit smaller than Noa, and his dad likes red, because he's a bit bigger. They are made of gold, but have a completely different color than a big lump of gold, because they are so small.

The electrons in Noa's stomach will experience the electric field in light the same way the little boat did in a big storm. They will swing up and down, sometimes so violently that the mooring breaks, so the electrons loose contact with the nucleus and jumps out into free space. A storm might not sound very pleasant, but making electrons swing in nanospheres can result in very efficient absorption of light. If you hold a marble up to the sun, it will make a shadow that is the same size as the marble itself. The sunlight is either absorbed or reflected at the surface. But Noa's

shadow is many times larger than himself. Effective absorption of light is a very important feature when one is going to make electricity from sunlight. Many other factors matters too; how the electricity is stored, transported and transformed is important to ensure minimum loss from energy production to the power outlet.

A solar cell such as the one Noa lives and works in is not yet available on the public market. At the University of Bergen we explore how light behave on the nanometer scale, so that one day we can make a solar cell which easily can be painted directly on the wall of your house. One thing we learned from studying the relationship between nanostructures and light, is that the surface of a material matters a lot to its appearance. But it is not just the appearance that changes for different surfaces. You can for example make a material water repellent by covering it with Noa and his friends. A surface with many small nanospheres will repel the water, making sure that the water can't settle. The lotus leaf and the lady's mantle are two examples of such surfaces.

As a soon graduating science student, the oil crisis in 2014 has caused me to wonder what my job opportunities are. What chances does a science graduate have to get a job now? According to Hegnar.no 39,000 jobs have been lost (September 2016) and they're not expected to return. Still it is the science graduates who are the first to find jobs after graduation. The oil crisis should not discourage us. There is still a huge need for scientists, especially in construction, IT, digitization, machine engineering, and fortunately for me and Noa; renewable energy. There is a shift in focus within science, not a change in the usefulness of this field of study.

Compared to other science subjects, nanotechnology is relatively new. Norway has been behind the United States and Europe in the development of nanotechnology, but has in recent years made an effort to catch up, through the Research Council's Nano2021 initiative. Today, nanotechnology is used in many other fields of expertise, for example drug delivery, where nanospheres help medicine find the sick cells, or diagnostics in the health sector, smaller hardware within IT, cosmetics, and perhaps most of all material technology, which can be used in clothing, building industry (materials become lighter and stronger), transport, energy, etc. We are still making new discoveries thanks to nanotechnology research.

It's possible that we are only in the starting phase of discovering the potential of nanotechnology. How a material is structured at the nano level matters a lot to the properties of that material. Once we get an overview of these properties, and how to manipulate them, it would not be unlikely that there won't be a single discipline left that has not been infiltrated by nanotechnology. One of the biggest challenges we have before we get to that point is how to do nanostructuring efficiently for large areas. Today there are many instruments that can create incredibly small and

advanced structures both in 2D and 3D, but it is a slow process for large areas. Maybe if more of you came here and got to know Noa and his friends, we could find out more about what they're good at?

This text was originally published in Norwegian as an article in the newspaper *Bergens Tidene*, see Appendix I.

Acknowledgments

I would like to thank a number of people who have helped making this thesis a reality.

First of all I thank my supervisors Bodil Holst and Martin M. Greve, who in my opinion make the best team a PhD student could ask for. They each have their own area of expertise, that being good administrative skills, ensuring a pleasant working environment, and assisting with technical and theoretical guidance. Combined, all the bases are covered ensuring a productive and pleasant Nanophysics group. I would also like to thank my colleagues who's been working in the group during the years I've been here, and to the Norwegian PhD Network on Nanotechnology for Microsystems for their financial support and the annual workshops.

In 2015, I was lucky to be able to exchange to Halas Nanophotonics Group at Rice University in Houston. I am very grateful to Naomi Halas for hosting me, and to Bob Y. Zheng for all his good advice. Thank you also to Sam Gottheim and Benjamin Cerjan.

In order to keep the mind sharp, the body, as well as the mind must be trained. I really appreciate Bergen diving club, Paul Joachim Thorsen and all the divers on the team for helping me with this. I am so grateful for having such a constant and reliable source of courage and self esteem, and for the people who help provide it. I also want to thank everybody at Midtown MMA Houston and the "Morgensymjing for dei Unge og Vakre" club.

Last, but not least, my family and friends deserve a big thank you for all their support. To my husband for feeding me and picking up the slack, to my parents for teaching me good values, my brothers and their families for encouraging me, and to my friends Trine, Lasse, Mads and Morten for giving me wonderful memories; thank you.

Abstract

The work presented in this thesis focuses on nanostructures, and what effect parameters like size, material, and surroundings have on their physical properties, with special emphasis on optical properties. The motivation for this thesis has been to provide foundational work, both experimentally and theoretically, for the exploration of metal nanoparticles for solar energy applications. The devices were fabricated using electron beam lithography and electron beam evaporation. Characterization and imaging were done with scanning electron microscopy and atomic force microscopy. Optical performance was measured using thin film analyzer, dark field microscopy and integrating spheres. Numerical analysis of optical behavior was done using the software Lumerical. The experimental work was done at the University of Bergen NanoStructures laboratory and at Rice University Halas Nanophotonics laboratory.

The thesis consists of six articles, which can be divided into three categories. The first, main category focuses on the optical and electrical properties of metal nanoparticles and metal nanostructures, and contains four articles. The first three articles cover theoretical investigations of the absorption properties of a nanofluid, experimental investigations of the effect of annealing on the optical properties, and the influence of fabrication methods on optical properties of metal nanoparticles. The fourth article presents a novel bimetallic metal-insulator-metal (MIM) device, where two metals with different work functions have been used to create a bias for hot-electron extraction. To the best of the authors knowledge this is the first MIM-device that does not require an external bias.

The second category concerns non-optical effects of nanosized features. It contains one article, which describes how wetting can be affected by surface treatment.

The third category has a more conceptual theme, and contains one article. It describes how to build an affordable nanoscience laboratory, which might help motivate people and local industry to develop nanotechnology in Norway and elsewhere.

Nomenclature

Abbreviations

AFM	atomic force microscopy
AM1.5	air mass 1.5
CCD	charge-coupled device
CM	contact mode
DC	direct current
DDA	discrete dipole approximation
DF	dark-field
DM	dynamic mode
EBE	electron beam evaporation
EBL	electron beam lithography
ELWD	extreme long working distance
FDFD	finite-difference frequency-domain
FDTD	finite-difference time-domain
FEM	finite element method
HCL	hole colloidal lithography
I-V	current-voltage
IR	infrared
ITO	indium-tin-oxide
KPFM	Kelvin probe force microscopy
LED	light emitting diode
LIA	lock-in amplifier
LSPR	localized surface plasmon resonance
MIM	metal-insulator-metal
MNP	metal nanoparticle
MoM	method of moments
NIR	near infrared
NREL	national renewable energy laboratory
PCI	photocurrent instrument
PEEC	partial element equivalent circuit
PML	perfectly matched layer
PV	photovoltaic
SEM	scanning electron microscope
TE	transverse electric
TFA	thin film analyzer
TFSF	total field scattered field
TM	transverse magnetic
UoB	University of Bergen
VIS	visible

Symbols

α	polarizability
β	coefficient (m^{-1})
λ	wavelength (nm)
μ	permeability (kg m s^{-2} A^{-2})
ω	angular frequency (rad s^{-1})
$\overline{Q}$	average efficiency
Φ	radiant power (Watt)
ϕ	phase

σ	cross section (nm^2)
τ	optical depth (m)
ε	permittivity (m^{-3} kg^{-1} s^4 A^2)
$\vec{D}$	displacement field (C m^2)
$\vec{E}$	electric field (kg m s^{-3} A^{-1})
$\vec{H}$	magnetic field (Am^{-1})
$\vec{S}$	surface area (m^2)
A	absorbance
A	area (nm^2)
C	amplitude
D	dose (C)
d	diameter (nm)
E	extinction
F	force (N)
f	concentration
f	focal length (mm)
g	density (g/cm^3)
I	current (A)
k	wavenumber (m^{-1})
m	mass (kg)
m	relative refractive index
N	number of particles per unit volume (m^{-3})
n	number of particles
n	refractive index
P	power (Watt)
Q	efficiency
R	reflection
r	radius (nm)
r	raw data reflectance
S	scattering
T	transmittance
t	raw data transmittance
t	time (s)
V	voltage (V)
V	volume (m^3)
w	width (nm)
x	size parameter (m)
z	path length (m)
a	aperture (μm)
eht	source acceleration voltage (kV)
W	work function (eV)

Subscripts

0	vacuum
ω	frequency
a	absorbed
abs	absorption
AC	alternating current
c	by cross section
CPD	contact potential difference
DC	direct current
e	energetic
ext	extinction
i	incident
m	surrounding medium
mnp	metal nanoparticle
np	nanoparticle
R	reflected
r	reference signal
r	relative
S	source
s	measured signal
sca	scattering
t	transmitted
v	by volume
w	by weight

Part I

Overview and summary

Chapter 1

Introduction

1.1 Thesis structure

This thesis is divided into three main parts. Part I consists of 4 chapters: introduction, theory, methods and conclusion and further work. The introduction is chapter 1, and covers the motivation and background, objectives, state of the art for nanostructures used in solar energy applications, and finally a summary of all the articles that have come out of this work (which are presented in part II). Chapter 2 discusses the theory of optics at the nano-scale, particularly numerical methods for calculating the optical behavior with an emphasis on the method used in this work. Chapter 3 presents in detail some of the methods used, such as the "home made" photocurrent instrument (PCI). Chapter 4 provide the conclusion and further work. Part II contains all the articles that have been published during this thesis work, and part III contains the appendixes.

1.2 Motivation and Background

It is becoming increasingly evident that human consumption of natural resources has become unsustainable, and that global warming is not just caused by natural fluctuations, but is a result of human pollution [1]. For future generations to thrive, it is crucial that society as a whole changes its attitudes on this subject [2]. Scientists may help motivate a shift in the energy generation industry towards renewable energy by providing more efficient and cheaper clean energy solutions.

The sun is an abundant and highly reliable source of renewable energy. Many devices already exist which are designed to harvest solar energy [3], particularly semiconductor based devices have achieved commercial success. Unfortunately, the energy and pollution associated with the production of these devices partially

negates the advantage it has of providing clean energy [4]. Furnaces with high temperatures is used in the production of pure silicon, which is the key ingredient in about 90 % of solar arrays as of 2013 [5]. It produces bi-products like coal, coke and charcoal. Other materials are also used during manufacturing, such as cadmium, lead and nickel, which are particularly toxic for the local environment when used at a large scale [6].

When comparing power generating sources, the carbon footprint and the energy pay back ratio becomes two relevant terms. The carbon footprint considers the CO_2 emission of the product, not only during operation but also from it's production, and compares it to the power it has generated. Solar photovoltaic (PV) energy has a slightly higher carbon footprint (approximately 60 grams of carbon dioxide equivalent per unit of electricity gCO_2eq/kWh) than hydro and wind power (approximately 10 gCO_2eq/kWh) which are also renewable resources, but small compared to oil and coal (800-1000 gCO_2eq/kWh) [8]. The energy payback ratio is significantly lower for solar PV than hydro and wind [6], motivating research on improved efficiency.

In order to decrease the consumption of resources and the generation of pollutants, "green nanotechnology" is proposed to replace less environmental energy harvesting methods. All though nanostructured cells are initially thought to be cleaner than semiconductor cells, the health and environmental risks associated with this new technology is not fully known. The biological impact and life-cycle of nanomaterials is not well known, nor the toxicity and long term health impact of nanomaterials. This, and the environmental impact of manufacturing must be considered [7] as research on this topic advances.

Whether nanomaterials proves to be more environmental than semiconductor based solar cells or not, they hold another definite advantage, that is that a nanostructured cell can absorb light from the entire solar spectrum, and is not limited to light with energy above the semiconductor bandgap. When a photon is absorbed in the a semiconductor based cell, an electron may be excited from the valence band across the band gap into the conduction band, only if the energy of the photon exceeds the band gap. The maximum theoretical efficiency of a single semiconductor p-n junction, called the Shockley-Queisser limit [11], is approximately 34% (assuming a band gap of 1.34 eV). Figure 1.1 shows the experimental efficiency of the best research cells since 1975 (provided by the National Renewable Energy Laboratory [9]). Figure 1.2 shows how much of the solar spectrum a silicon cell is able to convert (Figure is reproduced from reference [10]).

Contrary to semiconductor based devices, the theoretical efficiency is higher for photoelectric devices consisting of metallic nanostructures which utilize the plas-

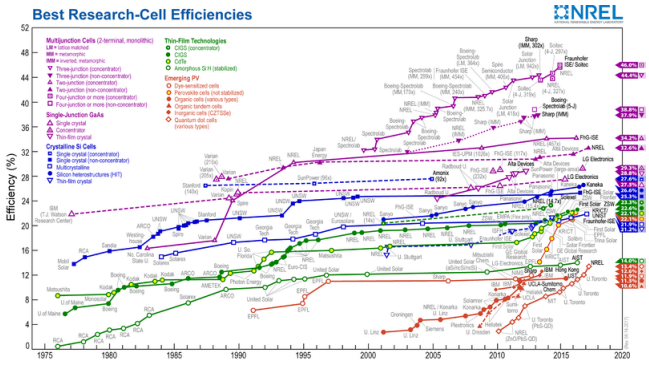

Figure 1.1: National Renewable Energy Laboratory (NREL) [9] Best Research-Cell Efficiencies.

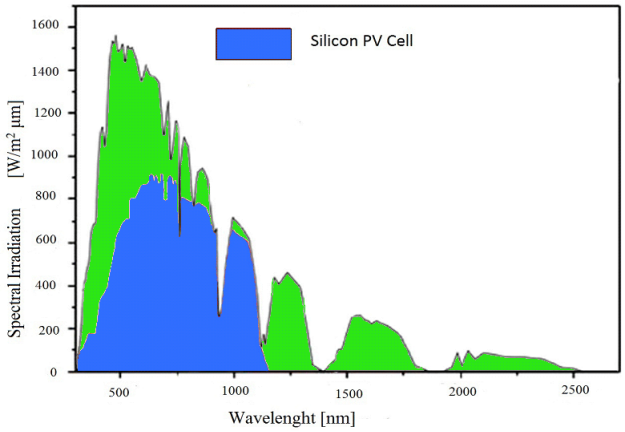

Figure 1.2: Silicon cell convertible spectrum compared with the solar spectrum (AM1.5). Figure reproduced from reference [10].

monic effect. The absorption process is not limited by a band gap, and can be tuned to absorb light at any wavelength across the whole bandwidth of the solar specter. Due to the small size of the nanostructure, the electric field of the light displaces the electrons in the structure relative to the core, which in turn establish a restoring field. This causes an oscillation which ultimately result in either absorption or scattering of the solar energy, an effect called the localized surface plasmon resonance (LSPR). The amount and wavelength of solar light being absorbed depends on factors like size, shape, material, and surrounding material. Plasmonics, and specifically LSPR is described in detail in section 2.1.

With this in mind, nanoparticles and nanostructures present a promising addition to semiconductor devices. Specific configurations are described in more detail in section 1.4. Nanostructures are potentially very efficient at light absorption through plasmonic effects, an advantageous quality to have for light harvesting devices, and a great motivation for further investigation.

1.3 Objectives

The main objective of this thesis is to investigate, experimentally and theoretically, plasmonic effects in metal nanostructures, with the ultimate aim of exploiting the LSPR of nanostructures to create solar energy harvesting devices. The work may prove useful in other applications such as photo detection/sensors and heat sensors, and shed light on the effect of surface structures and photocurrent issues.

The work presented in this thesis has mainly been done at the University of Bergen NanoStructures Laboratory, with the exception of the work described in article D, which was mostly done at Rice University Halas Nanophotonics Laboratory. Electron beam lithography (EBL) and electron beam evaporation (EBE) have been important manufacturing tools due to the precession and flexibility of patterning and thin film deposition on the nano-scale. For imaging, scanning electron microscopy (SEM) and atomic force microscopy (AFM) have been the dominant techniques. Thin film analyzer (TFA), integrating spheres, and dark-field (DF) spectroscopy were used for optical analysis, and a source meter and lock-in amplifier (LIA) were used for the electrical analysis. The fabrication methods are described in the articles with additional details given in chapter 3.

The work is based on six articles, four of which have been published, one which has been submitted, and one in manuscript form. The thesis defender Vårin R. A. Holm is first author on three of the publications. All published or submitted articles have been done so to well established journals accessible through the Web of Science and PubMed. The articles can be divided into three categories: Optical properties of nanostructures, which includes articles A-D, non-optical properties

of nanostructures, which includes article E, and a conceptual category, containing article F.

The first category of articles was originally inspired by the idea of a metal nanoparticle (MNP) based solar cell patented by the Bergen company EnSol [12]. One of the key aspects of this solar cell is that it is made entirely of metals and insulators. This eliminates the need for semiconductors, which is a material that can be costly to produce and leave hazardous bi-products, as mentioned in section 1.2. It consists of MNPs suspended in a dielectric and sandwiched between two electrodes made from different metals. The two metals have different work functions, which give rise to an electric field between them, eliminating the need for an externally applied bias. An example of how this would look is depicted in Fig. 1.3.

The four first articles investigate properties that are important for this device. Article A, named "A theoretical investigation of the optical properties of MNPs in water for photo thermal conversion enhancement" [13] takes a theoretical approach to exploring which metals and particle sizes gives the most efficient absorption, and how they can be optimized to absorb as much sunlight as possible. Simulations are done for metal spheres in water since there is an abundance of experimental results to compare to in literature. The optimization of efficiency is relevant for the EnSol patent, but also, it can be used as the basis for a simpler device: a solar thermal collector. Thermal energy devices are discussed in section 1.4.2. Article B named "Temperature induced color change in gold nanoparticle arrays: Investigating the

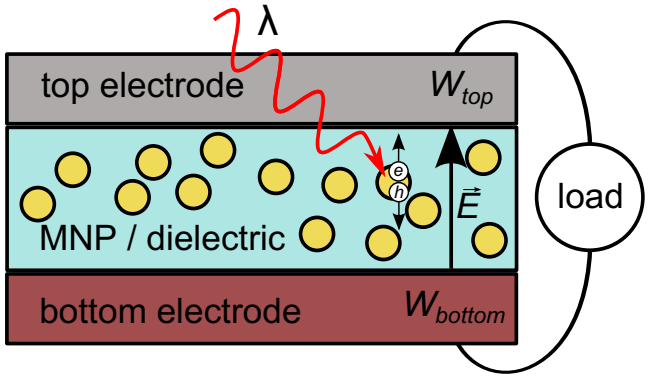

Figure 1.3: Illustration of the EnSol solar cell which inspired the work presented in articles A-D. The basic layout is seen from the side, and dimensions are not to scale. W is the work functions, $\vec{E}$ is the electric field and λ is the wavelength of the incident light. The electrons and holes are illustrated as e and h respectively.

annealing effect on the localized surface plasmon resonance" [14] examines the relationship between the shape of MNPs and the color. The article shows how very minor changes caused by annealing can lead to major color changes of nanoparticle arrays. Article C named "Light absorption and scattering of 40 - 170 nm gold nanoparticles on glass substrates" [15] investigates how the size of nanoparticles on glass substrates affect the color, and compare the results with other nanoparticles of the same size in literature. The results were also compared to nanoparticles produced with a different fabrication process. Knowing this, we are better equipped to measure hot electrons generated by absorption through LSPR, which is done in article D named "Work function-driven hot electron extraction in a bimetallic plasmonic MIM device". In this article, the plasmonic element is incorporated into a metal-insulator-metal (MIM) device made with two different metals, similar to the EnSol idea.

The second category of articles contain only article E. "Under-Water Superoleophobic Sapphire (0001) Surfaces" [16] treats a somewhat different subject matter, but has been included because it is a very nice illustration of how effects on the nanoscale can affect other macroscopic properties apart from color, in this case wetting. A cooperation with the company ProAnalysis on self cleaning windows for subsea (oil industry) applications inspired this article. It is interesting to relate how minor changes in surface topology makes such a large difference on the macro scale, whether it be in the optical, electrical or wetting properties of that material.

The third category concerns ideas relevant in nanostructure research, and consists of only one article also. Article F named "How to design a simple, small scale, nano lithography research laboratory" share some of the tactics used at University of Bergen NanoStructures laboratory to make it affordable at a low budget. The newspaper article "Vi er bare i startfasen (Only the start)" [17] is not peer-reviewed, but could also fit into this category. It is a popular-science feature article for the local newspaper *Bergens Tidene* explaining some of the work in this thesis in a language anybody can understand.

1.4 Solar Energy Applications using nanostructures: An overview of State of the Art

Before going into details of the presented articles, this section will focus on state of the art, and explore various examples, of nanostructure technology being used in solar energy applications. Solar energy is harvested for both electrical and thermal energy use, so the section is divided into these two topics. The absorption capabilities of photovoltaic (including MIM devices) and photo thermal devices can be increased by incorporating nanostructures, thus improving the power conversion

efficiencies [18], which is the common goal for energy harvesting devices.

1.4.1 Nanostructures in photovoltaic devices

Semiconductor devices

In order to absorb all the light in a semiconductor based photovoltaic device, it must be sufficiently thick. This is because the Beer-Lambert law, which reads $T = e^{-\tau}$, states that light traveling through a material decreases exponentially, and the transmittance T is determined by the optical depth τ of the material. However, too thick material layers are not good for electricity generation, as the thickness must be several times smaller than the minority carrier diffusion length. Commercial solar cells based on crystalline silicon usually have a thickness of 180-300 μm [19]. In order to decrease the cell thickness, thin film devices with plasmonic light trapping elements have been investigated. Nanoparticles or nanostructures can be used to trap light in active layers, which in turn will help decrease the thickness of the device, reducing the cost as well.

There are at least three methods for trapping light in thin film devices. The first is to place MNPs directly above the semiconductor in order to scatter and redistribute the angle of incident light, which help increase the path length of the light in the semiconductor. Research on such devices are are done by for example Schaadt et al. [20] for single crystalline silicon, and Derkacs et al. [21] and Matheu et al. [22] for amorphous silicon. The second method is to embed MNPs into the semiconductor to utilize the near field effect the nanoparticles, making use of the strong local field to absorb light at the p-n junction. In order to avoid the absorbed energy dissipating into ohmic damping in the metal, the absorption rate in the semiconductor must be larger than the reciprocal of the typical plasmon decay time, which is on the order of 10-50 fs [19]. This approach shows promising results for both organic [23] and inorganic [24, 25] solar cells. The third method is the coupling of light into surface plasmon polaritons at the metal-semiconductor interface using a nanostructured metal back surface. A 26 % enhancement in short circuit current is shown for an amorphous silicon thin film solar cell using this technique [26]. Traditional semiconductor based devices have a limited wavelength range due to the semiconductor band gap. By introducing metallic nanostructures, the working wavelength of these devices can be increased [27].

Metal-insulator-metal (MIM) devices

Metal-dielectric nanostructures are of great interest due to their optical properties [28]. An MIM device is a non-linear, rectifying device. A number of research groups have investigated MIM diodes using a variety of metals, showing that a large difference in work function of the metals yield good rectification capabilities

[29]. When combined with nanostructures, it is often refereed to as a rectenna (optical antenna and rectifier). Tailoring the nanostructure results in the desired optical response, for example high absorption for very thin films. Liu et al. reports near perfect absorption at 6 μm for their nanostructured MIM device [30]. For thin insulating layers, the LSPR will couple with the underlying metal film, affecting the optical response [31]. While the nanostructure is responsible for optical absorption and conversion to hot electrons, the MIM stack provides the rectifying element, ensuring DC current. The rectenna is reported to have a theoretical efficiency of 84% [32, 33].

The nanostructure and the MIM layers might be two different parts of the device design, such as the Au nanoparticle/Al_2O_3/Au/HfO_2/Al stack investigated by Atar et al. [34]. Alternatively, the nanostructure and MIM can be combined, such as the Ag nanostructured/SiO_2/Ag structure reported by Aydin et al. [35]. They achieved polarization independent averaged absorption of 0.71 across VIS (400-700 nm) where the MIM stack had a total thickness of 260 nm.

The energy collection of metamaterials [36] and MIM [37] devices has also been investigated. Chin et al. states that the efficiency in a rectenna is limited by the impedance matching between the nanostructure and the rectifier [33]. They also measure the asymmetry and non linearity of the current-voltage (I-V) characteristics of Nb/Nb_2O_5/X MIM devices, where X is either Cu, Ag, Nb, Ni, Au or Pt. The highest asymmetry of Pt is due to it having the highest difference in metal work functions, which is also shown by Periasamy et al. [38].

The EnSol solar cell described in section 1.3 is a MIM device with a plasmonic element. In plasmonic MIM devices hot electrons are generated by photo-illumination. If the electron energy is greater than the barrier height of the insulator, it can travel ballistically across the barrier to generate current. If the insulator is sufficiently thin, electrons with lower energy may tunnel through. Article D of this thesis is relevant to this topic. Similar to our experiments, Lee et al. investigate the hot electron flow by a MIM device, revealing a decrease in photocurrent with increasing insulator layer thickness, in their case for a Ti/TiO_2/Au structure [39]. In the case of the EnSol solar cell, one of the metal layers in the MIM structure is proposed in the patetnt [12] to be replaced by a transparent material. ITO is such a material, and in some cases it may support guided modes in the same wavelength range the structure absorbs at [40]. An example of this phenomenon is shown in Fig. 1.4 (reproduced with permission from Ref. [41]).

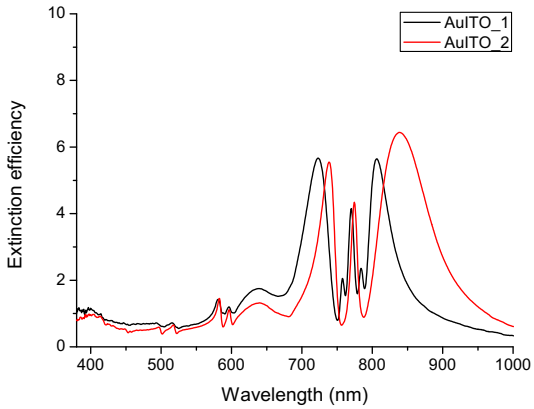

Figure 1.4: Extinction spectra of two separate samples, both with 150 diameter gold nanoparticles with 450 nm spacing on ITO, where the nanoparticles couple light into the ITO waveguide. Figure is reproduced with permission from Ref. [41].

Hot electrons

The LSPR absorbed energy, which has a lifetime of approximately 10 fs, can be transfered radiatively by re-emission of a photon or non-radiatively through the creation of hot electron-hole pairs [42]. Electrons are deemed hot when their distribution can be described by the Fermi function with an elevated effective temperature [43]. These hot electrons can be used to induce chemical reactions which otherwise would be very energetically demanding, such as water splitting [44, 45] or hydrogen dissociation [46]. Alternatively, if the electron-hole pair can be separated before they recombine, they can be extracted as current for energy harvesting [34] or photo detection [36, 47].

After being generated, hot electrons may experience electron-electron and later electron-phonon scattering, converting its energy to heat. These mechanisms contribute to determine the hot electron lifetime, which have been reported to vary between 0.05 to 1 ps [48, 49]. Manjavacas et al. shows that the exact value of the lifetime is crucial for determining the energy distribution of the hot electrons. Long lifetimes produce hot electrons with large energies. Also, smaller particles creates more energetic hot electrons than larger ones, when their lifetimes are the same. Since the total amount of energy is determined by the optical absorption, highly energetic hot electrons means a low number of electrons, and vice versa [49].

1.4.2 Nanostructures in photo thermal devices

Despite thermal energy being more utilized than electrical (456 GW thermal compared to 303 GW electrical energy world wide by the end of 2016 [50]), less attention is given to solar thermal conversion processes [27]. The reason might be because electrical energy is more widely utilized than thermal. A photo thermal device should have high absorptance and a low emittance, as the photo thermal conversion efficiency depends on these two factors. The heat can be stored and used for electricity generation when needed, eliminating the need of a battery for electricity storage [27]. It can also be used directly for heating, circumventing electricity all together in the case where electric energy is used for heating.

Photo thermal devices can consist of solid materials, or fluids. In the case of solid material, the nanostructured thermal absorbers can consist of metal/insulator composites much like the structures described in section 1.4.1, only this time the thermal heat is utilized rather than hot electrons. Two such promising configurations are presented here. The first is cement-based solar absorbers, where MNPs are embedded in a dielectric matrix, placed on a IR reflector and topped with an anti reflection coating. An example is Ni-Al_2O_3 composite reported by Craighead and Buhrman [51]. The second is multilayer absorbers, consisting of alternating metal and insulator films. For example, Barshilla et al. achieved absorptance of 0.95-0.97 and emittance between 0.06-0.08 at 82^{o}C from an aluminum/aluminum oxide multilayer absorber [52].

Nanofluid based photo thermal devices consist of absorbing fluids which incorporate nanoparticles in order to increase absorption. Water, ethylene glycol, or oils is used as the base fluid, while examples of nanoparticle materials are oxides, nitrides and metals [54]. Four photo thermal configurations are shown in Fig. 1.5 [53]. Mirrors shaped in the form of trough or dishes, or arranged as Fresnel lenses focus the light at an absorber tube (or point) containing a nanofluid. While fluids with large particles are subject to sedimentation which further cause flow resistance and erosion, the application of nanoparticles provide nanofluids with stable suspension. More interestingly, the increased surface to volume ratio of MNPs improve the heat transfer between the MNPs and fluid [55]. The heat transfer capability and the absorption efficiency of the nanofluid are ultimately what limits the photo thermal efficiency [56] of a photo thermal device. This topic is investigated in article A of this thesis. The absorption and scattering of nanoparticles of various sizes and materials suspended in water are investigated theoretically. Nanofluids can be applicable not only in photo thermal devices, but also as coolant fluids for microelectronic and other devices requiring advanced cooling [54].

Nanostructures used in thermal energy devices should be thermally stable, some-

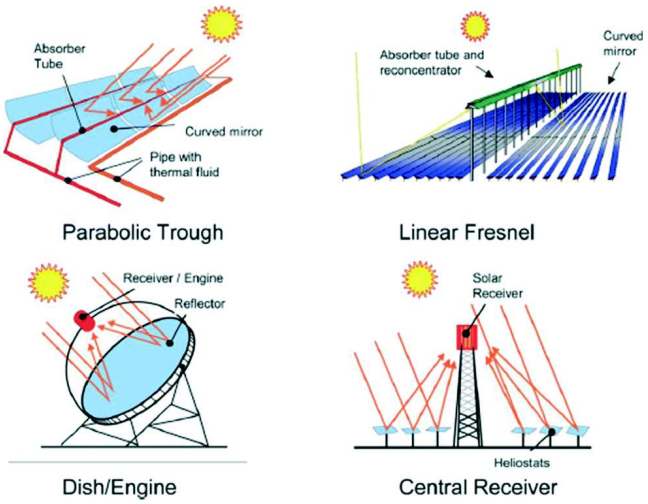

Figure 1.5: Four solar concentrating technologies: Parabolic trough collectors, linear Fresnel reflector systems, dish-engine systems, and power towers, also known as central receiver systems. The Figure is reproduced with permission from Ref. [53].

thing which is not necessarily the case. For example can the melting point of MNPs differ drastically from the bulk melting point due to increase of surface to volume ratios [57]. Bosman et al. [58] show that the extinction efficiency of nanostructures increases when annealed due to the decrease of grain boundaries, showing that heating nanostructures may be advantageous. In article B in this thesis it is shown how annealing, which causes a seemingly minute change to the nanoparticle shape, can lead to a strong change in the optical properties. Since the effect of annealing is irreversible, it is thermally stable after annealing, and it can increase the efficiency permanently.

1.5 Summary of the articles including additional work not presented in the articles

1.5.1 A theoretical investigation of the optical properties of metal nanoparticles in water for photo thermal conversion enhancement

Optical analysis carried out in this thesis was done using TFA, integrating spheres, or DF spectroscopy. But how do you know that the results are as expected? One solution is to compare the results to previously reported results in literature, though sometimes it may be hard to find someone who has built the exact same structure, and if they have, the work you do might be redundant. A better solution is to perform a theoretical investigation, through mathematical analysis or computational

simulations, and compare the results. For this reason, the commercial software package Lumerical was acquired. Details on this software is provided in the article and in section 2.2.1.

The thesis defender did all the numerical simulations and was the main writer of the manuscript with contributions to the scientific discussion from the co-authors. As the first person in our group to utilize this tool, the thesis defender was eager to create an overview of how certain parameters affected the absorption and scattering. Especially, what material and particle size will ensure the most efficient absorption in our EnSol solar cell? Though the particle there will be placed in a dielectric material, with metal films so close that they will surely couple, the choice to simulate metal spheres in water was made for two reasons. Firstly, spheres in water is a simpler system, more suited for exploring and getting to know the simulation software. Secondly, water based nanofluids have been extensively investigated in literature and can be used in many already existing systems, making experimental results to compare to abundant, and making a systematic overview of the absorption and scattering of such nanofluids useful. Most of the literature investigated in this article use concentrations in the ppm range (by volume). Concentrations in the % range can potentially present aggregation problems.

Supplementary information for this article is presented together with the article in part II. Here are two results not included in the article: Simulations of a gold sphere in water with diameter d=40 nm, and with the light source dimensions ranging from 50^2 to 300^2 nm^2 were performed, verifying that the simulation is unaffected by the source size, as long as it is larger that the cross section of the sphere itself. The results are shown in Fig. 1.6. In the article, the results show that 40 nm silver spheres are the most efficient absorber at the LSPR peak wavelength out of the tested metals, gold, silver, copper and aluminum. However, this is true only for the LSPR peak wavelength, not for all light absorbed across the spectrum.

In order to find the best total absorber, the average absorption efficiency across the wavelengths investigated are found by integration of the absorption efficiency spectrum. This is presented in Fig. 1.7. As discussed in the article, though the LSPR peak of 40 nm silver spheres is the most efficient, the peak is quite narrow, and we see that it is not the most efficient total absorber. 60 nm gold and copper spheres give the best results. Since copper is prone to oxidation, gold appears to be the choice material, when cost is not an issue.

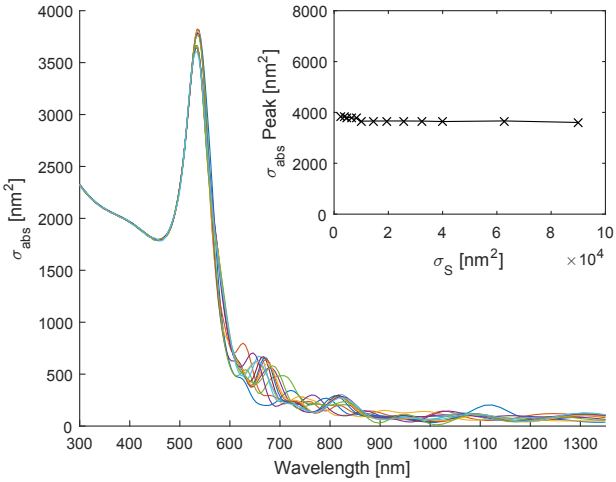

Figure 1.6: The absorption cross section σ_{abs} as a function of wavelength simulated by Lumerical for various source light injection cross sections σ_S ranging from 50^2 to 300^2 nm^2. The ripples on the red side of the absorption peak is a result of insufficiently small mesh size, and is non-physical. The absorption peak value as a function of light injection cross section is inserted in the top right corner.

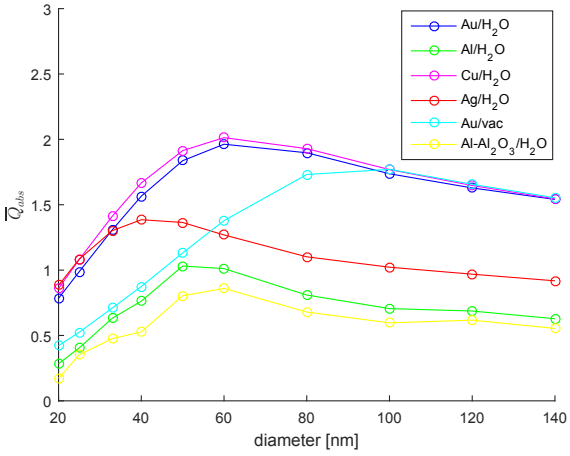

Figure 1.7: Average absorption efficiency $\overline{Q}_{abs}$ for wavelengths 300 - 1250 nm, calculated as $\overline{Q}_{abs} = \frac{1}{\Delta\lambda}\int_{300}^{1250} Q_{abs} d\lambda$. The best absorbers are 60 nm gold and copper. 40 nm is the most efficient size for silver both at peak wavelength and averaged.

1.5.2 Temperature induced color change in gold nanoparticle arrays: Investigating the annealing effect on the localized surface plasmon resonance

The environment in which the nanoparticles will be placed must be considered, since it may affect the absorption performance. Nanoparticles in a solar cell will be placed in the sunlight where they will be heated, which may change their optical behavior. In this article we observe quite a dramatic change in color, when annealing gold nanoparticles. The LSPR frequency and amplitude is determined by particle size, shape, and material, and the surrounding medium [59]. The surprising part of the results in this experiment is how little these parameters need to change to cause such a large change in color. SEM and AFM images merely show a smoothening of the particle surface and a slight decrease in height, no dramatic change in size or shape. All the experimental work was done by the thesis defender. The thesis defender was also the main writer of the manuscript with contributions to the scientific discussion and experimental design from the co-authors.

These results may be used to tune the LSPR of a nanoparticle based solar cell, but beyond that, the effect of annealing may be exploited in other sensor technologies. The color change is clearly visible to the naked eye and is not reversible, which can be advantageous for non electronic sensors. The nanoparticles can work as a temperature sensor in remote locations which have no power supply or no continuous monitoring. For example can a nanoparticle array be used as a product temperature history, revealing if the product has been exposed to temperatures over a certain limit.

One of the technical challenges in this experiment was how to image the same nanoparticle repeatedly with an AFM instrument with no stage positioning mechanism. The University of Bergen NanoStructures laboratory has an Anfatec "Eddy" AFM instrument, which is quite simple as far as AFMs go, and is intended for student education purposes [60]. As a solution, the thesis defender made a design where the cluster of nanoparticles were surrounded with arrows pointing toward them, large ones if they were far away, and smaller ones if they were close. The distance between the arrows were made short enough to make sure there would always be an arrow in the AFM image, no matter where the image was taken on the sample. The nanoparticle cluster was found by pushing the sample in the direction of the arrows.

Once the cluster was located, every single nanoparticle must be identifiable in the sea of other nanoparticles. This was achieved by arranging the particles in a very specific pattern, like a bar code. The cluster consist of 15×15 arrays, each array has 10×10 particles. In every array, one specific particle is removed. The

position of the absent particle signifies the position of that specific array. Thus, every particle is identified by its array's identifying feature. This is described in more detail in section 3.2.

Another technical consideration that had to be made relates to the SEM imaging. If the electron beam is focused on a small area for several seconds, the gold nanoparticles start to melt/sputter, changing the appearance of the particle, see Fig. 1.8. This was avoided by focusing the image at a spot adjacent to the desired image, thus minimizing the exposure time of the particles of interest.

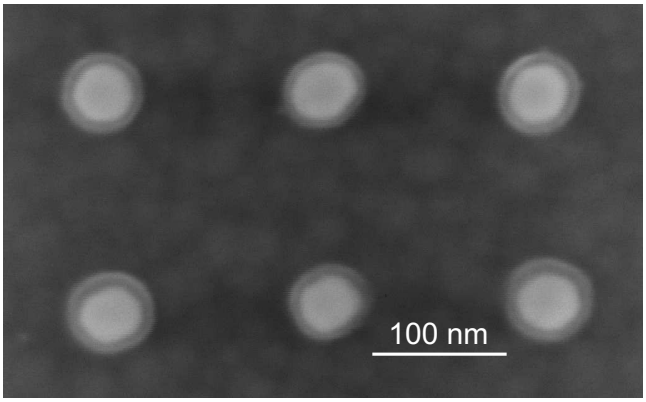

Figure 1.8: SEM image of degraded gold nanoparticles after being imaged for several seconds.

1.5.3 Light absorption and scattering of 40 - 170 nm gold nanoparticles on glass substrates

All the spectral analysis performed in this thesis is done using a TFA or DF spectroscopy, except the results presented in this article, where integrating spheres (and an extinction measurement setup) were used. Two spheres allow us to measure both reflected and transmitted light. The thesis defender assisted in writing the manuscript, and assisted in data collection from the integrating spheres and data analysis/calculations. Figure 2 and 3 in the article and all numerical simulations are done by the thesis defender. A detailed description of the calculations of the raw data spectra are included in section 3.3.

In this article we are only interested in the absorption and scattering of the MNP, not including the glass slide they sit on. By measuring and subtracting the reflected, transmitted and extinct light of the glass from the glass with MNPs, the influence of the glass slide on the spectra can be removed. Dark spectra are also obtained and subtracted.

The normalized MNP reflection contains the back scattered light, and the transmitted light contains the forward scattered light and the directly transmitted. Figure 1.9 shows the raw data from the integrating spheres of the 78 nm particle sized array. We compare our results to a similar structure produced with a different manufacturing procedure, hole-mask colloidal lithography, and find that their optical properties are comparable.

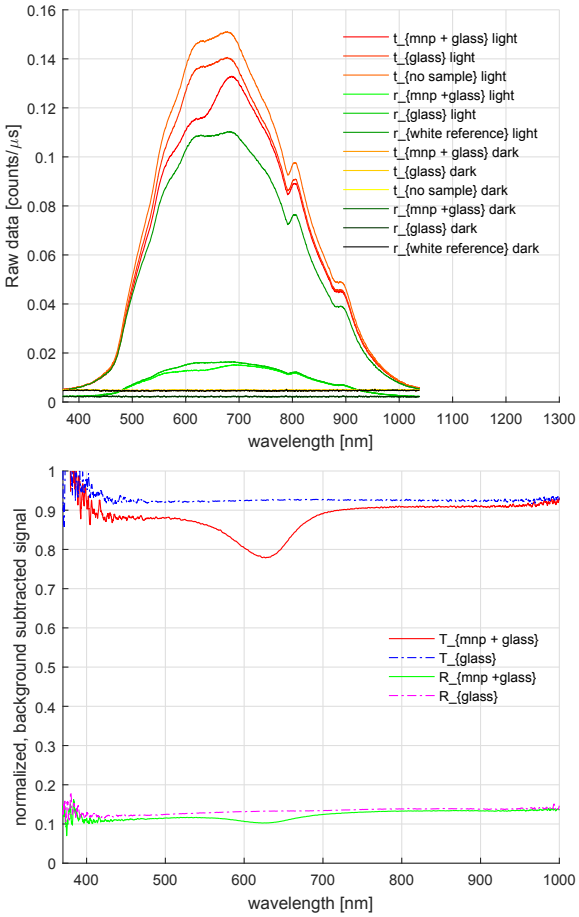

Figure 1.9: Top: Un-normalized, raw transmittance t and reflectance r data from integrating spheres for the 78 nm particle sized array (sample C). Bottom: Normalized and background subtracted transmittance T and reflectance R for the 78 nm particle sized array (sample C). For more information on how the raw data is treated to calculate the normalized transmittance and reflectance, see section 3.3.

1.5.4 Work function-driven hot electron extraction in a bimetallic plasmonic MIM device.

In this article, the optical and electrical properties of a bimetallic plasmonic MIM device is investigated. All the experimental work done for this article was done by the thesis defender, with initial assistance from Bob Zheng on the photocurrent measurements, and Martin M. Greve on the current voltage measurements. The thesis defender was the main writer of the manuscript with contributions to the scientific discussion and experimental design from the co-authors. All the experiments in this article were performed at Rice University, apart from the FDTD simulations and current-voltage (I-V) curve, which were done at the University of Bergen.

The devices produced for these experiments are a simplified version of the EnSol solar cell. By using rods instead of particles, and connecting the rods directly to the top electrode, the rods are electrically in contact, making replenishing easier. In addition, the distance between the plasmonic element and the top electrode is removed, thus removing one variable.

In the article, only the peak position of the FDTD simulations are presented. Here, the Poynting lines of the light wave at LSPR traveling through the thinnest device with 3 nm Al_2O_3 is presented in Fig. 1.10. The Poynting line/vector is the cross product of the electric and magnetic field, and describes the direction of the energy flux. If the Poynting line ends up circling inside the particle, the light has been absorbed.

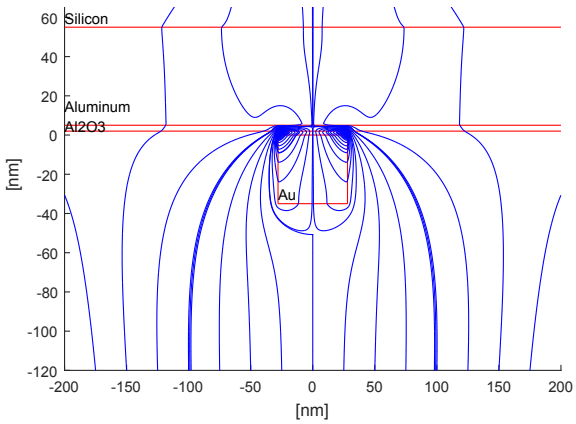

Figure 1.10: 2D FDTD simulation of the thinnest device with 3 nm Al_2O_3 from article D, showing the Poynting lines of the light wave at LSPR.

The devices from this article were used at the University of Bergen to investigate the performance of the new PCI built by the thesis defender, which is described in detail in section 3.4. It is designed to measure the current response of a device when exposed at the nanostructured/active region with light of a given wavelength. It was tested using a source meter for I-V measurements, where the I-V curve is measured for the thinnest device with a 3 nm Al_2O_3 layer from article D under illumination (with dark current subtracted). This measurement is done with both the Rice University and the University of Bergen PCI, and are shown together in Fig. 1.11, revealing a very similar result. Since the results were comparable, the University of Bergen PCI was used to produce the dark I-V characteristics presented in Fig. 2b in the article.

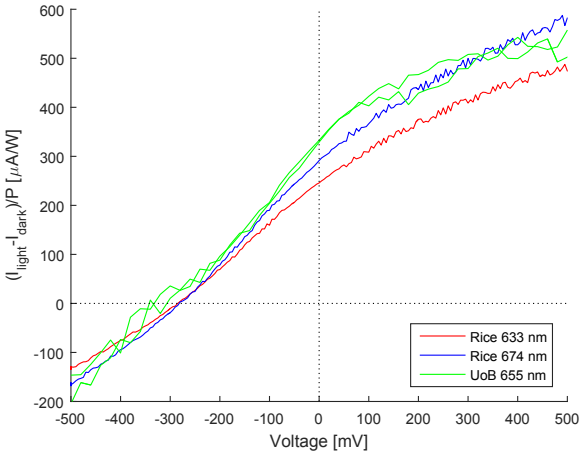

Figure 1.11: I-V curve for the thinnest device with a 3 nm Al_2O_3 layer from article D, measured using both the setup at Rice University, and the PCI built at the University of Bergen (UoB), demonstrating the reproducibility of the I-V characteristics. The current is measured under illumination, the dark current is subtracted, and is normalized by the illumination power. The numbers in the legend refer to the illumination wavelength. The laser used at the University of Bergen is not tunable, and is fixed at 655 nm.

1.5.5 Under-Water Superoleophobic Sapphire (0001) Surfaces

The motivation for this work, was to prevent the contamination of optical sensor windows used in harsh environments (i.e. oil contaminated waters). The thesis defender performed contact angle measurements for this article. An example of the under-water application of optical sensors is the monitoring of hydrocarbon levels in topside produced water discharge which is released to the environment by the oil industry. Such monitoring must be done to satisfy regulations for oil

pollution. Optical sensors can also be used for surveillance of subsea equipment, cameras, and flow rate and turbidity measurements [62].

In the oil industry, optical equipment have to survive being exposed to hydrocarbons, salt and biological material, and potentially high pressure and temperature variations. Precipitated salt fouling is formed by the crystallization of solid salts onto a surface from saturated solutions. Hydrocarbon fouling is most often related to the deposition of heavy hydrocarbon fractions, such as asphaltene and parafin waxes. Both salt and hydrocarbon fouling is strongly dependent on pressure and temperature conditions, and other chemical species in the fouling fluid [63]. Biofouling of substrates is formed by the deposition of biological films, which are often later covered with increasingly larger organisms.

Maintenance interventions at subsea is costly, and could involve risks related both to safety and environment, and in some cases requires shutdown of production processes, which could have large economic consequences. Therefore it is desirable to find an optical element that does not foul or break. Optical windows for harsh environment sensors are typically made of sapphire, since it is transparent and is the second hardest material after diamond [61]. The preparation of sapphire windows affects the resulting surface structure, which in turn affects the wetting properties of the window. In this article we investigate the relationship between the surface preparation, the wetting properties and how this relates to the long term hydrocarbon (oil) fouling.

This is a three way problem, and is addressed in three ways. Firstly, the question of surface structure is investigated by taking AFM images of three differently prepared sapphire windows. Secondly, the long term fouling is investigated by imaging these same windows and recording the oil coverage, after being installed in a water tank filled with 200 ppm oil in water for 12 hours. Thirdly, the wetting angle of these windows are recorded using a contact angle measurement system. Both water in air and oil in water wetting angles were measured.

Figure 1.12 shows the time evolution of the wetting angle for a hexadecane droplet on the epi-polished sapphire window not included in the article, illustrating that the timing of the wetting angle measurement is not arbitrary. Viscosity will affect how the angle decreases and settles over time. Wetting angle measurement techniques are discussed in more detail in section 3.5.

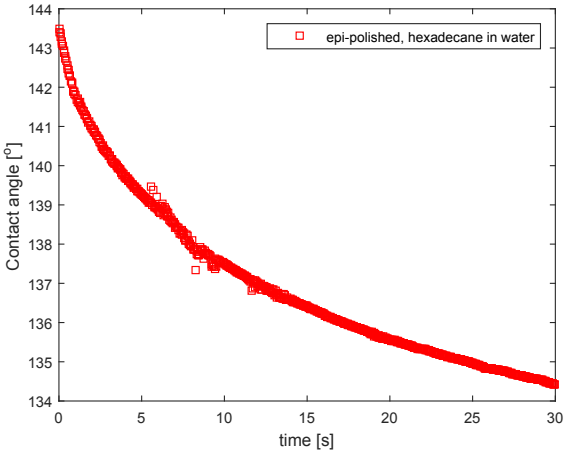

Figure 1.12: The time evolution of the wetting angle of a 3 μL droplet of hexadecane in water on an epi-polished sapphire surface.

1.5.6 How to design a simple, small scale, nano lithography research laboratory.

This article is somewhat untraditional, in that it concerns the establishment and running of a low cost clean-room lab. The thesis defender did the contamination experiment presented in table 1, took SEM images for Fig. 2 and 3, and assisted in writing the manuscript.

In our group, we are very lucky to have excellent nanostructuring equipment, to be used by a small number of people, giving each person plenty of lab time. By carefully choosing the right equipment and lab design, a clean-room lab could be built despite a limited budget. Students can be trained on several instruments, and are involved in the running and maintenance, which is a great learning experience. What makes the lab low cost, is the limited clean-room area, and the placing of non-critical manufacturing steps outside the clean-room. Procedures such as lab wear, sticky mats and routine cleaning helps limit the contamination, resulting in successfully manufactured devices despite the increased contamination risk. Our hope is that this article may be of assistance to other institutions or small businesses who wish to invest in affordable clean-room labs.

Chapter 2

Theory

2.1 Optical behavior at the nano-scale

Plasmonics, which is a major theme in this thesis, falls under the category nanophotonics. As the name suggest, nanophotonics is the combination of nano-scale structures and the field of photonics. Photonics describes the physics of light, specifically the particle properties of light; photons. We all encounter phenomenons like reflection and transmission, colors and brightness, on a daily basis, usually in the context of bulk materials on a macro level. But on the nano-scale, when the material structure is in the same order of magnitude (or smaller) as the wavelength of light, the interaction of light and matter will vary from that of bulk matter [64, 65]. This is explored through plasmonics, which describes how electromagnetic radiation (light) interacts with conduction electrons in metallic nanostructures.

In this thesis, MNPs and metal nanorods were illuminated. As the wavelength of the incident light is larger than the structures itself, the electric field is relatively constant over the whole particle at any given time, displacing the conduction electron with respect to the ion cores. Consequently, a restoring electric field occurs between the cores and conduction electrons, resulting in a collective oscillation. When the frequency of the incident light wave matches the frequency of the oscillating electrons, a resonance condition is achieved. This is known as localized surface plasmon resonance, and is the main mechanism for the absorption and scattering properties found for MNPs. The same is true for nanorods being illuminated by TE polarized light, since the electric field then oscillates across the narrow width of the rod. For TM polarized light, with the electric field along the length of the rod, the oscillation of electrons happens over a wide range of frequencies. This also occurs for bulk material or for propagating surface plasmons,

and results in dispersion.

One of the earliest examples of MNPs being used is for coloring the Lycurgus cup, which is dated to approximately 300 B.C. and is made of silver nanoparticles embedded in glass [66]. As early as 1871, Lord Raleigh explained that the sky is blue due to the scattering of light by particles much smaller than the wavelength of radiation [67]. In 1908, Mie presented a solution to Maxwell's equation describing the scattering of electromagnetic radiation by a sphere of arbitrary size [68]. In 1956, Pines described the collective oscillations of conduction electrons in metals as plasmons [69], and in 1970, Kreibig and Zacharias used surface plasmons to describe the optical properties of metal nanostructures for the first time [70]. The field of plasmonics is now rapidly growing, due to it's potential applications to light detection and harvesting, and the advancement of nanostructuring instrumentation and techniques [71].

There are several approaches to investigating the interaction between electromagnetic waves and small particles. Possibly the simplest approach is called Raleigh scattering, named after Lord Raleigh. One starts out with a spherical particle in a medium, with an incident plane wave, and applying the quasi-static approximation. In the quasi-static approximation the particle is much smaller than the wavelength, so we can assume that the electric field is constant over the whole particle at a given time. This is described by $x << 1$ and $|m|x << 1$, where the size parameter x and the relative refractive index m is:

$$x = kr = \frac{2\pi nr}{\lambda}$$

$$m = \frac{k_m}{k} = \frac{n_m}{n}$$

given the refractive index of particle n and medium n_m, the sphere radius r, the wavelength λ, and wavenumber of particle k and medium k_m. With this criteria met, the particle can be thought of as a dipole, and the absorption and scattering cross sections, σ_{abs} and σ_{sca} respectively, are given as [59, 72]

$$\begin{aligned} \sigma_{abs} &= k\mathrm{Im}\left[\alpha\right] = 4\pi kr^3 \mathrm{Im}\left[\frac{\varepsilon - \varepsilon_m}{\varepsilon + 2\varepsilon_m}\right] \\ \sigma_{sca} &= \frac{k^4}{6\pi}|\alpha|^2 = \frac{8\pi}{3}k^4 r^6 \left|\frac{\varepsilon - \varepsilon_m}{\varepsilon + 2\varepsilon_m}\right|^2 \end{aligned} \tag{2.1}$$

where α is the polarizability, ε and ε_m is the permittivity of the sphere and surrounding medium respectively, also known as the dielectric function. The refractive index n and dielectric function ε of a material is related by: $n(\omega) = \sqrt{\varepsilon(\omega)}$.

From Eq. 2.1 it is easy to see why the refractive index of the surrounding medium has such a significant impact on the absorption and scattering of MNPs, as a resonance condition occurs when $|\varepsilon + 2\varepsilon_m|$ is at a minimum.

Mie theory is conceptually very similar, however, it deals with what happens when the particle is no longer small enough to be though of as a dipole. The quasi-static approximation is in that case not valid, since the electric field is no longer constant across the particle. As a result, the oscillation of the conduction electrons does not move in one collective motion, and as such can not be described by Raleigh scattering alone. In Mie theory, the electromagnetic fields are calculated by expanding the internal and external fields into a set of normal modes described by vector harmonics [59]. The absorption and scattering can then be expressed as a superposition of these normal modes. For these larger particles, higher-order resonances may exist. Mie theory also explains the redshift of the resonance wavelength for larger particles, due to the increase in distance between the conduction electrons and ion cores [59, 72], this can be seen nicely in Fig. 3.2.

The smaller nanoparticles investigated in this thesis can be described by Raleigh scattering, and the larger nanoparticles have properties which can only be described by Mie theory. However, both approaches address nanospheres, not nanostructures of arbitrary shape. In the following, we will look into the advantages of numerical methods.

2.2 Numerical methods

The size, shape, and permittivity of the surrounding medium of the particles are what determine which frequency the resonance occurs at [59]. When dealing with varying boundary conditions, materials, and (sometimes non symmetric) geometries, electromagnetic problems are not always analytically calculable, with closed form equations. A computational simulation is in order. Some of the objectives of computational electromagnetics are to provide efficient approximations to Maxwell's equations, to describe electromagnetic propagation when not in free space, and specifically relevant to this thesis, describe the electromagnetic radiation scattered and absorbed by small particles.

Depending on the specific problem at hand, there are many approaches and tools for modeling electromagnetic propagation. A method may solve the electric and magnetic fields, the power flow direction (Poynting), waveguide normal modes, dispersion or scattering. Which one to choose is application specific. Picking the right one is crucial, as choosing the wrong one may result in the wrong answer (if the application does not meet the constraints of the method) or excessively long computation time. Most of the methods (though not all) can be sorted into two

categories; integral equation solvers and differential equation solvers.

One approach in the integral equation solver category is the discrete dipole approximation (DDA). In DDA, an arbitrarily shaped nanostructure can be built using many dipoles with a given dipole moment. The dipoles interact with each other via their electric fields, resulting in in a linear system of equations based on the integral form of Maxwell's equations. This way, the scattering and absorption can be found for an arbitrary geometry. A disadvantage of this technique is that the electromagnetic field diverge at the grid point, where the dipole is located [73]. Also, the computational power required is quite high.

Another integral equation solver is the method of moments (MoM) [74]. In MoM, linear partial differential equations which have been formulated as integral equations are solved. It is significantly more efficient than DDA for problems with a small surface to volume ratio, because it requires only calculations of the boundary conditions rather than all points through space. Compression techniques such as multipole expansions may be used to decrease storage requirements and computation times, but increases complexity, and is not suited for all applications. For many problems these methods are less efficient than finite-element or finite-difference methods which we will look at later.

The last integral equation solver we will look at is the partial element equivalent circuit method (PEEC), which combines electrodynamics and circuit analysis. The integral equation is interpreted as Kirchoff's voltage law (the conservation of energy around a closed circuit path) and is applied to a basic PEEC cell. The method is widely used for combined electromagnetic and circuit problems, and applies to both time and frequency domains [75].

Moving on to differential equation solvers, where the most common ones are the finite-difference method and finite element method (FEM) [76]. Finite-difference methods are intuitive and effective approaches, where the space in question is discretized by a rectangular mesh, and the electromagnetic fields, and other relevant parameters are calculated for each element in the mesh. Calculations can be done for increasing time steps, called finite-difference time-domain (FDTD) [77], or for increasing frequency steps, called finite-difference frequency-domain (FDFD). Each of these approaches have their advantages, FDTD is useful when investigating the time evolution of an electromagnetic field, FDFD is better at incorporating material dispersion and is useful when studying periodic structures. Similarly, FEM also divides up the simulation space into a mesh, but in this method, the elements are not rectangular. For 3D simulations, the mesh shapes can be tetrahedron, quadrilateral pyramid, triangular prism, and/or hexahedron. This gives a much better representation of structures with curved surfaces, and thus very accurate results,

but is more complex than the finite-difference method. After dividing ut the space, the method then find approximate solutions of partial differential equations, and then combines them to a global solution.

Two of the most prominent commercial software packages available for solving nano-optics problems are Lumerical Solutions (Vancouver, BC, Canada) [78], which use finite-difference method, and COMSOL Multiphysics® Modeling Software (Burlington, MA) [79], which use FEM. Lumerical has been used in several of the articles presented in this thesis because the FDTD method is well suited for calculating the absorption and scattering of metallic and dielectric composites, and it has an user-friendly interface. It will be presented in more detail in the following section.

2.2.1 Lumerical

Lumerical software includes finite-difference time-domain (FDTD) solutions for nanophotonic design, and MODE solutions for waveguide design. It can solve optical scenarios, as well as charge and heat transport, and model circuit design. Lumerical's FDTD method is a fully vectorial Maxwell solver, and can be used for design analysis and optimization of nanophotonic devices, processes and materials [78].

All the Lumerical simulations done for this thesis are done using the FDTD solver package. Some of the benefits of this method are that the solution is easily Fourier transformed for frequency solutions, it handles non linear behavior, and it is a robust and mature method. The drawbacks include that it is inefficient for highly resonant devices, and square grid/mesh doesn't match curved elements.

In Lumerical FDTD solver, Maxwell's curl equations in non-magnetic materials are solved

$$\begin{aligned} \frac{\partial \vec{D}}{\partial t} &= \nabla \times \vec{H} \\ \vec{D}(\omega) &= \varepsilon_0 \varepsilon_r(\omega) \vec{E}(\omega) \\ \frac{\partial \vec{H}}{\partial t} &= -\frac{1}{\mu_0} \nabla \times \vec{E} \end{aligned} \tag{2.2}$$

where $\vec{H}$, $\vec{E}$ and $\vec{D}$ are the magnetic, electric and displacement fields respectively, and $\varepsilon_r(\omega)$ is the complex relative dielectric constant, and μ_0 is the vacuum permeability. The magnetic and electric fields can be can be split into six components H_x, H_y, H_z, E_x, E_y and E_z. Equation 2.2 are solved for each grid cell in a discretized space and time interval, though at slightly different locations within the grid cell due to the nature of Maxwell's equations, which describes how an elec-

tric field induces a magnetic field and vice versa. This is illustrated in Fig. 2.1, showing what is called the Yee cell. By calculating the magnetic field half a cell step and half a time step away from the electric field, the calculations for both the electric and magnetic fields can be made within the same loop iteration, decreasing the total amount of loops necessary by half. The results are interpolated to the origin of each grid point. This solver use a rectangular Cartesian mesh, with a smaller mesh for a higher dielectric constant/refractive index in order to maintain a constant number of mesh points per wavelength. It can be set manually in regions where we need the mesh extra fine, such as for complex structures or in areas where the fields change rapidly.

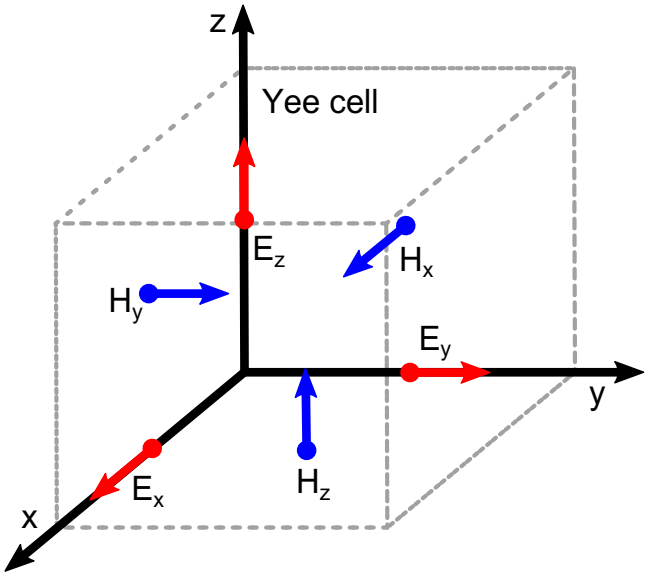

Figure 2.1: The Yee cell, showing where in a grid cell the magnetic and electric field components are solved in Lumerical FDTD method.

The solver offers a range of boundary conditions, such as perfectly matched layer (PML), periodic and Bloch, and a range of light sources, such as point dipoles, beams, plane waves and total-field scattered-field (TFSF). For the simulations presented in this thesis, the TFSF was used. This source type contains a plane wave, but the computation region is separated into two by a rectangular box. Inside the box, the total field exist, i.e. both the incident and scattered fields, and outside only the scattered field exist. This is achieved by injecting a plane wave from one surface of the source box, and subtracting it at the opposite side. This type of source is useful when studying the scattering behavior of objects, as the scattered field can be isolated.

The electric and magnetic fields can be recorded through the use of monitors, which integrate the total power flow across the surface of the monitor using the following equation:

$$\text{Power}(\omega) = \frac{1}{2} \int \text{Re}\left(\vec{P}(\omega)\right) d\vec{S} \tag{2.3}$$

where $\vec{P}$ is the power at each point of the monitor surface $\vec{dS}$. The monitor box detect light coming from both inside and outside the box and subtracts the latter from the former. In the case of a TFSF source, only scattered light will reach the monitor if it is placed outside the light source. By placing a monitor inside the light source box, it will receive incident light on the outside surface, and transmitted and scattered light on the inside surface, leaving the net difference, i.e. the absorption.

In order to simulate the LSPR effect in Lumerical, we start out by defining a FDTD simulation space. Within this space we place a light source, two monitors, one to detect absorption, and one for scattering, and the nanostructure we wish to investigate. The library provides a variety of shapes and materials, which can be combined to make the desired geometry. Power monitors can be added for displaying the electric and magnetic hot spots, or Poynting vectors. A version of the Lumerical simulation layout from article D is shown in Fig. 2.2.

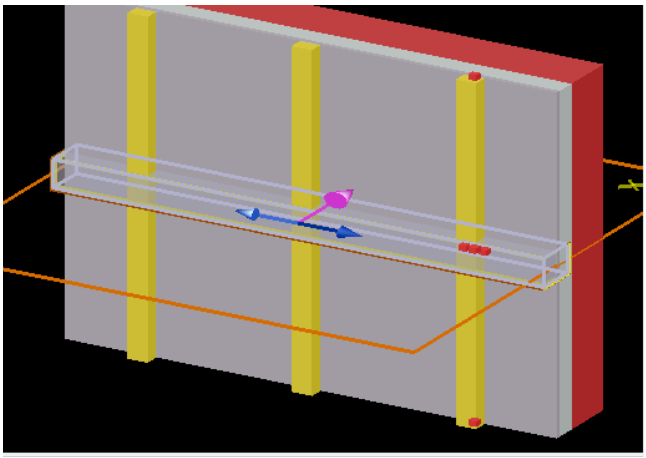

Figure 2.2: Lumerical simulation layout of a device used in article D. The orange square is the simulation boundary with PML, indicating a 2D simulation. The blue and magenta arrows shows the electric field and injection direction respectively of the plane wave source (yellow box). The gray box is a monitor. Gold rods are shown in yellow, the Al_2O_3 is dark gray and aluminum is light gray. The silicon substrate is red.

Chapter 3

Methods

In this chapter some of the experimental methods used in this thesis are presented in more detail. Particular emphasis is on experimental procedures that have been developed/used for the first time by the thesis defender during this Phd. Development of manufacturing procedures and navigation of our simple AFM instrument is described, the calculations used in the integrating spheres are given, and the PCI at Rice University and a PCI made by the thesis defender is presented.

3.1 EBL procedures

Electron Beam Lithography (EBL) has been used extensively in this thesis to fabricate samples used in the experiments. In EBL, an electron beam is extracted from a filament by applying an acceleration voltage. The beam travels through an aperture and is focused on the sample surface by electromagnetic lenses. The surface is covered by either a positive or negative photo resist, which is sensitive to the exposure of the electron beam, causing either clipping or cross-linking of the polymer chains in the photo resist respectively. Depending on the type of photo resists, different doses are required. The exposure time t in seconds is given as:

$$t = \frac{D}{I} \tag{3.1}$$

where D is the dose in C, and can be given per area, line or point. The beam current I is given in A [80]. At the University of Bergen NanoStructures Laboratory we have a Raith E-Line EBL instrument, which we also use for all our SEM needs. It can distinguish structures down to approximately 5 nm, and working distance, stigmation, brightness, contrast and sample position is easily controlled with the instrument software. It provides 2D images of any (conducting) sample surface.

A recipe had to be developed in order to produce structures with the desired size and robustness. In literature, it is common to deposit a small layer of for example titanium in order to make gold adhere better to glass substrates. Due to this rigorous investigation of patterning parameters, such an adhesion layer was not necessary in our case. First, the photo resist is distributed on the sample surface by spin coating. The spin speed determines the PMMA thickness, and must be tested regularly, as PMMA becomes more viscous over time due to evaporation of the diluting solvent. A number of dose matrices of MNPs on ITO substrates were produced by EBL, while varying source acceleration voltage (eht) and aperture (a), thus mapping out the resulting particle size, and is shown in Fig. 3.1. Figure 3.2 show some of these arrays taken with optical (stereo) microscope. Proximity effects during EBL fabrication causes larger particles which redshifts the macroscopic color.

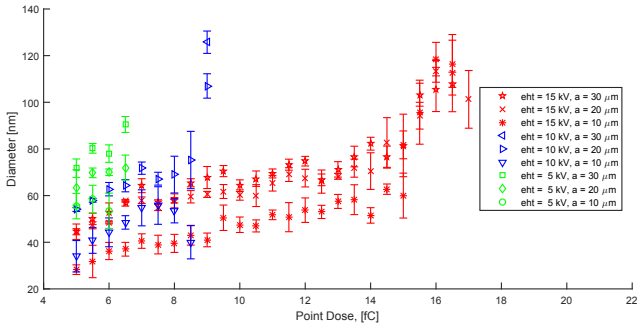

Figure 3.1: Size of hole in PMMA for various acceleration voltages (eht), apertures (a), and point doses.

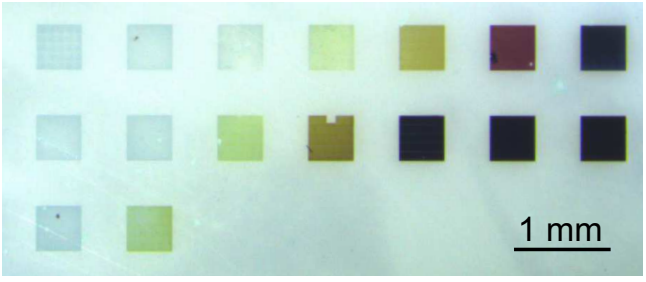

Figure 3.2: Stereo microscope image of gold nanoparticles with increasing point dose from left to right (9-61 fC) resulting in increasingly larger particles of approximately 50-170 nm (top line). The interparticle distance is increased from 160 to 265 nm from bottom to top. Macroscopically, the arrays have different colors and light intensity, due to their difference in particle size and spacing (lower spacing leads to an increase in proximity effects during EBL exposure).

3.2 AFM navigation

Our lab has an Anfatec "Eddy" atomic force microscope (AFM), see Fig. 3.3. It is a fairly simple instrument intended for educational purposes. In theory it has an xy resolution of 5 nm, though in reality this is very dependent on the quality of the tip, among other factors. SEM images of three different tips are shown in Fig. 3.4. The one advantage it holds over SEM is that it produces 3D images, and the z resolution is in the range of 0.5 nm. Unfortunately, it can only scan over an area of 30x30 μm^2, and the only sample positioning mechanism is pushing it by hand.

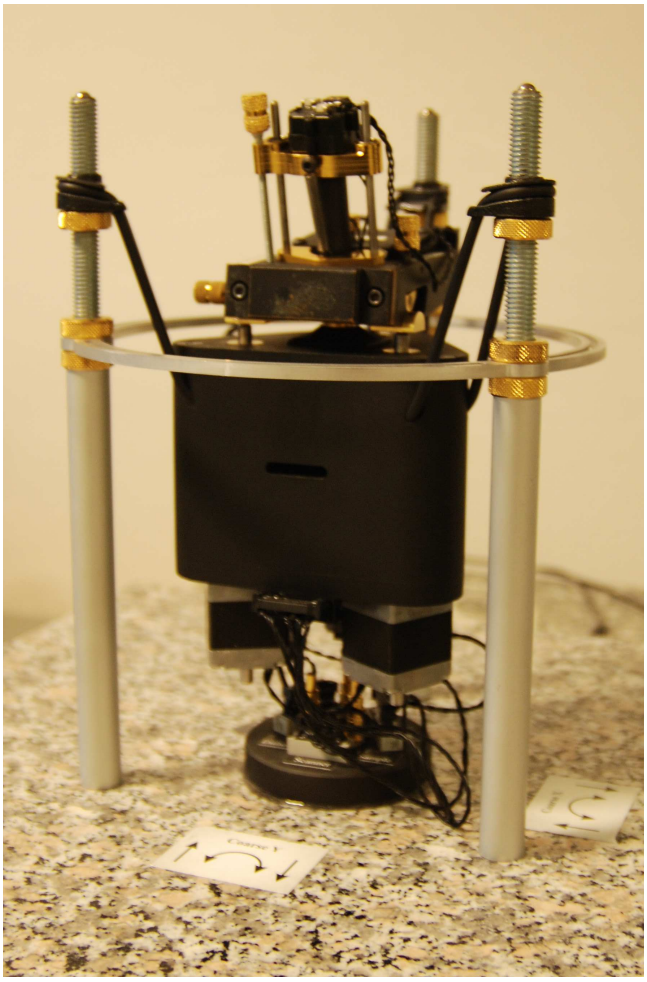

Figure 3.3: Anfatec "Eddy" atomic force microscope intended for educational purposes, and used for simple height measurements.

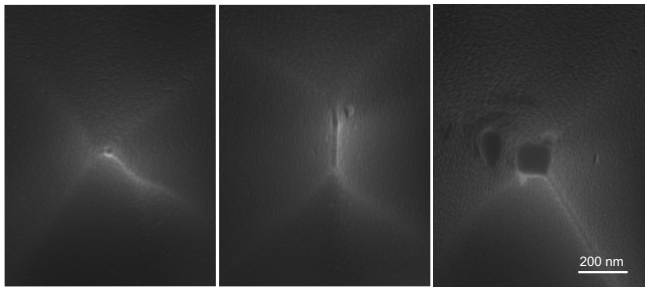

Figure 3.4: SEM images of three AFM tips. The left one is as specified with a tip smaller than 35 nm, however a large portion of the tips from the same shipment are like the other two, or worse.

For article B, it would be interesting to know the volume of specific MNPs. Because of the unreliable xy dimensions in AFM, the area data was collected from SEM images and z data from AFM, combining the information to calculate the volume. Previously, large arrays of MNP had been manufactured so MNPs could be easily found when doing AFM measurements. Since the AFM instrument have no specific position control, this would provide z data of some random MNPs, and combined with some random SEM images, would give a statistical averaged volume value. To get the volume of a specific particle, a sample where each particle was identifiable had to be made, as well as a way to navigate to it by hand.

The solution was to make an array of 15x15 clusters of particles which could fit within the AFM range of 30x30 μm^2. The array can be seen in Fig. 3.5 and 3.7. Each cluster consist of 10x10 particles in a square array pattern, and for each array one or two specific particles was removed, giving that array it's identifying mark. For example, the cluster in column 5, row 1, would have the particle in array position 5,1 removed, as shown in Fig. 3.6. This way, there would be no confusion about which particles was being shown in any AFM or SEM image within the 30x30 μm^2.

In order to locate this array with AFM, a 3x3 mm^2 area surrounding the MNPs was patterned with arrows pointing towards the MNPs, see Fig. 3.7. More than 0.5 mm away from the MNPs the arrows were 10 µm, 20 µm apart. Closer than 0.5 mm, they were 5 µm, 10 µm apart. Within 50 µm of the MNPs, the arrows were 5 µm apart. In order to find the MNPs with the AFM, an image was taken, which is bound to contain at least one arrow, then the sample was moved gently using a tweezer in the direction the arrow was pointing. The smaller and closer the arrows were, the less the sample would be moved. Bear in mind, xy for the sample is not necessarily xy in the image software, so some mapping is required

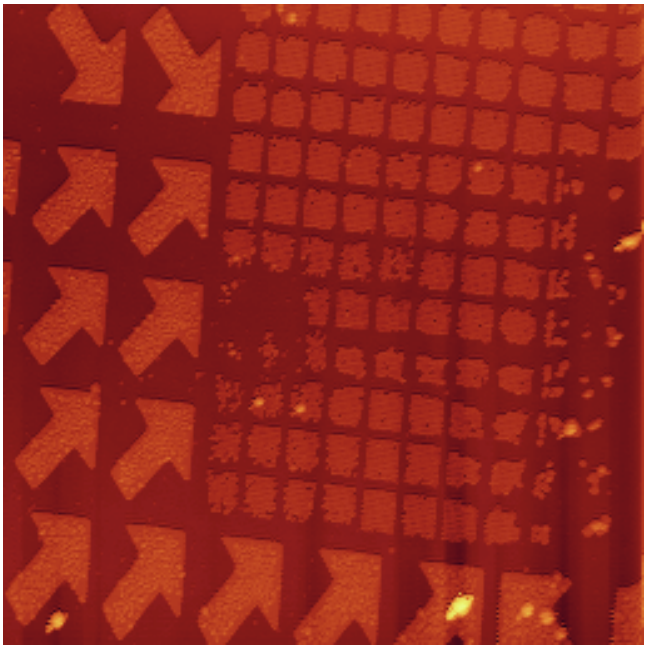

Figure 3.5: AFM image of the array clusters and some of the arrows. Because AFM is somewhat intrusive, and because gold does not adhere well to glass, it can potentially cause MNPs to be shaved off. That is why some of the clusters are missing. The image is 30x30 μm^2.

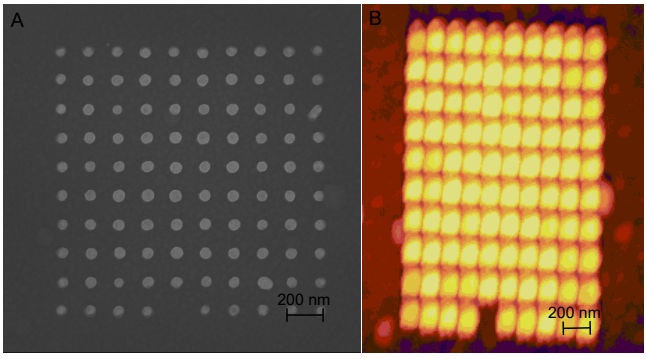

Figure 3.6: SEM (A) and AFM (B) image of cluster 5,1 with the particle in column 5 row 1 removed. Particles appear larger in xy direction in the AFM compared to the SEM, possibly due to a blunt AFM tip or static charging (particles and tip are of metal, but substrate is isolating), however z data is provided.

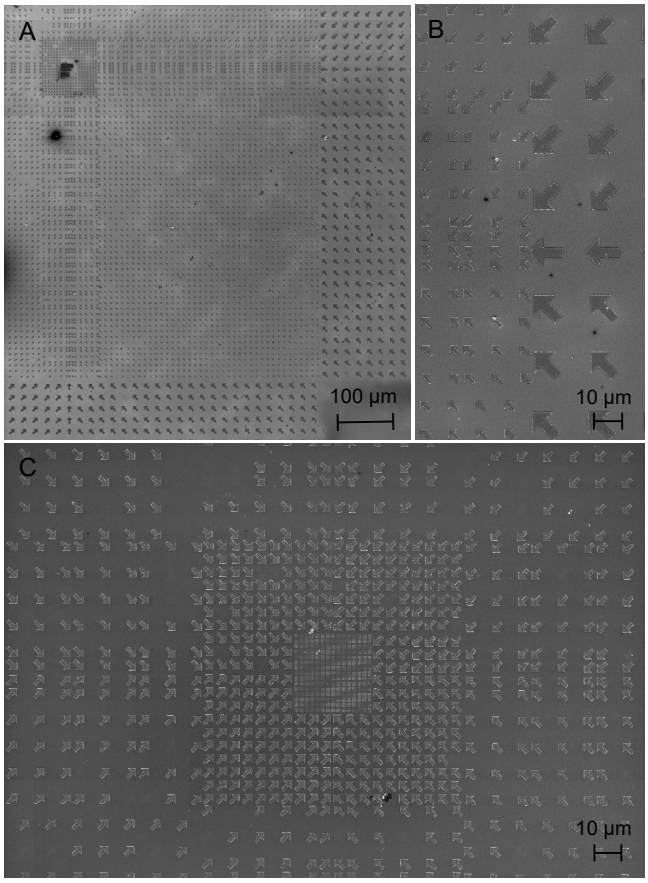

Figure 3.7: SEM images of (A) the lower right corner of the sample, (B) the transittion between large and small arrows, and (C) the center of the sample with the MNP array clusters in the middle. The MNP array is surrounded by small arrows close together, further out are small arrows further apart, and even further away are large arrows. The arrows point diagonally, except the ones on the axis lines, which point straight at the MNPs. The MNPs are on a glass substrate, which creates electron charging of the substrate when SEM images are taken, and is why some of the MNP arrays have a darker shade.

to determine which direction in the software correspond to which direction of the sample. Once the MNPs was located and imaged, they would be easy to find in the SEM due to their identifying features.

AFM is a somewhat intrusive imaging technique, and gold MNPs does not adhere well to the glass substrate it was built on. For contact mode AFM, this will always lead to the MNPs being shaved off the surface, leaving nothing to image. Dynamic mode AFM is better, because the tip is kept further away from the surface, but would still occasionally shave the MNPs off the substrate. For this project, it was found that the least damaging method was to use kelvin probe force microscopy (KPFM), which is essentially like dynamic mode AFM, with an additional bias applied to the tip. A more detailed description of contact mode, dynamic mode and KPFM is included in appendix II.

A debate which often occurs when dealing with AFM images is whether what is seen in the image is real or scanning artifacts. Combining AFM and SEM images of the same structures may aid in identifying features in both AFM and SEM images.

3.3 Integrating spheres

In integrating spheres the (diffuse) reflection R and transmission T through a sample can be measured. Figure 3.8 shows the integrating sphere setup. In article C we are interested in measuring R and T, as well as the directly transmitted, i.e. the extinct light E (which is measured using a different setup, see article C). R, T and E was then used to calculate the absorption and scattering of MNPs. Since the nanoparticles were resting on glass substrates, R, T and E was measured for samples with MNPs on glass, and for the glass only (in the proximity of the MNPs), so that R, T and E of the MNPs alone could be calculated.

$$\begin{aligned} R_{glass} &= \frac{\mathrm{I}-\mathrm{II}}{\mathrm{V}-\mathrm{VI}} & R_{mnp+glass} &= \frac{\mathrm{III}-\mathrm{IV}}{\mathrm{V}-\mathrm{VI}} \\ T_{glass} &= \frac{\mathrm{IX}-\mathrm{X}}{\mathrm{VII}-\mathrm{VIII}} & T_{mnp+glass} &= \frac{\mathrm{XI}-\mathrm{XII}}{\mathrm{VII}-\mathrm{VIII}} \\ E_{glass} &= \frac{\mathrm{XVII}-\mathrm{XVIII}}{\mathrm{XIII}-\mathrm{XV}} & E_{mnp+glass} &= \frac{\mathrm{XIX}-\mathrm{XX}}{\mathrm{XIV}-\mathrm{XVI}} \end{aligned} \tag{3.2}$$

$$\begin{aligned} R_{mnp} &= R_{mnp+glass} - R_{glass} &&= S_R \\ T_{mnp} &= T_{mnp+glass} - T_{glass} &&= T \\ E_{mnp} &= E_{mnp+glass} - E_{glass} &&= E \end{aligned} \tag{3.3}$$

Equation 3.2 shows the calculations for R, T and E using the twenty necessary

measurements given in table 3.1. The reflectance measurements are normalized by a white reference measurement, and the transmittance measurements are normalized by a measurement with no sample present. The extinction measurements for no sample, which is used for normalizing the extinction spectra, are taken twice corresponding to the setup geometry for measuring on the glass substrate and nanoparticles respectively. Dark spectra are subtracted from all corresponding light spectra. Eq. 3.3 relates the calculations from Eq. 3.2 to the notation given in article C. Expressions like absorption, absorbtance and absorbance are easily confused, and are therefore addressed in appendix III.

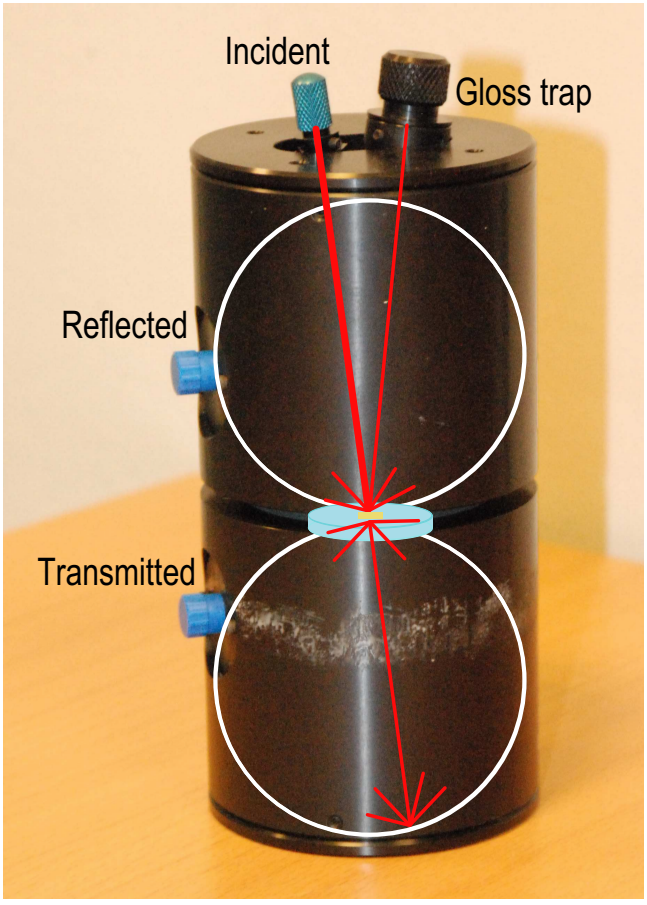

Figure 3.8: Integrating sphere setup photo with diagram. The spheres were used for measurements presented in article C.

Table 3.1: List of measurements done with integrating spheres and extinction measurement setup.

	Reflectance		Transmittance		Extinction	
	light	dark	light	dark	light	dark
No sample			VII	VIII	XIII, XIV	XV, XVI
glass	I	II	IX	X	XVII	XVIII
MNP + glass	III	IV	XI	XII	XIX	XX
White reference	V	VI				

3.4 Photocurrent Instrument

In order to realize the EnSol solar cell idea, it is crucial to investigate the relationship between incident light and resulting electrical response. In order to achieve this, we need an instrument which has a light source of known properties, a mechanism for focusing the light at the active region of a sample, electrical contact, and source meter for readout. At Rice University, the Halas Nanophotonics group has built such an instrument, which is described in section 3.4.1. The thesis defender built one at the University of Bergen NanoStructures Laboratory based on a similar principal, this is described in detail in section 3.4.2. This instrument will be vital in the future investigation of photo-electric devices developed by the University of Bergen Nanophysics group. When finished, the I-V characteristics and spectral response of targeted nanostructures can be obtained.

3.4.1 PCI at Rice University Halas Nanophotonics Laboratory

Figure 3.9 shows a schematic of the Rice University PCI setup. It consists of three separate functions. The first function is a white light lamp and camera, which enables us to see what we are doing. It assists in the focusing and aiming of the laser beam, and in the placement of the electrical contact probes. Beamsplitters are used to direct the white light onto the same path as the laser and the light reflected from the sample onto the camera. The second function is the laser with accompanying mirrors and lenses, used for positioning and focusing. The laser is tunable, allowing for photo excitation from 450 - 690 nm. The z-fold optics allows us to control both the xy position and the incoming angle of the laser beam on to the sample. Strategically placed parabolic mirrors decreases the laser spot size, and the microscope objective focuses the beam onto the surface of the sample, ensuring high laser light intensity at a small spot size. The third function is the electrical setup. Two probes are placed on individual xyz controllers, so the probe tip can be placed on the electrical connection pads of the sample. The probes can be connected to a source meter for I-V measurements, or to a LIA. A LIA needs

a pulsating signal, so the laser is chopped, and the chopper frequency information is fed to the LIA. A detailed description of LIAs is included in appendix IV. The Rice University PCI is shown in Fig. 3.10. For details on instrument names and models, see the article D.

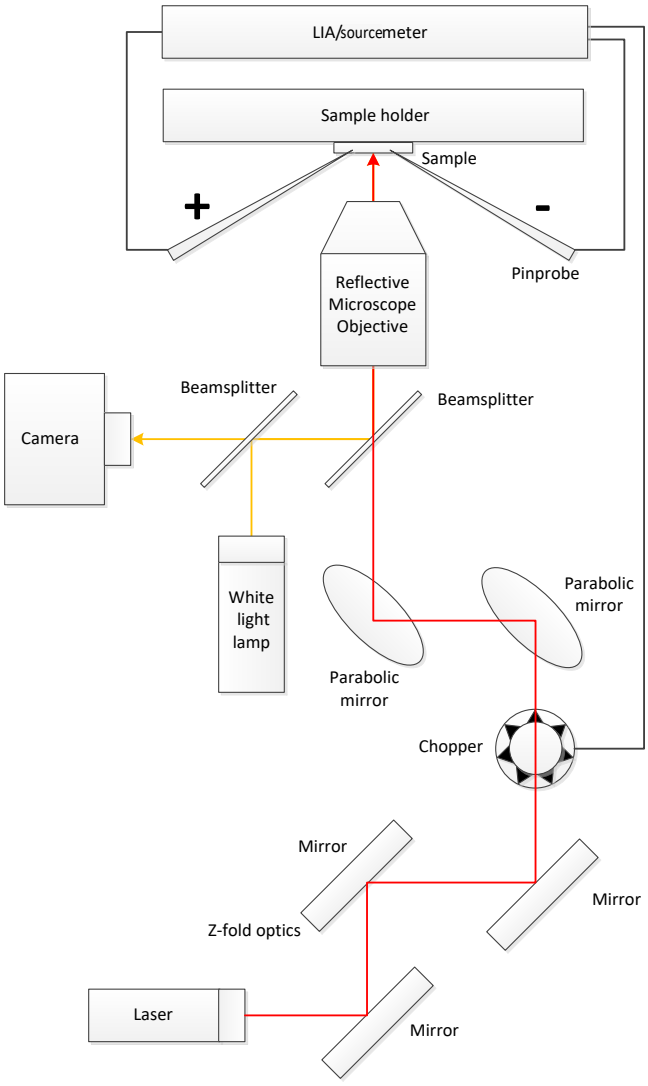

Figure 3.9: Schematic of the photocurrent instrument setup.

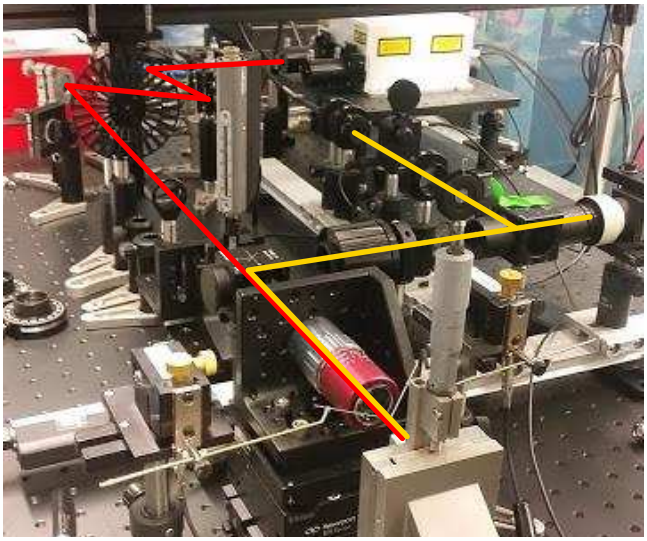

Figure 3.10: Photocurrent instrument at Rice University. White light path from source to camera is shown in yellow, while the laser path through the z-fold and microscope objective is shown in red. The parabolic mirrors are not installed at the time this picture was taken.

3.4.2 PCI at University of Bergen NanoStructures laboratory

To be able to do similar measurements locally in the future, a similar instrument was built at the University of Bergen NanoStructures laboratory by the thesis defender. All optics were chosen to handle wavelengths between 400-700 nm. The setup is essentially very similar to the Rice University PCI, except lenses are used instead of parabolic mirrors to decrease the laser spot size, and a chopper and LIA has not yet been implemented. The University of Bergen PCI is shown in Fig. 3.11. The camera is a Thorlabs CCD camera, and the microscope objective has ELWD (extremely long working distance) and is from Nikon. An MRL 655 nm (1W) laser is used temporarily. This laser is not tunable, so a signal can only be measured at 655 nm. To measure the laser power, a Thorlabs PM100D optical power and energy meter is used. From Quater Research and Development comes the electrical probes, which are tungsten needles held by a collet probe arm with coaxial cable. It is isolated near the needle/probe for less capacitance. All components are placed inside an optically shielding box to keep noise light out, and protect the user from strong laser light. A detailed list of the components used for the University of Bergen PCI is given in appendix V.

The I-V curve presented in article D Fig. 3 is produced by the University of Bergen

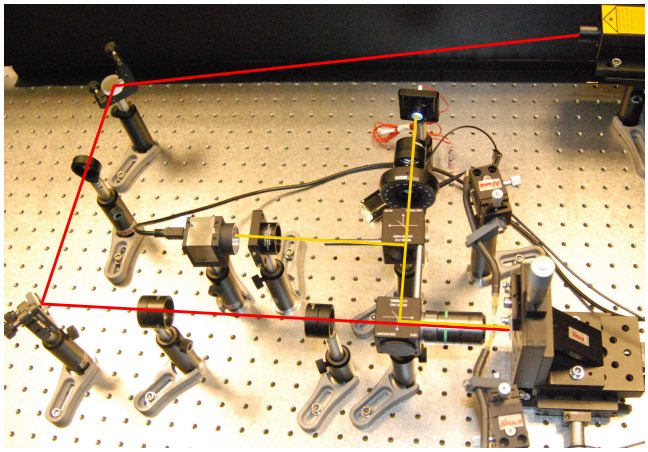

Figure 3.11: Photocurrent instrument at the University of Bergen. White light path from LED source to camera is shown in yellow, while the laser path through the z-fold (here shaped like a u) and microscope objective is shown in red.

PCI. Also, as mentioned in section 1.5.4 and shown in Fig. 1.11, the University of Bergen PCI was tested and compared to the Rice University PCI, giving very similar results.

3.5 Measuring the wetting angle

Now we will discuss the measuring of a non-optical effect of nanostructures; wetting. Wetting is a balance between adhesive and cohesive forces. It is a measure of how well a liquid can maintain contact with a solid when it is surrounded by a gas or another liquid, and is given by a contact angle. After taking a picture of a liquid drop placed on a solid surface, the contact angle can be measured at the interface where the liquid-vapor or liquid-liquid meets the solid. There are several measurement methods. In the static sessile drop method, the angle is measured after the drop has been placed on the surface by a syringe, as shown in Fig. 3.12. The dynamic sessile drop method is done by measuring the angle while increasing and decreasing the volume of the drop using the syringe. A hysteresis is obtained by increasing the volume until the one finds the largest possible angle without increasing the solid-liquid interface, and then decreasing the volume to find the smallest possible angle. Measurements can also be done on a tilted surface, making the angles at one side of the drop different from the other. Viscosity will affect the settling time of the drop, so sometimes it may be advantageous to take a video of the drop rather than a picture, in order to observe the time evolution of the contact angle, as shown in Fig. 1.12.

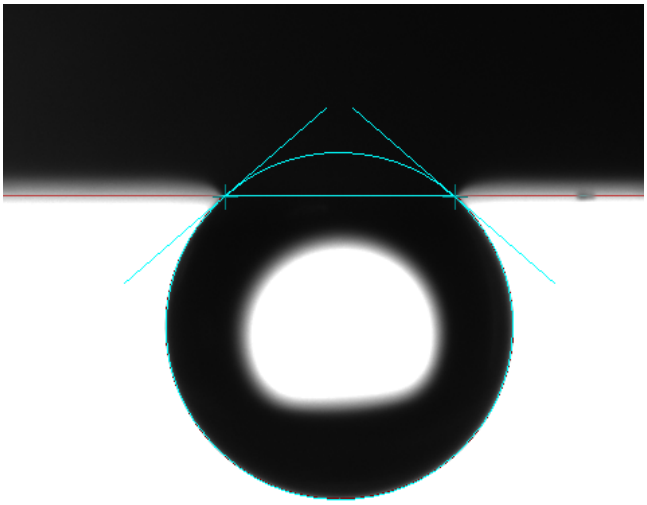

Figure 3.12: Measuring the contact angle of hexadecane oil droplet in water on a sapphire surface using the static sessile drop method.

Chapter 4

Conclusion and further work

The work presented in this thesis is motivated by the idea of a bimetallic plasmonic MIM solar cell, but covers a wider field of nano-related topics. The articles in this thesis can be sorted into three categories: Four articles concerning effects related to the optics of nanostructures, one article related to non-optical effects (wetting) of nanostructures, and one article related to nanotechnology laboratory design. In this chapter the results are summarized very briefly and further work is proposed.

4.1 Optical properties of nanostructures

There are four articles in the first category. The first article simulates optical absorption and scattering of MNPs in water using the commercial software Lumerical, and compares it to experimental results found in available literature. Simulations show that aluminum spheres have a wide absorption range, and 40 nm silver spheres have the most efficient absorption at a single wavelength. Efficient absorption across the whole VIS specter can be achieved by combining sizes and metals. The results largely agree with experiments. Further simulations could be done on nanofluids containing nanoshells, exploring absorption in the NIR. Simulations of particular relevance for several experiments performed in the University of Bergen NanoStructures Group are shapes placed on glass or indium-tin-oxide (ITO) wafers. In particular it would be of value to the development of a solar cell to find a structure configuration with total-absorption, meaning that it absorbs efficiently across the whole solar specter.

The second and third article investigate variables that may affect the optical behavior, namely annealing and fabrication method. In the case of annealing, the particle barely changes shape or size, and yet the extinction peak shifts from ap-

proximately 580 to 520 nm when annealed up to 600^{o} C. Only the surface roughness seems to change slightly. In the third article we compare a sample made with EBL to one made with HCL, and the difference in results are explained by variations in particle size, and the randomness of inter-particle distance in the HCL case. One important aspect which is mentioned in the second article, that could be investigated closer, is how the crystallinity of the metal affects the absorption. For the metals investigated in the three first articles, the size and treatment of the particles only affect optical behavior in a narrow range, except in the case of aluminum spheres. For full VIS-NIR absorption, finding a way to tune it in a wider range should be investigated. A final suggestion for further work is to manufacture and perform optical experiments on a potential total-absorption geometry after designing one in simulations.

The fourth article addresses the optical and electrical response of a nanostructure in a bimetallic MIM device, where the two metals have different work functions. This article is important because it is the first to address the electrical behavior of the proposed EnSol solar cell. The measured current is low, motivating two paths of further work. Firstly, the PCI should be further developed. A tunable high power laser would provide optical and electrical response for different wavelengths, which is desirable. The implementation of a LIA would allow us to measure very low signals. Alternatively, 4-wire sensing could be utilized. Secondly, loss mechanisms should be investigated for the proposed solar cell. What material combinations are best for efficient electron hole separation and transport? How large is the portion of energy which is transfered to heat rather than electron-hole pairs? Can this portion be minimized or utilized? These are all questions that should be answered in order to optimize the efficiency of the solar cell.

4.2 Non-optical properties of nanostructures

Non-optical effects are addressed in one article. The wetting properties of a sapphire surface is investigated in the hope of making a self-cleaning window in an oil-fouling environment. Although we work with non-structured surfaces in this article, the work falls under the category of nanostructure effects since we show that a sapphire's nano-sized features, namely its surface mis-cut, polishing method and initial cleanliness, greatly affects the surface's oleophobic properties. The paper contains wetting angle measurements of water droplets in air and oil droplets under water, in contact with the sapphire surface. The surface hydrophilicity in air is linked to the oleophobicity in water, and by making the surface hydrophilic, it remains cleaner in an oil-fouled environment for longer. Further work involves nanostructuring of the sapphire surface, to see if it can not be made even more

oleophobic, improving the self-cleaning effect further.

4.3 Laboratory design

In the third category one article addresses what is needed to build a clean-room lab, and tricks to make it affordable. By placing non critical processes outside the clean-room, it's size can be decreased significantly. Clean-room cabins are used, which requires less alterations to the building compared to a ceiling filter and perforated floor setup. Dust, temperature and humidity control is energy consuming. By recycling the air, the running cost is reduced. Norway is in it's infancy of tapping into the global industry of nanotechnology. The information in this article may help businesses locally and elsewhere getting a hand in the door of nanoindustry, which may be difficult due to the high start up costs.

Part II

Articles

Energy Conversion and Management 149 (2017) 536–542

Contents lists available at ScienceDirect

Energy Conversion and Management

journal homepage: www.elsevier.com/locate/enconman

A theoretical investigation of the optical properties of metal nanoparticles in water for photo thermal conversion enhancement

Vårin R.A. Holm *, Martin M. Greve, Bodil Holst

Department of Physics and Technology, University of Bergen, Allégaten 55, 5007 Bergen, Norway

ARTICLE INFO

Article history:
Received 22 May 2017
Received in revised form 10 July 2017
Accepted 11 July 2017

Keywords:
Light absorption/scattering
Nanofluid
Metal nanoparticle

ABSTRACT

Nanofluids are used in photo thermal absorbers such as direct absorption solar collectors (DASC) to improve the absorption and heat transfer. A range of experimental studies have investigated the photo thermal conversion in nanofluids based on metal nanoparticles. The photo thermal conversion efficiency depends mainly on the ability of the metal nanoparticle based nanofluid to absorb light which in turn is governed by the particle localized surface plasmon resonance (LSPR). In this article we investigate the optical properties of metal nanoparticles in water, and based on this we judge their suitability for use in water based nanofluids. We simulate the optical properties and provide an overview of the absorption, scattering and extinction properties of solid and spherical aluminum, silver, copper and gold nanoparticles suspended in water. We study nanoparticle diameters between 20 and 140 nm for the wavelength range 300–1350 nm (200–1250 nm for aluminum). We compare our simulation results with the available experimental results presented in the literature, and find good agreement.

1. Introduction

In the chase for cleaner, more efficient energy harvesting, solar energy is an appealing source, being both abundant and free. Between electrical, chemical, and thermal solar energy conversion, thermal is the more simple and straightforward choice [1]. Common photo thermal collectors absorb light utilizing a black body, and transfer the heat to a fluid. The fluid is then transported from the point of absorption to be used directly for heating, or to a generator such as a steam engine to produce electricity. Some examples are flat plate collectors, parabolic troughs and power towers [2]. The collector efficiency is limited by how effectively the heat may be transfered from the black body to the fluid [3]. This limitation can be circumvented by making the liquid absorb the light directly. Such a device is called a direct absorption solar collector (DASC) [4]. Nanofluids may be introduced in non-DASC devices also, such as parabolic troughs [5]. In such cases, a nanofluid may replace the fluid in order to increase absorption in the liquid. Nanoparticles in a liquid will transfer the absorbed energy to the liquid more quickly than that of an idealized black body pipe, since nanoparticles will have a larger surface area in contact with the liquid. Also, the thermal conductivity of the nanoparticles increases with decreasing particle size [6], improving the photo thermal conversion efficiency η.

The photo thermal conversion efficiency depends on the geometric configuration, specific heat, and convection heat transfer, but it is ultimately limited by the optical absorbtion of the nanofluid [7]. In the following we will focus on water as the liquid medium. Water itself is highly transparent and not a great absorber [8]. Metal nanoparticles absorb light through the localized surface plasmon resonance (LSPR). LSPR occurs when the electric field of a photon causes the metal electrons to oscillate, and the photon frequency is matched to cause an amplification of the oscillation, determined by the nanoparticle size and shape, and the dielectric properties of the surrounding medium [9].

In this paper, the absorption of a single particle is presented as a cross section σ_{abs} [nm^2]. The absorption coefficient β_{abs} of a nanofluid is given as

$$\beta_{abs} = \sigma_{abs} N \tag{1}$$

where N is the number of nanoparticles per unit volume. The absorption efficiency Q_{abs} is given as

$$Q_{abs} = \frac{\sigma_{abs}}{A_{np}} \tag{2}$$

where A_{np} is the cross sectional area of the particle (πr^2 for a sphere) [10]. At resonance, the nanoparticle can absorb light from an area which is larger than it's physical area making the efficiency greater

* Corresponding author.
E-mail address: Varin.Andvik@uib.no (V.R.A. Holm).

http://dx.doi.org/10.1016/j.enconman.2017.07.027
0196-8904/

Nomenclature

Abbreviations

AM 1.5	solar spectral irradiance for air mass 1.5 (W m^{-2} nm^{-1})
DASC	direct absorption solar collector
FDTD	finite-difference time-domain
FWHM	full width half maximum
IR	infrared, 1050 nm and longer
LSPR	localized surface plasmon resonance
NIR	near infrared, 700–2500 nm
PML	perfectly matched layer
VIS	visible, 390–700 nm
wl	wavelength (nm)

Symbols

β	coefficient
ϵ	permittivity (m^{-3} kg^{-1} s^4 A^2)
η	photo thermal conversion efficiency
μ	permeability (kg m s^{-2} A^{-2})
σ	cross section (nm^2)
A	area (nm^2)
c	specific heat (m^2 K^{-1} s^{-2})
d	diameter (nm)
E	electric field (kg m s^{-3} A^{-1})
H	magnetic field (A m^{-1})
I	intensity (W m^{-2})
m	mass (kg)
N	number density (particles/nm^3)
P	power (W)
Q	efficiency
t	time (s)
T	temperature (K)
z	zenith angle (°)

Subscripts

abs	absorption
exp	experiments in literature
ext	extinction
l	liquid
lum	lumerical simulation
np	nanoparticle
sca	scattering
sim	simulations in literature

than 1. Eqs. (1) and (2) are valid for the scattering and extinction cross sections, σ_{sca} and σ_{ext} as well, and are related to the absorption cross section by the following definition [10]:

$$\sigma_{ext} = \sigma_{abs} + \sigma_{sca} \tag{3}$$

In the context of photo thermal conversion for nanofluids, scattered light can be absorbed by neighboring nanoparticles. For DASC applications, there is therefore no immediate need to minimize scattering. However, light must be absorbed in order to be converted to heat, so the main objective is to maximize the absorption efficiency. The absorbance spectra of nanofluids are usually measured experimentally using a transmission spectrometer, which in reality measures the extinction. For small nanoparticles, usually less than 30–40 nm (though this is material dependent), scattering is negligible and the terms extinction and absorption are interchangeable [11]. As the nanoparticles becomes larger however, scattering becomes the dominant process.

One should keep in mind that a high absorption efficiency is not necessarily the same as a high photo thermal conversion efficiency, η. η is given as

$$\eta = \frac{(c_l m_l + c_{np} m_{np})}{IA} \frac{\Delta T}{\Delta t} \tag{4}$$

where c_l and c_{np} is specific heat of the liquid and particle respectively, m_l and m_{np} is mass of the liquid and particle respectively, I is solar intensity, A is the illuminated area of the fluid, and ΔT is the temperature rise in the time interval Δt [12]. Some materials may re-emit the absorbed light at longer wavelengths (fluorescence), and some materials may have low thermal conduction despite a high absorption efficiency, thus yielding a low ΔT. For example, Chen et al. observe that the photo thermal conversion efficiency seems to decrease slightly for increasingly larger gold nanoparticles, when investigating spherical gold nanoparticles in water [7].

Theoretical calculations of optical nanostructures can be performed using for example Mie theory [9], Raleigh scattering method [10], or finite difference [13] or finite element simulations in the time or frequency domain, depending on the system one wishes to investigate. In the Raleigh scattering method, the electric field is assumed to be constant over the entire particle, and it is therefore only valid for particles much smaller than the wavelength of radiation. For larger particles, Mie theory can be applied. Mie theory describes the interaction of an electromagnetic plane wave with a homogeneous sphere. For non-spherical particles, discretization of Maxwell's equations may be appropriate. For transient behavior of the electromagnetic field, a time domain approach is desirable. Frequency domain calculations are particularly useful when studying periodic structures. In the following, four examples of Raleigh scattering calculations are given. Metal nanoparticles dispersed in water have been investigated by Saidur et al. [11], who investigated aluminum nanoparticles in the range 1–20 nm suspended in water, and found the absorption peak at approximately 300 nm. Taylor et al. [14] found the extinction peak for 40–200 nm silver spheres in water to be at 400 nm using Maxwell-Garnett modeling. Gorji and Ranjbar investigated silver spheres and found an extinction peak at approximately 390 nm, but did not get corresponding experimental results for 20 nm diameter spheres in water [15]. Khlebtsov et al. investigated 15 nm gold, and 15 and 60 nm silver spheres and found extinction peaks at 515, 380 and 412 nm respectively [16].

In this paper we simulate the absorption and scattering of a solid metal nanoparticle dispersed in water by solving Maxwell's equations using the finite-difference time-domain (FDTD) method in the commercial software package Lumerical [17].

$$\begin{aligned} \frac{\vec{H}\left(t+\frac{\Delta t}{2}\right) - \vec{H}\left(t-\frac{\Delta t}{2}\right)}{\Delta t} &= -\frac{1}{\mu}\nabla \times \vec{E}(t) \\ \frac{\vec{E}(t+\Delta t) - \vec{E}(t)}{\Delta t} &= \frac{1}{\varepsilon}\nabla \times \vec{H}\left(t+\frac{\Delta t}{2}\right) \end{aligned} \tag{5}$$

Eq. (5) show the one dimensional Maxwell's equations solved in the time domain using finite difference approximation [13], where E is the electric field and H is the magnetic field, μ and ϵ are the permeability and permittivity respectively, t is time, and Δt is the time step (i.e. $t = \Delta t n$, where n is an integer). For every increasing time step, the values of E and H are updated from the previous ones. A light source is an area where the electric and magnetic field

components are initiated, from here the fields are free to propagate in three dimensions. Knowing the electric and magnetic fields, the power flow through a virtual surface can be recorded within the simulation space. By strategically placing such virtual surfaces (see methods section) the absorption or scattered power can be found. Finally, the cross section is calculated using $P = \sigma I$ where P is the recorded power flow and I is the source intensity.

We vary the size and metal of the spherical nanoparticle, and investigate the effect of the water on the absorption and scattering. We also investigate the effect of oxidation of aluminum, which is likely to occur in practice. The simulation results are compared to experimental results in literature.

2. Methods

Lumerical FDTD Solutions version 8.16.884 was used for all simulations. The setup is shown in Fig. 1. Simulations are done for gold, silver, copper, and aluminum nanoparticles with diameters d ranging from 20 to 140 nm centered at the origin. In order to simulate the LSPR effect, we start out by defining a FDTD simulation space. The boundaries of this space are perfectly matched layers (PML) which absorb radiation, but can reflect evanescent fields. The size of the FDTD simulation space should be chosen sufficiently large so the structure in question do not interact with the evanescent fields [18]. Here the FDTD simulation space was chosen to be

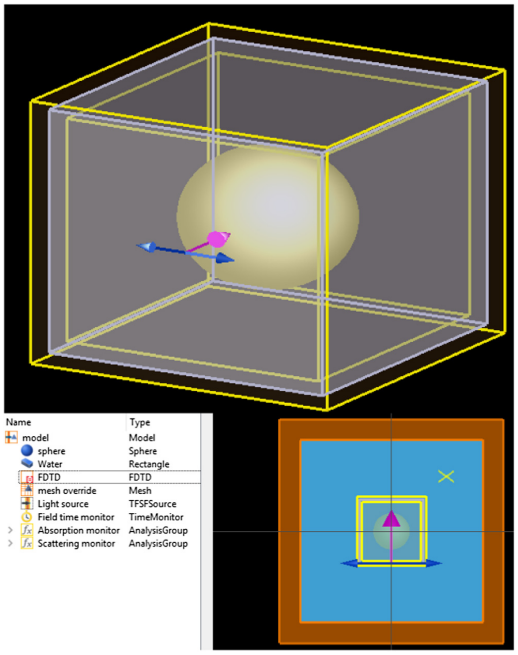

Fig. 1. Simulation geometry. Lumerical [17] is used to simulate the absorption and scattering of light by a metal nanoparticle. The 3D layout (top), simulation elements (bottom left), and the 2D layout in the *XY* plane (bottom right) are shown in the figure. One side of the gray box is defined as the light injection plane, with the magenta arrow showing the propagation direction, and the blue arrows showing the polarization. The absorbed or scattered light is detected by the yellow boxes which are the absorption and scattering monitors. The metal nanoparticle is placed in the center. (For interpretation of the references to color in this figure legend, the reader is referred to the web version of this article.)

700 nm in *X*, *Y* and *Z* direction centered at the origin. This leaves a rather short distance between the sphere and the perfectly matched layers (PML) boundary, but it was chosen to make the total simulation time as short as possible. Simulations with larger FDTD spaces up to 1400 nm were done for 140 nm diameter gold nanoparticles (not shown) to ensure that the size of the FDTD simulation space did not significantly affect the absorption and scattering spectra.

The structure shape (sphere) and material is defined. The sphere is surrounded by water which is set to have the same size as the total simulation space. Lumerical uses experimental data (Palik [19], CRC [20] and Johnson and Christy [21]) as a basis for calculating the refractive index of the chosen material within the desired wavelength range. The mesh size is automatically generated, being inversely proportional to the refractive index. In areas where the refractive index changes rapidly or the geometries are small, the mesh can be overridden with a finer mesh to ensure accurate modeling. The mesh override area used here is the same size as the scattering monitor. The override mesh sizes d*x*, d*y* and d*z* are set to 2.5 nm. This mesh size yield minor ripples on the absorption and scattering spectra for the smallest spheres. They can be eliminated by reducing the mesh size further, though this dramatically increases the simulation time. Since the ripples are small compared to the absorption and scattering spectra, and they quickly disappear as the sphere size increases, the mesh size was not decreased.

The light source is defined as a plane wave in the shape of a box, where the structure must fit completely inside. One side is defined as the injection plane, and the propagation direction and polarization is defined. When the plane wave reaches the boundary of the box, that same plane wave is subtracted, so no light is transmitted past the boundary (apart from the scattered light, which no longer has the same direction as the incident plane wave). The light source has a space of a few nm around its boarders where the values for the electric and magnetic field are non-physical. Simulations on a 40 nm gold nanoparticle in water with a light source where the dimensions vary from 50 to 300 nm were performed (not shown), confirming that the results did not change for various light source sizes. The wavelength range was chosen to be 300–1300 nm for gold, silver and copper, and 200–1200 for aluminum, because although the solar radiation spectrum extends up to 2500 nm there is practically no absorption or scattering above 1200 nm for any of the metal spheres in water investigated here. Simulations of 140 nm gold, silver, copper and aluminum spheres were done with wavelengths up to 2500 nm (not shown) to verify this fact. The wavelength data collection is set so that there is 5 nm between every data point.

Two monitors, one for absorption, and one for scattering are included. A monitor is a box that detects light coming from both inside and outside the box and subtracts the latter from the former. By placing a monitor outside the light source, only the scattered light will reach it. By placing a monitor inside the light source box, it will receive incident light on the outside surface, and transmitted and scattered light on the inside surface, leaving the net difference, i.e. the absorption. The absorption and scattering monitors are placed a small distance of 12.5 nm away from the source boarders.

Finally, a field time monitor is placed at an arbitrary position outside the scattering box and inside the FDTD simulation space to record the time evolution of the electric and/or magnetic fields. This is to verify that the fields have enough time to decay before the maximum simulation time is reached [17].

The settings for the simulation elements are listed in Table 1. All other advanced settings not mentioned here are the same as Lumerical's "Mie Scattering 3D" [17].

Table 1
Simulation parameters. The dimensions column refer to width in both *x*, *y* and *z* direction, all centered at 0 nm.

Parameter	Dim. [nm]	Comments
Metal sphere	20–140	Diameter
Water	700	
FDTD sim. space	700	Sim. temperature is 300 K
Mesh override	270	Override mesh dx = dy = dz = 2.5 nm
Light source	245	Wavelength range is 300–1350 nm (Au, Ag, Cu), 200–1250 nm (Al)
Field time monitor	0	in position 210
Absorption monitor	220	
Scattering monitor	270	

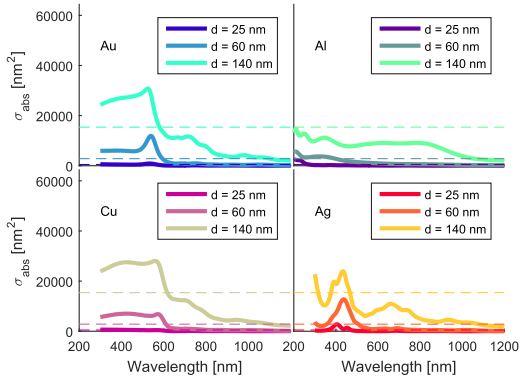

Fig. 2. Absorption spectra. The absorption cross sections for gold, aluminum, copper and silver spheres in water are presented here. The dotted line shows the respective sphere (real) cross sections, illustrating that the spheres absorb from an area which is larger than their physical area, at and near resonance.

3. Results and discussion

Fig. 2 shows the absorption cross section spectra for gold, aluminum, copper and silver spheres in water. The scattering cross sections are included in Fig. 3, and the extinction cross sections is shown in the supplementary material Fig. S1. The dotted line shows the actual (geometrical) cross section of the sphere A_{np}. We see in Fig. 2 that gold and copper absorb some blue light, but the peaks drop rapidly towards the red.[1] The smaller silver nanoparticles have one relatively narrow peak, and as the nanoparticles become larger, another peak emerges, possibly due to quadrupole excitations [22]. Aluminum has wide absorption peaks, making it well suited for absorbing light over a wide range, but we also see that the absorption cross section is low compared to the real sphere cross section. This could be compensated by increasing the volumetric concentration [11]. However, if the concentration is increased past an absorption saturation threshold, the solar energy will be absorbed only at a shallow layer near the surface, increasing the possibility of heat loss [1]. A high particle concentration could also lead to aggregation and sedimentation. In fact, improvements in thermal efficiency only occurs for low concentrations, as reported by Coccia et al. [5] who states that for concentrations higher than 0.01% by weight, the efficiency decreases compared to pure water. The investigation was done on gold nanofluids in a parabolic trough.

[1] For interpretation of color in Figs. 2, 4, and 5, the reader is referred to the web version of this article.

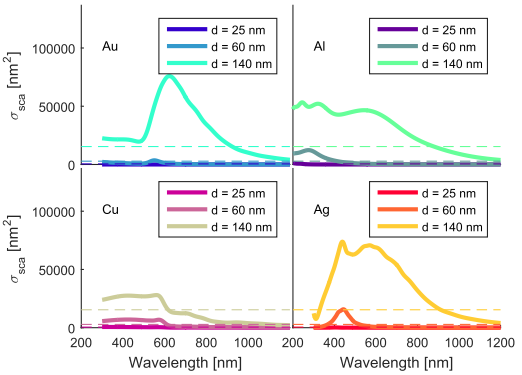

Fig. 3. Scattering spectra. The scattering cross sections for gold, aluminum, copper and silver spheres in water are presented here. The dotted line shows the respective sphere (real) cross sections, illustrating that the spheres scatter from an area which is larger than their physical area, at and near resonance.

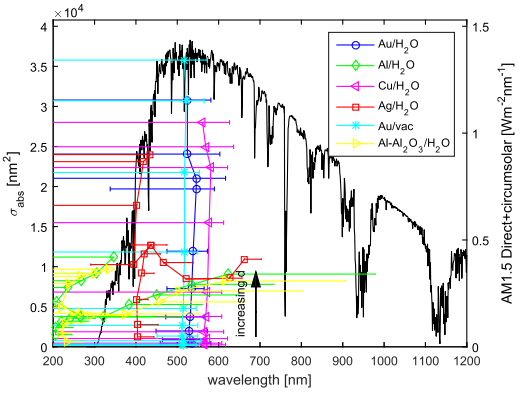

Fig. 4. Absorption cross section peaks and peak wavelengths. Simulations done with Lumerical on gold, aluminum with and without a native oxide layer, copper and silver spheres in water, and gold in vacuum are shown here. The plot shows absorption cross section peaks and peak wavelengths. If the spectrum has multiple peaks, the plot branches out, and the horizontal bars represent the range where the peak has dropped to half its maximum value (there is no bar between branches as the peak does not drop to half value between peaks). The arrow indicates that absorption increases for increasing particle size. The solar spectral irradiance for air mass 1.5 (AM 1.5) [23] is included for comparison.

Figs. 4 and 5 show simulations done with Lumerical for gold, aluminum, copper and silver spheres in water, gold spheres in vacuum, and aluminum spheres in water with a native oxide layer of 3 nm on the surface. In Figs. 4 and 5 only the absorption and scattering cross section peaks and peak wavelengths are presented. The extinction peaks and peak wavelengths are presented in the supplementary material Fig. S2. The horizontal bars represent the width of the peak, indicating the wavelengths where the peak has dropped to half its maximum value. The term full width at half maximum (FWHM) is not used in this context since the peaks are not Gaussian distributions. Further the peaks are strongly assymetrical and many peaks do not drop to half their value for shorter wavelengths. This is due to interband transitions [24]. In these cases the horizontal bars are simply covering the full lower wavelength range. The solar spectral irradiance after traveling through 1.5 air mass (corresponding to a solar zenith angle of $z = 48.2°$ measured at sea level) is included.

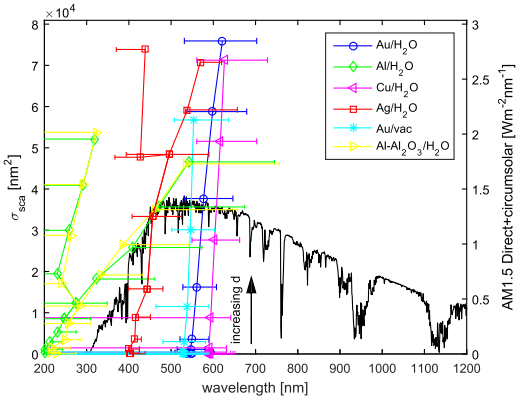

Fig. 5. Scattering cross section peaks and peak wavelengths. Simulations done with Lumerical on gold, aluminum with and without a native oxide layer, copper and silver spheres in water, and gold in vacuum are shown here. The plot shows scattering cross section peaks and peak wavelengths. If the spectrum has multiple peaks, the plot branches out, and the horizontal bars represent the range where the peak has dropped to half its maximum value (there is no bar between branches as the peak does not drop to half value between peaks). The arrow indicates that scattering increases for increasing particle size. The solar spectral irradiance for air mass 1.5 (AM 1.5) [23] is included for comparison.

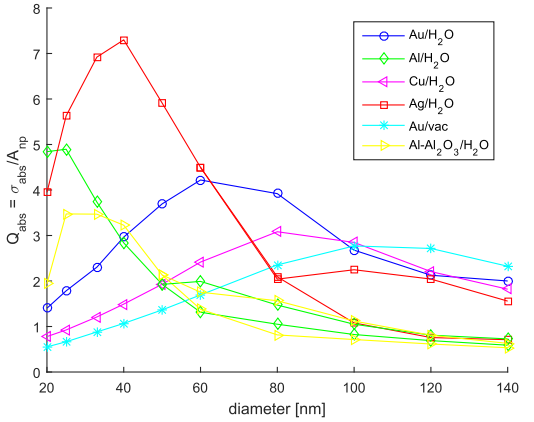

Fig. 6. Absorption efficiencies. The efficiencies are calculated using Eq. (2) for various sphere sizes. (The peak values of σ_{abs} are used.)

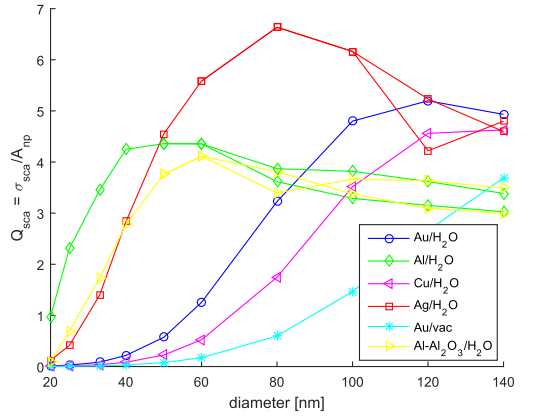

Fig. 7. Scattering efficiencies. The efficiencies are calculated using Eq. (2) for various sphere sizes. (The peak values of σ_{sca} are used.)

The scattering cross section is larger than the absorption cross section for particles larger than 100, 100, 60, and 40 nm for gold, copper, silver, and aluminum respectively, and 120 and 50 nm for gold in vacuum and aluminum/aluminum oxide respectively. The complete set of all absorption, scattering and extinction spectra of spheres ranging from 20 to 140 nm for gold, silver, copper, aluminum and aluminum with 3 nm native oxide layer in water, and gold in vacuum is presented in the supplementary material Fig. S4.

Again, we see that gold, in water and in vacuum, and copper have essentially no absorption in the near infrared (NIR) and infrared (IR) range. In order to absorb light at longer wavelengths with these materials, one could use nanoshells, a metal particle with a dielectric core, of various sizes [1,25,26]. Alternatively, one could use other materials than metals, such as Vakili et al. who use graphene nanoplatelets in water to achieve absorption over the entire visible (VIS) range [27], or Han et al. who use carbon black aqueous nanofluids to absorb across the VIS-NIR range [28].

The absorption cross section peak increases with increasing particle size for all materials. For both aluminum and silver, two absorption peaks at different wavelengths are observed (for spheres larger than 60 nm for aluminum, and 100 nm for silver). This is beneficial when trying to absorb over the entire VIS range, however, this is not the size range where the absorption is most efficient for these materials, as we shall discuss later.

To investigate the effect of water, the absorption and scattering of gold spheres in vacuum is also included in Figs. 4 and 5. The absorption cross section peak wavelength is slightly blue-shifted in vacuum, however the largest difference is the peak amplitude, which is considerably lower in vacuum. This shows that water is beneficial to the absorption proses, due to the difference in refractive index.

Figs. 6 and 7 show the absorption and scattering efficiencies (Eq. (2) based on the cross section peak) as a function of particle size. The extinction efficiencies are shown in the supplementary material Fig. S3. Although the 40 nm silver sphere has the highest Q_{abs} value, the peak is quite narrow. High efficiency absorption across the entire VIS range can be achieved by combining materials and geometries, i.e. different nanoparticle shapes.

Since aluminum quickly develops a native oxide layer on it's surface, a simulation of aluminum spheres with a 3 nm aluminum oxide surface layer is included. The layer's effect is only dominant for small nanoparticles (less than 30 nm), where the absorption efficiency becomes increasingly smaller compared to pure aluminum.

In order to test the validity of our simulations, we compare them, where available, to experimental results in Table 2 and to other simulations in Table 3. The simulations done here do not consider particle interaction and aggregation, since most of the experimental work we compare out results to have very low concentrations, and therefore negligible particle-particle interaction. They are below 0.01% by volume for all references included in Table 2 except Xuan et al. [1] who has 1% volume concentration. Tsai et al. [30] and Tsuji et al. [34] does not provide concentrations. All simulation peak wavelengths wl_{lum}^{max} are within 15 nm of the experimental peak wavelengths wl_{exp}^{max} given in literature, except

Table 2
Comparison of results from experimental articles with Lumerical simulation results. The column marked wl_{exp}^{max} show the experimental peak wavelengths (exp, max) reported in literature, and the column marked wl_{lum}^{max} show the simulation peak wavelength (lum, max) presented in this paper for the same nanoparticle size and material. The diameter ranges are taken from the articles. The wavelengths are read off spectra in the original articles and the error is an estimated reading error. The error on the Lumerical simulations stem from the fact that simulations were done in steps of 5 nm.

Experimental articles	Material	d [nm]	wl_{exp}^{max} [nm]	$wl_{lum}^{max} \pm 2.5$ [nm]
Chen et al. [7]	Au/H_2O	25 ± 9	529 ± 10	531
		33 ± 13	535 ± 10	528
		40 ± 12	544 ± 10	531
Jin et al. [29]	Au/H_2O	~20	526 ± 10	535
Zhang et al. [12]	Au/H_2O	10–30	520 ± 10	528–535
Tsai et al. [30]	Au/H_2O	21 ± 13	529 ± 10	535
Chen et al. [31]	Au/H_2O	~10	521 ± 10	531
	Ag/H_2O	~30	408 ± 10	402
Chen et al. [32]	Ag/H_2O	~53	481 ± 10	418
Xuan et al. [1]	Ag/H_2O	n.a. (20–140)	500 ± 100	(402–573)
Taylor et al. [14]	Ag/H_2O	40–200(140)	400 ± 20	414–(573)
Sato et al. [33]	Ag/H_2O	(20)	410	(402)
Tsuji et al. [34]	Ag/H_2O	10–30	410 ± 10	408
Phuoc et al. [35]	Ag/H_2O	15–30	393–397	402–408
Chang et al. [36]	Cu/H_2O	150–450	270 ± 10	621

Table 3
Comparison of simulation articles with Lumerical simulation results. The column marked wl_{sim}^{max} show the simulated peak wavelengths (sim, max) reported in literature, and the column marked wl_{lum}^{max} show the simulation peak wavelength (lum, max) presented in this paper for the same nanoparticle size and material. The wavelengths are read off spectra in the original articles and the error is an estimated reading error. The error on the Lumerical simulations stem from the fact that simulations were done in steps of 5 nm.

Simulation articles	Material	d [nm]	wl_{sim}^{max} [nm]	$wl_{lum}^{max} \pm 2.5$ [nm]
Khlebtsov et al. [16]	Au/H_2O	15	515 ± 10	528
	Ag/H_2O	60	412 ± 10	441
	Ag/H_2O	15	380 ± 10	408
Taylor et al. [14]	Ag/H_2O	40–200(140)	400 ± 10	414–(573)
Gorji and Ranjbar [15]	Ag/H_2O	20	390 ± 10	402
Saidur et al. [11]	Al/H_2O	1–20	300 ± 100	205

the 53 nm silver spheres reported by Chen et al. [32], and the copper nanofluid presented by Chang et al. [36]. The deviation for the silver nanofluid could be explained by aggregation or non spherical nanoparticles in the experimental sample, which could cause the extinction spectrum to redshift. In the copper nanofluid case, our simulations does not include the whole size range reported by Chang.

4. Conclusions

In this paper, we have investigated the absorption and scattering properties in the range 300–1350 nm (200–1250 nm for aluminum) for nanofluids consisting of metal nanoparticles (gold, silver, aluminum and copper) ranging from 20 to 140 nm in diameter, suspended in water. We compare our simulations with existing experimental results and find good agreement. Our simulations show that aluminum, despite a low absorption efficiency, and silver nanoparticles above 100 nm are particularly suited for absorption over a large wavelength range in the VIS. High efficiency absorption across the entire VIS range can be achieved by combining materials and geometries.

Appendix A. Supplementary material

Supplementary data associated with this article can be found, in the online version, at http://dx.doi.org/10.1016/j.enconman.2017.07.027.

References

[1] Xuan Y, Duan H, Li Q. Enhancement of solar energy absorption using a plasmonic nanofluid based on TiO2/Ag composite nanoparticles. RSC Adv 2014;4:16206–13. http://dx.doi.org/10.1039/C4RA00630E.

[2] Kalogirou SA. Solar thermal collectors and applications. Prog Energy Combust Sci 2004;30(3):231–95. http://dx.doi.org/10.1016/j.pecs.2004.02.001. <http://www.sciencedirect.com/science/article/pii/S0360128504000103> .

[3] Otanicar TP, Phelan PE, Prasher RS, Rosengarten G, Taylor RA. Nanofluid-based direct absorption solar collector. J Renew Sustain Energy 2010;2(3):033102. http://dx.doi.org/10.1063/1.3429737.

[4] Minardi JE, Chuang HN. Performance of a black liquid flat-plate solar collector. Sol Energy 1975;17(3):179–83. http://dx.doi.org/10.1016/0038-092X(75)90057-2. <http://www.sciencedirect.com/science/article/pii/0038092X75900572> .

[5] Coccia G, Nicola GD, Colla L, Fedele L, Scattolini M. Adoption of nanofluids in low-enthalpy parabolic trough solar collectors: numerical simulation of the yearly yield. Energy Convers Manage 2016;118:306–19. http://dx.doi.org/10.1016/j.enconman.2016.04.013. <http://www.sciencedirect.com/science/article/pii/S0196890416302539> .

[6] Wang X-Q, Mujumdar AS. Heat transfer characteristics of nanofluids: a review. Int J Therm Sci 2007;46(1):1–19. http://dx.doi.org/10.1016/j.ijthermalsci.2006.06.010. <http://www.sciencedirect.com/science/article/pii/S1290072906001190> .

[7] Chen M, He Y, Zhu J, Kim DR. Enhancement of photo-thermal conversion using gold nanofluids with different particle sizes. Energy Convers Manage 2016;112:21–30. http://dx.doi.org/10.1016/j.enconman.2016.01.009. <http://www.sciencedirect.com/science/article/pii/S019689041600025X> .

[8] Otanicar TP, Phelan PE, Golden JS. Optical properties of liquids for direct absorption solar thermal energy systems. Sol Energy 2009;83(7):969–77. http://dx.doi.org/10.1016/j.solener.2008.12.009. <http://www.sciencedirect.com/science/article/pii/S0038092X08003496> .

[9] Maier SA. Plasmonics: fundamentals and applications. Springer; 2007.

[10] Bohren CF, Huffman DR. Extinction. Wiley VCH Verlag GmbH; 2007. http://dx.doi.org/10.1002/9783527618156.ch11. pp. 286–324.

[11] Saidur R, Meng T, Said Z, Hasanuzzaman M, Kamyar A. Evaluation of the effect of nanofluid-based absorbers on direct solar collector. Int J Heat Mass Transfer 2012;55(21):5899–907. http://dx.doi.org/10.1016/j.ijheatmasstransfer.2012.05.087. <http://www.sciencedirect.com/science/article/pii/S0017931012004188> .

[12] Zhang H, Chen H-J, Du X, Wen D. Photothermal conversion characteristics of gold nanoparticle dispersions. Sol Energy 2014;100:141–7. http://dx.doi.org/10.1016/j.solener.2013.12.004. <http://www.sciencedirect.com/science/article/pii/S0038092X13005215> .

[13] Sullivan DM. Electromagnetic simulation using the FDTD method. Wiley-IEEE Press; 2000. <http://ieeexplore.ieee.org/xpl/bkabstractplus.jsp?OtherFormats &bkn=5263542#OtherFormats> .

[14] Taylor RA, Phelan PE, Otanicar TP, Adrian R, Prasher R. Nanofluid optical property characterization: towards efficient direct absorption solar collectors.

Nanoscale Res Lett 2011;6(1):225. http://dx.doi.org/10.1186/1556-276X-6-225.
[15] Gorji TB, Ranjbar A. A numerical and experimental investigation on the performance of a low-flux direct absorption solar collector (dasc) using graphite, magnetite and silver nanofluids. Sol Energy 2016;135:493–505. http://dx.doi.org/10.1016/j.solener.2016.06.023. <http://www.sciencedirect.com/science/article/pii/S0038092X1630202X> .
[16] Khlebtsov NG, Trachuk LA, Mel'nikov AG. The effect of the size, shape, and structure of metal nanoparticles on the dependence of their optical properties on the refractive index of a disperse medium. Opt Spectrosc 2005;98(1):77–83. http://dx.doi.org/10.1134/1.1858043.
[17] Lumerical. <https://www.lumerical.com/ [accessed: 2016-08-31].
[18] Lumerical. Discussion and results. <https://kb.lumerical.com/en/particle_scattering_nanowire_discussion_results.html> [accessed: 2017-05-03].
[19] Palik ED, editor. Handbook of optical constants of solids. Academic Press; 1998.
[20] Haynes WM, editor. CRC handbook of chemistry and physics. CRC Press; 2015.
[21] Johnson PB, Christy RW. Optical constants of the noble metals. Phys Rev B 1972;6:4370–9. http://dx.doi.org/10.1103/PhysRevB.6.4370. <https://link.aps.org/doi/10.1103/PhysRevB.6.4370> .
[22] Zhou F, Li Z-Y, Liu Y, Xia Y. Quantitative analysis of dipole and quadrupole excitation in the surface plasmon resonance of metal nanoparticles. J Phys Chem C 2008;112(51):20233–40. http://dx.doi.org/10.1021/jp807075f.
[23] American Society for Testing and Materials. Terrestrial reference spectra for photovoltaic performance evaluation ASTM G173-03, http://rredc.nrel.gov/solar/spectra/am1.5/#refs; 2003.
[24] Pinchuk A, von Plessen G, Kreibig U. Influence of interband electronic transitions on the optical absorption in metallic nanoparticles. J Phys D: Appl Phys 2004;37(22):3133. <http://stacks.iop.org/0022-3727/37/i=22/a=012> .
[25] Wu Y, Zhou L, Du X, Yang Y. Optical and thermal radiative properties of plasmonic nanofluids containing core-shell composite nanoparticles for efficient photothermal conversion. Int J Heat Mass Transfer 2015;82:545–54. <http://www.sciencedirect.com/science/article/pii/S0017931014009983> .
[26] Cole JR, Halas NJ. Optimized plasmonic nanoparticle distributions for solar spectrum harvesting. Appl Phys Lett 2006;89(15):153120. http://dx.doi.org/10.1063/1.2360918.
[27] Vakili M, Hosseinalipour S, Delfani S, Khosrojerdi S. Photothermal properties of graphene nanoplatelets nanofluid for low-temperature direct absorption solar collectors. Sol Energy Mater Sol Cells 2016;152:187–91. http://dx.doi.org/10.1016/j.solmat.2016.01.038. <http://www.sciencedirect.com/science/article/pii/S0927024816000519> .
[28] Han D, Meng Z, Wu D, Zhang C, Zhu H. Thermal properties of carbon black aqueous nanofluids for solar absorption. Nanoscale Res Lett 2011;6(1):457. http://dx.doi.org/10.1186/1556-276X-6-457.
[29] Jin H, Lin G, Bai L, Amjad M, Filho EPB, Wen D. Photothermal conversion efficiency of nanofluids: an experimental and numerical study. Sol Energy 2016;139:278–89. http://dx.doi.org/10.1016/j.solener.2016.09.021. <http://www.sciencedirect.com/science/article/pii/S0038092X16304273> .
[30] Tsai C, Chien H, Ding P, Chan B, Luh T, Chen P. Effect of structural character of gold nanoparticles in nanofluid on heat pipe thermal performance. Mater Lett 2004;58(9):1461–5. http://dx.doi.org/10.1016/j.matlet.2003.10.009. <http://www.sciencedirect.com/science/article/pii/S0167577X03008036> .
[31] Chen M, He Y, Huang J, Zhu J. Synthesis and solar photo-thermal conversion of au, ag, and au-ag blended plasmonic nanoparticles. Energy Convers Manage 2016;127:293–300. http://dx.doi.org/10.1016/j.enconman.2016.09.015. <http://www.sciencedirect.com/science/article/pii/S0196890416307932> .
[32] Chen M, He Y, Zhu J, Wen D. Investigating the collector efficiency of silver nanofluids based direct absorption solar collectors. Appl Energy 2016;181:65–74. http://dx.doi.org/10.1016/j.apenergy.2016.08.054. <http://www.sciencedirect.com/science/article/pii/S0306261916311412> .
[33] Sato M, Abe Y, Urita Y, Di Paola R, Cecere A, Savino R. Thermal performance of self-rewetting fluid heat pipe containing dilute solutions of polymer-capped silver nanoparticles synthesized by microwave-polyol process. Int J Transp Phenomena 2011;12:339–45. <https://www.researchgate.net/publication/267736822_Thermal_Performance_of_Self-rewetting_Fluid_Heat_Pipe_Containing_Dilute_solutions_of_Polymer-capped_Silver_Nanoparticles_Synthesized_by_Microwave-Polyol_Process> .
[34] Tsuji T, Okazaki Y, Higuchi T, Tsuji M. Laser-induced morphology changes of silver colloids prepared by laser ablation in water: enhancement of anisotropic shape conversions by chloride ions. J Photochem Photobiol A: Chem 2006;183(3):297–303. http://dx.doi.org/10.1016/j.jphotochem.2006.05.021. Proceedings of 12th international conference on unconventional photoactive systems (UPS-12) <http://www.sciencedirect.com/science/article/pii/S1010603006002905> .
[35] Phuoc TX, Soong Y, Chyu MK. Synthesis of Ag-deionized water nanofluids using multi-beam laser ablation in liquids. Opt Lasers Eng 2007;45(12):1099–106. http://dx.doi.org/10.1016/j.optlaseng.2007.06.005. <http://www.sciencedirect.com/science/article/pii/S0143816607001194> .
[36] Chang H, Wu Y, Chen X, Kao M. Fabrication of Cu based nanofluid with superior dispersion. Natl Taipei Univ Technol J 2000;5:201–8. <http://citeseerx.ist.psu.edu/viewdoc/citations;jsessionid=AB79C8DE69E8B54A7C17808EBE69C38F?doi=10.1.1.505.8793> .

Supplementary reference

Supplementary information: A theoretical investigation of the optical properties of metal nanoparticles in water for photo thermal conversion enhancement

Vårin Renate Andvik Holm[a], Martin M. Greve[a], Bodil Holst[a]

[a]*Department of Physics and Technology, University of Bergen, Allégaten 55, 5007 Bergen, Norway*

Here we provide supplementary information for "A theoretical investigation of the optical properties of metal nanoparticles in water for photo thermal conversion enhancement".

Figure S1 show extinction cross sections for gold, aluminum, copper and silver spheres in water. Figure S2 show the extinction peaks and peak wavelengths. The horizontal bars represent the wavelength range between the two wavelengths where the peak has dropped to half its maximum value. In some cases the peak stays above this value for the whole small wavelength range. This is discussed in the main text. Figure S3 show the extinction efficiencies for various sphere sizes. Finally, all the absorption, scattering and extinction spectra of spheres ranging from 20-140 nm for gold, silver, copper, aluminum and aluminum with 3 nm native oxide layer in water, and gold in vacuum are presented in Fig. S4. These spectra have been used to compile all other figures in the paper.

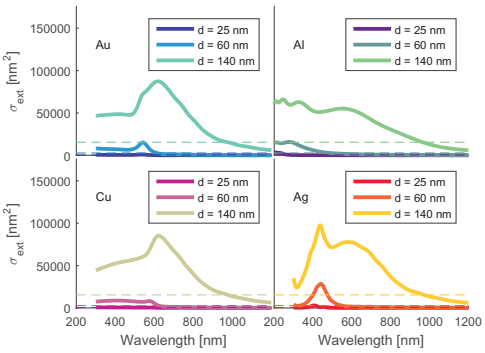

Figure S1: Extinction spectra. The extinction cross section for gold, aluminum, copper and silver spheres in water are shown here. The dotted line show the respective sphere (real) cross sections, illustrating that the spheres extinct from an area which is larger than their physical area, at and near resonance.

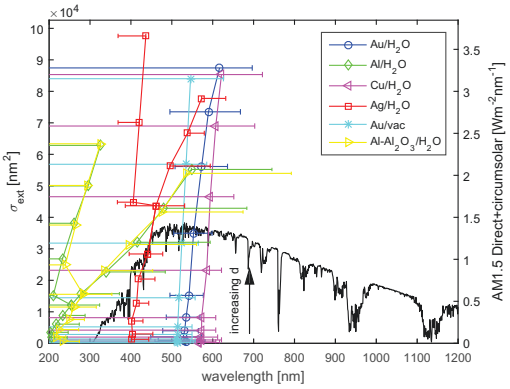

Figure S2: Extinction peaks and peak wavelengths. Simulations done with Lumerical on gold, aluminum with and without a native oxide layer, copper and silver spheres in water, and gold in vacuum are shown here. The plot shows extinction cross section peaks and peak wavelengths. If the spectrum has multiple peaks, the plot branches out, and the horizontal bars represent the range where the peak has dropped to half its maximum value (there is no bar between branches as the peak does not drop to half value between peaks). The arrow indicates that the extinction increases for increasing particle size. The solar spectral irradiance (AM 1.5) is included for comparison.

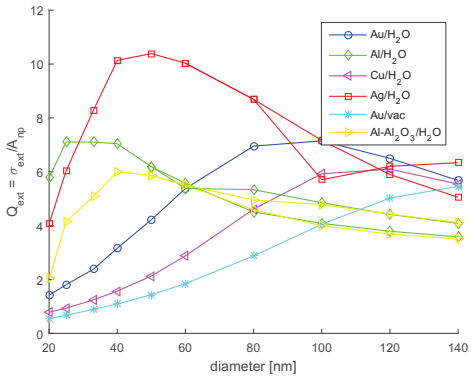

Figure S3: Extinction efficiencies. The extinction efficiencies are calculated for various sphere sizes. (The peak values of σ_{ext} are used).

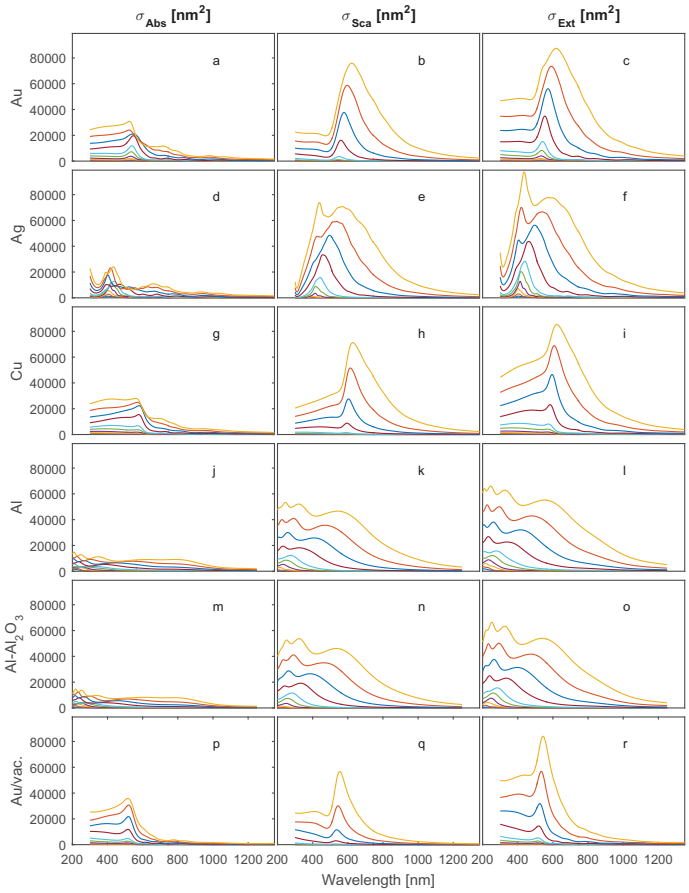

Figure S4: Absorption, scattering and extinction spectra. The absorption (a, d, g, j, m, p), scattering (b, e, h, k, n, q), and extinction (c, f, i, l, o, r) cross sections for gold (a, b, c), silver (d, e, f), copper (g, h, i), aluminum (j, k, l), and aluminum with 3 nm native oxide layer (m, n, o) in water, and gold in vacuum (p, q, r) are shown here for sphere sizes ranging from 20 (blue) - 140 (yellow) nm.

Temperature induced color change in gold nanoparticle arrays: Investigating the annealing effect on the localized surface plasmon resonance

Vårin R. A. Holm,[a] Martin M. Greve, and Bodil Holst
Department of Physics and Technology, University of Bergen, Allegaten 55, 5007 Bergen, Norway

(Received 23 June 2016; accepted 7 September 2016; published 27 September 2016)

The localized surface plasmon resonance (LSPR) effect in metal nanoparticles is important for a range of applications, including photovoltaics and sensors. The actual LSPR effect is difficult to predict, because it can vary strongly with the size, shape, surface structure, and surrounding media of the nanoparticles. In order to understand this better, more experimental data are needed. Here, the authors present a study of the LSPR effect in macroscopic two-dimensional square arrays of gold nanoparticles, 50–80 nm in diameter with a pitch of approximately 160 nm, fabricated on borosilicate substrates. The arrays were exposed to different annealing temperatures in steps of 50 up to 600 °C. The authors observe an irreversible blue-shift of the LSPR extinction peak, from around 580 to around 520 nm at annealing temperatures of only 450 °C, an effect clearly visible to the naked eye. The authors also present measurements of the shape of the nanoparticles at the different annealing steps. These measurements were obtained using a combination of scanning electron microscopy (SEM) and atomic force microscopy (AFM). A carefully indexed pattern allowed us to measure the exact same nanoparticles with separate AFM and SEM instruments. The only clear effect that can be observed is that the nanoparticles appear to get smoother with annealing. Our results demonstrate that seemingly minor changes in the metal nanoparticle appearance can lead to a strong change in the LSPR effect. Our results also open up for potential applications in temperature sensing. The fact that the effect of temperature exposure can be observed with the naked eye without any need of electronic readout or power supply is particularly advantageous.
 [http://dx.doi.org/10.1116/1.4963153]

I. INTRODUCTION

A metal nanoparticle (MNP) is smaller than the wavelength of visible light. If the nanoparticle is small enough, the electric field in the incoming light will act uniformly over the whole nanoparticle, displacing the electrons. Combined with the restoring force of the atom cores, this system can be described as an oscillator with a resonance frequency.[1] This effect is referred to as the localized surface plasmon resonance (LSPR) effect, and the macroscopic color of a MNP is determined by the wavelength at which the resonances occur. Varying the shape, size, material, and surrounding medium of the nanoparticles will result in different resonance frequencies. The shape and dielectric function may in turn be affected by external effects applied postfabrication, such as annealing.

There are some investigations on the effect of annealing of nanoparticles of various materials.[2–7] Cai *et al.*[8] reports first a blue-shift and then a red-shift of the absorption peak when annealing 3–5 nm sized silver nanoparticles dispersed within the pores of monolithic mesoporous silica, at temperatures between 500 and 800 °C. Bi *et al.*[9] demonstrate that by alternate annealing in air and H_2, silver nanoparticles dispersed within pores of monolithic mesoporous silica change color. This is attributed to a redox of the Ag nanoparticles, and the process is reversible. Oxidation is not likely to be an issue when annealing gold. Annealing can cause nanoparticles to sink into a glass substrate as reported by Karakouz *et al.*[10] This would mean that a larger portion of the nanoparticle will be surrounded by the substrate rather than air, changing the dielectric function of the surrounding medium and leading to an increase in the refractive index. The quasistatic approximation description of the interaction between a nanoparticle and an electromagnetic field predicts the position of the LSPR to depend on the dielectric function of the surrounding medium[1] so that we would expect a red-shift, should the nanoparticles sink into the substrate. This is assuming that there are no structural changes to the nanoparticles. Bae *et al.*[11] and Jensen *et al.*[12] reports a red-shift for a decrease in nanoparticle height.

Hulteen *et al.*[13] observe a blue-shift when annealing gold nanoparticles located within the 45 nm sized pores of porous alumina membranes up to 400 °C. They present TEM images which shows that the gold nanoparticles goes from being irregular to becoming denser and more uniform, especially the smaller ones. Kessentini *et al.*[14] have investigated the effect of surface roughness on the LSPR, theoretically. They predict a blue shift of approximately 25 nm, for a cylinder with 50 nm diameter and 20 nm height, and a surface root mean square roughness going from 1.6 to 0 nm. Qian *et al.*[15] calculate theoretically that the extinction spectrum blue shift for hollow gold cubes when the corners are rounded. Liu *et al.*[16] show the same for bipyramids when the tips are rounded using finite-difference time-domain (FDTD) simulations; the absorption peak is shifted 40 nm by a change in the radius of curvature from 4.4 to 2.0 nm. All of these examples demonstrate that a change in shape, even a really small, subtle change, can affect the extinction peak significantly.

[a]Electronic mail: varin.andvik@uib.no

Here, we present an experimental study of the color change of gold nanoparticle arrays when annealed at a range of temperatures. We combine spectral measurements with atomic force microscopy (AFM) and scanning electron microscopy (SEM) to investigate how the color change correlates with the alteration of the nanoparticle size or shape.

II. METHOD

A total of six gold nanoparticle arrays were made, following the manufacturing procedure used by Greve *et al.*[17] The samples were labeled A–F. Samples A–E were prepared on $24 \times 24\,\mathrm{mm}^2$ borosilicate glass substrates (Menzel-Gläser). Sample F will be discussed later. After an initial cleaning using acetone, methanol, and isopropanol, the glass substrates were spin-coated with PMMA to a thickness of approximately 190 nm. A 3 nm chromium thin film was deposited on top of the PMMA using Temescal FC-2000 electron beam evaporation (EBE) to make the substrates conductive for electron beam lithography (EBL). Raith eLINE EBL was used for patterning the samples A–E with square arrays of 2 nm pixels. A pattern resulting in holes of approximately 50–80 nm diameter and an interparticle distance of 160 nm was patterned. The interparticle distance was chosen to avoid optical coupling between the MNPs.[18] A total area of $4 \times 4\,\mathrm{mm}^2$ was patterned. The dose was 0.0090 pC per dot, the acceleration voltage was 15 kV, and the beam aperture was 30 μm in diameter, resulting in a beam current of 0.175 nA and a dwell time per pixel of 0.051429 ms. The working distance was approximately 10.7 mm.

After patterning, the chromium was removed using a chromium etchant (Transene chromium etchant 1020). The PMMA exposed by the electron beam was removed by submerging the samples for two minutes in developer (Micro Resist Technology developer mr-Dev 600). Approximately 25 nm gold [estimated using a quartz crystal microbalance (QCM)] was deposited using EBE. In order to avoid undesired optical effects no adhesion promoting layer was used for the gold film. It was still possible to produce large, high quality arrays. Lift off was done by soaking the sample in *N*-methyl-2-pyrrolidone heated to 80 °C for 2 h. This removed the PMMA, leaving only the gold nanoparticles on the substrate. Figure 1 shows SEM images of samples A and D, taken both perpendicularly and tilted at a 45° angle. It has been discussed in the literature that gold does not adhere well to glass substrates, but this was not an issue for the sample preparation and optical experiments presented here. However, it became an issue for the AFM characterization which will be discussed in Sec. II.

Annealing was done in a Nabertherm GmbH (LE2/11/R6) furnace. The furnace operates in air at atmospheric pressure and was preheated to the set temperature before a sample was inserted. Annealing was done for 5 min for each temperature.

To characterize the color change resulting from annealing, a spectral analysis was performed. For samples with little or no scattering, the terms extinction and absorption are interchangeable. The extinction for samples with low reflectance is given as

$$\text{extinction} = -\log(t), \tag{1}$$

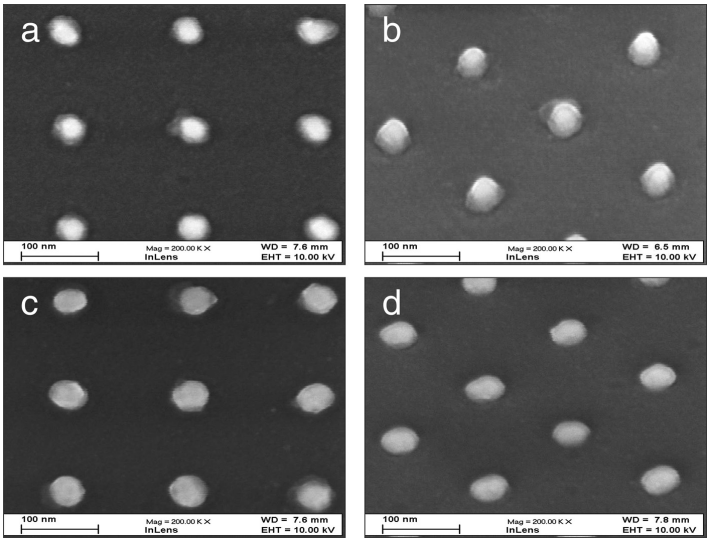

FIG. 1. (a) SEM image of sample A, showing the unannealed square array of gold nanoparticles with 66 nm diameter, 25 nm height, and 160 nm particle distance. (b) SEM image of sample A, taken at a 45° angle. (c) SEM image of sample D, which has been annealed at 450 °C. (d) SEM image of sample D, taken at a 45° angle. The hemispherical shape of the particle can be seen. The samples were coated with 3 nm chromium before imaging.

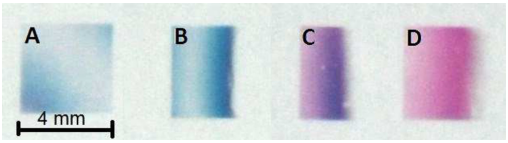

FIG. 2. (Color online) Macroscopic scale optical image of gold nanoparticle arrays. Sample A is not annealed, B is annealed at 150 °C, C at 300 °C, and D at 450 °C.

where t is transmittance through the sample.[1,18] This was measured on samples A–E using a Filmetrics F10-RT thin film analyzer. This instrument has a wavelength range from 380 to 1050 nm. Illumination from a white light source with normal incidence on the sample, and the transmitted spectrum was detected and analyzed using a spectrometer. Each measurement has been background corrected by subtracting the bare glass substrate signal, and five measurements were done for each temperature at random positions within the MNP array. To determine the peak extinction, each spectrum was fitted with a two term Gaussian model using MATLAB. Both Lorentzian[19,20] and Gaussian[21,22] fittings are commonly used in the literature. Macroscopic images of samples A-D were taken using a Nikon D80 digital camera (see Fig. 2).

After the optical measurements had been completed, the samples were coated with 3 nm chromium to avoid charging during the SEM investigation, where the size of the nanoparticles in the respective arrays was determined. Sixteen images were taken, 1.4 mm from all four corners (1 mm from the edges) for each of the $4 \times 4\,\text{mm}^2$ MNP arrays. Every image contains 35 nanoparticles, resulting in 560 nanoparticles imaged for each of the samples A–E. Using IMAGEJ software,[23] the diameter and area was calculated for all the nanoparticles. The results are presented in Table I.

Sample F was designed to be used for detailed AFM and SEM analysis. To avoid charging effects in the SEM images, a $20 \times 20\,\text{mm}^2$ ITO coated glass (about 350 nm thick) with 15–30 Ω/cm resistance was used as the substrate. We cannot exclude that this change in substrate can lead to a change in the interfacial energy between gold and the substrate, thus leading to a change in the wetting behavior of gold on these surfaces. We did notice that it appeared to be slightly easier to scrape off particles from the ITO covered substrate in the AFM. The same PMMA thickness was used for samples A–E, but no chromium layer is needed since the substrate is now conducting. The EBL pattern used was also changed, so that the nanoparticles only cover $30 \times 30\ \mu\text{m}^2$, split into 15×15 arrays, each with 10×10 nanoparticles. Each array was configured with a marker in the form of a selectively missing nanoparticle, so that every array and thereby every nanoparticle is uniquely identifiable. In addition, the nanoparticle arrays are surrounded by an area of $3\,\text{mm}^2$ filled with arrows, 5 or 10 μm in size depending on whether they are closer or further from the arrays than 0.5 mm, respectively. All arrows are pointing in the direction of the nanoparticle arrays and are included to aid in locating the arrays. The arrows were necessary because our AFM (Anfatech "Eddy") does not have built in optics for sample positioning or similar; hence, the arrows were vital for locating the gold nanoparticle arrays. After EBL patterning, the sample was developed, and 35 nm gold was deposited with EBE. A thicker gold layer was used (35 nm) in order to give a larger topographic change for the AFM, where particles are relative to the substrate. The lift-off step is the same as for samples A–E. See Fig. 3 for an overview SEM image of sample F.

AFM characterization of sample F was performed using Anfatech "EDDY" in the Kelvin probe mode (KPFM). KPFM was used because here the scanning probe retains a relatively large distance from the surface and it was found that using both dynamic and contact mode settings resulted in nanoparticles being scraped off the surface. The instrument used a NSC18/Ti-Pt cantilever from Ultrasharp, which has a 3.5 N/m and radius of curvature less than 35 nm. The drive amplitude was set to 2.0 V. Our AFM could not resolve the lateral dimensions of the nanoparticles. Therefore, the AFM is only used for measuring the topological response in

TABLE I. Average and standard deviation values of the diameter and area for samples A–F calculated using IMAGEJ software and SEM images is presented. Five hundred and sixty nanoparticles were measured for each sample (samples A–E). For sample F, the same 99 nanoparticles were measured after each annealing step. Samples A–E has a height of 25 nm, whereas sample F has a height of 35 nm (estimated using a QCM).

Sample	Temp. (°C)	Diameter (nm)	Area (nm^2)
A	0	50 ± 5	1400 ± 200
B	150	59 ± 10	2000 ± 600
C	300	75 ± 8	3400 ± 600
D	450	66 ± 10	2600 ± 700
E	600	50 ± 5	1600 ± 300
F	0	69 ± 7	2700 ± 500
F	150	66 ± 7	2600 ± 500
F	300	67 ± 7	2700 ± 500
F	450	65 ± 6	2700 ± 500

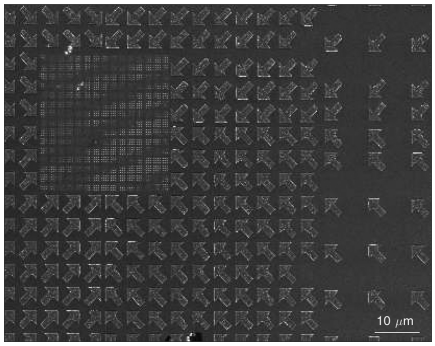

FIG. 3. SEM image of the indexed sample F, with a $30 \times 30\ \mu\text{m}^2$ area covered with gold nanoparticles with 69 nm diameter, 35 nm height, and 160 nm pitch, and surrounded by 5 μm sized arrows. Sample F is used for line profile and area analysis of specific nanoparticles using AFM and SEM. The dark stripes across the arrays are caused by the Moiré effect.

the z-direction. For nanoparticle diameter and area measurements, the SEM images were used. Our AFM instrument does not have any stage positioning mechanism, but by taking an AFM image, and pushing the sample manually with a pair of tweezers in the direction of the pointing arrows in the pattern described above, individual nanoparticles could be repeatedly located. The topographical images were analyzed using the software GWYDDION.[24] First, the images were adjusted for tilt, and then, the nanoparticle profile was investigated by line analysis, both in the vertical and horizontal directions.

SEM characterization of sample F was carried out using an acceleration voltage of 10 kV, the aperture was 30 μm, imaging was done using an InLens detector, and the contrast and brightness was kept the same for all images. Ninety nine nanoparticles were imaged, and the diameter and area of each nanoparticle was extracted using IMAGEJ. For finding the nanoparticle area, the software uses a threshold contrast to determine the edges of each nanoparticle. By counting the number of pixels within the nanoparticle, and using the correct pixel to nm^2 ratio, the area of the nanoparticle was determined. The diameter was found as a statistical average obtained by rotating the nanoparticle 360° with 2° increments. The results of the image analysis are presented in Table I.

III. RESULTS AND ANALYSIS

Figure 2 shows the macroscopically observed effect of annealing. The samples appear to turn red when annealed because more of the blue light is absorbed (the extinction peak blue-shifts). All samples A–E looked identical to the naked eye before annealing with respect to the color.

The extinction spectra for samples A–E for the different annealing steps are presented in Fig. 4(a). Sample A was not annealed, B was annealed at 50, 100, and 150 °C, C at 200, 250, and 300 °C, D at 350, 400, and 450 °C, and E at 500, 550, and 600 °C. Spectra were taken for each sample before they were annealed and are included as the top five extinction spectra in Fig. 4(a), and as the extinction peak data points at 20 °C in Fig. 4(b). The extinction peak became narrower with annealing, shrinking from 500 to 150 nm FWHM. The peak position (derived from a two term Gaussian fit) is plotted against the annealing temperature in Fig. 4(b). The uncertainty given here is the root mean square error of the Gaussian fit. As can be seen, all samples had extinction peaks between 570 and 580 nm before annealing, and the extinction peak shifted from 580 to 520 nm as the annealing temperature increased to 450 °C, followed by a light red-shift of a few nm up to 600 °C. The shift in extinction peak can be seen to be not so closely linked to the size of the nanoparticles, as the effect is very consistent, even with rather large nanoparticle size variation between 50 and 75 nm for samples A–E.

To investigate the relationship between the optical effect and the appearance of the nanoparticles, a total of 99 nanoparticles on sample F were imaged by SEM and AFM before annealing, and for annealing temperatures of 150, 300, and 450 °C. As discussed earlier, SEM and AFM imaging was done for exactly the same 99 nanoparticles. The combined AFM and SEM images allow us to obtain more information about the sample appearance. The results are presented in Fig. 5 and Table I. The technique for measuring the topographical response with the Kelvin probe is identical to that of the dynamic mode AFM. However, the additional tip bias and the fact that our sample is not grounded can result in charging effects in the image. The measured topographical response of the nanoparticles decrease from nominally 36 ± 3 to 26 ± 3 nm for annealing up to 450 °C. However, it is not certain that this is due to a true height change. It appears more likely that this is caused by a more strongly varying response in the unannealed nanoparticles, due to them being rougher. The measurements suggest that the nanoparticle surfaces get smoother with annealing and that the corners get less sharply defined, indicating a transition from the starting cylindrical shape to a more hemispherical

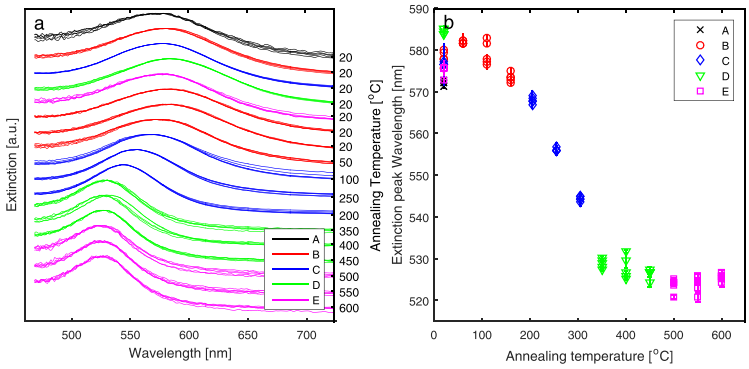

FIG. 4. (Color online) (a) Extinction spectra for gold nanoparticles samples A–E. The spectra are normalized and offset from each other for clarity. (b) Extinction peak position for gold nanoparticles done at annealing temperatures ranging up to 600 °C. As annealing temperature increases, the extinction peak blue-shifts. Macroscopically, this will cause the array to appear red because more of the blue light is absorbed.

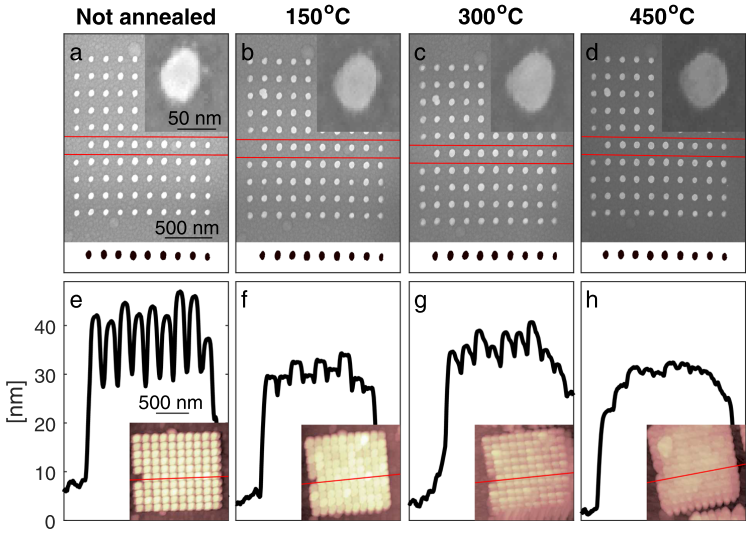

FIG. 5. (Color online) (a)–(d) SEM image of sample F gold nanpoarticles. Upper right inset shows the leftmost particle between the red lines, magnified. Bottom inset shows area analysis of nanoparticles between the red lines. (e)–(h) AFM line analysis taken over the same nanoparticles as the SEM area analysis. Inset show AFM image with red line indicating where the line profile is taken from. Images are taken before annealing [(a) and (e)], and after annealing at 150 °C [(b) and (f)], 300 °C [(c) and (g)], and 450 °C [(d) and (h)]. All the images are taken of the same nanoparticles. Note that due to the small arrays a slight dose variation can be seen (due to proximity effects), visible as a slight size variation from center to edge of the nanoparticle array.

shape. As can be seen from the SEM images and the area measurements presented in Table I, there does not appear to be a change in the area of the nanoparticles. We quantified the smoothening effect by using the SEM images to compare the perimeter length, also obtained from IMAGEJ analysis, to the circumference of a hypothetical smooth circle using an average radius calculated from the area data. We see that the surface root mean square roughness decreased from approximately 1.6 to 1.0 nm (estimation is sensitive to image resolution), a decrease of 35%, after annealing at 450 °C for the same sample. This is quantitatively in line with the predictions of Kessentini *et al.*[14] It is interesting that the effect seems to be so strong given the relatively low annealing temperatures. Considering the manufacturing process for samples A–F which would produce cylinders, it is plausible that the shape of our nanoparticles, initially cylindrical would become more hemispherical upon annealing. This would contribute to an even stronger blue-shift.[15,16]

In Fig. 1, the gold nanoparticles appear to have facets at their edges. The facets may indicate some level of crystallinity. Bosman *et al.*[7] show that annealing may increase the crystallinity of gold nanostructures, at least if it is low at first. It is not possible to say for certain if this occurs in our samples. The inset in Fig. 5(a) shows sub-10-nm particles near the edges. These particles come most likely from evaporated gold during EBE. The PMMA mask has an undercut, allowing room for stray gold to attach to the substrate near the gold particle edges. From Figs. 5(a)–5(d), we see an indication that some of these sub-10-nm particles appear to be consumed by the larger particle when annealed. This process seems to have no impact on the diameter or area of the particles (see Table I). A FDTD LUMERICAL[25] simulation of a 50 nm gold nanoparticle placed on glass with two 5 nm particles placed 5 nm from the larger nanoparticle reveals that the presence of sub-10-nm particles increases the amplitude and FWHM of the extinction peak slightly, but does not change the peak position. This is consistent with the decrease in FWHM observed in Fig. 4(a), as the sub-10-nm particles are consumed by the nanoparticle when annealed.

Karakouz *et al.*[10] reports that gold islands start sinking into a glass substrate at 550–600 °C. We observe the blue-shift in the extinction peak at lower temperatures. However, the slight red-shift occurring between 500 and 600 °C seen in Fig. 4 can potentially be attributed to this effect, as sinking into the substrate would not only change the surrounding medium, but in a sense also make the particles shorter relative to the substrate, which would cause a red-shift.[11,12] Borosilicate glass does not change refractive index significantly over the temperature range used in this experiment.[26]

IV. CONCLUSION

In this paper, we present optical measurements of gold nanoparticle arrays which change color when annealed up to 600 °C. The extinction peak blue-shifts from 580 to 520 nm already after annealing to 450 °C, after which a weak red-shift is observed. The visual appearance of the nanoparticles changes from blue to red. We conclude that the shift of 60 nm is mainly caused by two factors: first, a smoothening of the nanoparticle surface which is observed in SEM and

AFM images; second, we hypothesize a rounding of corners in the original cylindrical shape. Both of these effects would cause a blue-shift according to theoretical predictions. The final red-shift can be contributed to the nanoparticles starting to sink into the substrate. Our results demonstrate that seemingly minor changes in the metal nanoparticle appearance can lead to a strong change in the LSPR effect. We suggest that nanoparticle arrays, implanted in various devices, for example, using nanoimprint, could have potential applications for controlling the temperature product history (i.e., as a test to ensure that the temperature was never above a certain limit). The fact that the effect of temperature exposure is irreversible for these nanoparticle arrays and can be observed with the naked eye without any need of electronic readout or power supply is particularly advantageous.

ACKNOWLEDGMENTS

The authors thank Anne-Dorothea Müller, Anfatec Instruments AG for fruitful discussions. This work was carried out in the UiB Nanostructures laboratory funded by Trond Mohn, Bergen Research Foundation and the Norwegian Research Council.

[1]S. A. Maier, *Plasmonics: Fundamentals and Applications* (Springer, New York, 2007).
[2]X. Xiang, X. T. Zu, S. Zhu, C. F. Zhang, and L. M. Wang, Nucl. Instrum. Method B **250**, 229 (2006).
[3]P. Xiao-Niu, L. Min, Y. Liao, Z. Xian, and Z. Li, Chin. Phys. Lett. **25**, 4171 (2008).
[4]K. Chan, B. T. Goh, S. A. Rahman, M. R. Muhamad, C. F. Dee, and Z. Aspanut, Vacuum **86**, 1367 (2012).
[5]Z. W. Lei, M. Liu, W. Ge, Z. P. Fu, K. Reinhardt, R. J. Knize, and Y. Lu, Appl. Phys. Lett. **101**, 083903 (2012).
[6]K. Omri, A. Bettaibi, I. Najeh, S. Rabaoui, K. Khirouni, and L. El Mir, J. Mater. Sci.: Mater. Electron. **27**, 226 (2016).
[7]M. Bosman, L. Zhang, H. D. ans Shu Fen Tan, C. A. Nijhuis, C. Qiu, and J. K. W. Yang, Sci. Rep. **4**, 5537 (2014).
[8]W. Cai, H. Hofmeister, T. Rainer, and W. Chen, J. Nanopart. Res. **3**, 441 (2001).
[9]H. Bi, W. Cai, L. Zhang, D. Martin, and F. Träger, Appl. Phys. Lett. **81**, 5222 (2002).
[10]T. Karakouz, A. B. Tesler, T. A. Bendikov, A. Vaskevich, and I. Rubinstein, Adv. Mater. **20**, 3893 (2008).
[11]Y. M. Bae, K.-H. Lee, J. Yang, and D. Heo, J. Nanomater. **2014**, 175670.
[12]T. R. Jensen, M. D. Malinsky, C. L. Haynes, and R. P. Van Duyne, J. Phys. Chem. B **104**, 10549 (2000).
[13]J. C. Hulteen, C. J. Patrissi, D. L. Miner, E. R. Crosthwait, E. B. Oberhauser, and C. R. Martin, J. Phys. Chem. B **101**, 7727 (1997).
[14]S. Kessentini and D. Barchiesi, *State of the Art in Biosensors – General Aspects*, edited by Dr. T Rinken (InTech, Croatia, 2013), p. 311.
[15]J. Qian, C. Liu, W. Wang, J. Chen, Y. Li, J. Xu, and Q. Sun, Plasmonics **8**, 955 (2013).
[16]M. Liu, P. Guyot-Sionnest, T.-W. Lee, and S. K. Gray, Phys. Rev. B **76**, 235428 (2007).
[17]M. M. Greve, T. O. Håvardstun, and B. Holst, J. Vac. Sci. Technol., B **31**, 06F410 (2013).
[18]W. Rechberger, A. Hohenau, A. Leitner, J. Krenn, B. Lamprecht, and F. Aussenegg, Opt. Commun. **220**, 137 (2003).
[19]M. A. Schmidt, D. Y. Lei, L. Wondraczek, V. Nazaba, and S. A. Maier, Nat. Commun. **3**, 1108 (2012).
[20]G. Vecchi, V. Giannini, and J. Gómez Rivas, Phys Rev. B **80**, 201401(R) (2009).
[21]C. Diaz-Egea, W. Sigle, P. A. van Aken, and S. I. Molina, Nanoscale Res. Lett. **8**, 337 (2013).
[22]L. Soares, A. Csaki, J. Jatschka, W. Fritzsche, O. Flores, R. Franco, and E. Pereira, Analyst **139**, 4964 (2014).
[23]"IMAGEJ," https://imagej.nih.gov/ij/ (accessed 21 June 2016).
[24]"GWYDDION," http://gwyddion.net/ (accessed 21 June 2016).
[25]"LUMERICAL," https://www.lumerical.com/ (accessed 31 August 2016).
[26]N. Ritland, J. Am. Ceram. Soc. **39**, 403 (1956).

Part III

Appendixes and Bibliography

Appendix I
Vi er bare i startfasen

Appendix II
AFM modes

The Anfatec AFM instrument "Eddy" is used for height measurements of MNPs in article B, where it is observed that some imaging modes may remove nanoparticles which adhere poorly. The thesis defender also taught an AFM laboratory exercise for bachelor students using this instrument. For these reasons the probe-surface interaction and the different imaging modes mentioned in section 3.2 is described in more detail here.

An AFM takes images of a surface by scanning the surface with a probe. A laser is reflected on the backside of the tip and directed to a photo-detector. The deflection of the probe is recorded by the position of the laser light in the detector. The potential energy between the probe and the surface changes depending on their proximity to each other. At a distance, the tip will feel an attractive pull towards the surface (the potential is below zero). If the tip gets close enough it will start repelling the surface. Images taken with AFM contact mode (CM) operate in the region where the tip and surface is repelling each other. Changes in the surface topology will directly affect the tip-surface potential and thus the probe deflection. In dynamic mode (DM), the tip operates at a greater distance and is in the attractive regime. In this case, the tip is also excited with an oscillation, vibrating at the resonance frequency of the tip. When the topography changes, the amplitude and phase of the vibration changes. In both cases, a distance-force curve is measured in order to convert the tip deflection or the amplitude/phase data into height data.

Kelvin probe force microscopy (KPFM) is also done in the DM/attractive regime, with and oscillating tip, but in this case, a DC potential is applied to the tip. The tip and surface form a capacitor, and the oscillating tip creates an additional AC

potential. The potential V can be expressed as

$$V = (V_{DC} + V_{CPD})\, V_{AC} sin(\omega t) \tag{4.1}$$

where V_{DC} and V_{AC} are the DC and AC potentials respectively, and V_{CPD} is the contact potential difference. ω and t is the frequency and time respectively. Equation 4.1 can be used to calculate the electrostatic force $F = F_{DC} + F_{\omega}, + F_{2\omega}$. F_{DC} is used to calculate the topography, and F_{ω} can be used to calculate the work function of the surface. $F_{2\omega}$ can be used for capacitance microscopy.

Appendix III
Absorption, absorptance, absorbance

When studying the interaction between electromagnetic waves and nanostructures, some words and terms become very important. When dealing with terms like absorption, absorptance and absorbance, one wants to keep them straight. In this section we look at some terms, and evaluate the difference or relation between them. For more details on terminology and equations, see IUPAC's "Compendium of Chemical Terminology" [81] and the International Organization for Standardization catalog "ISO 9288:1989" [82], where the following information is taken from.

$$\text{Absorption} = \frac{1}{\Phi_e}\frac{d\Phi_e}{dz} \tag{4.2}$$

Absorption is the term used when the energy of a photon is taken up by matter. It is sometimes described as interchangeable with the attenuation coefficient, given in Eq. 4.2, where Φ_e is radiant power and z is the path length of the beam. This can sometimes cause confusion, since attenuation may be caused by scattering as well, in this case the term extinction would be more appropriate. Absorption has the unit m^{-1}, since the amount of light absorbed depends on the path it has traveled in a given matter.

$$\text{Absorbtance} = \frac{\Phi_e^a}{\Phi_e^i} \tag{4.3}$$

Absorptance is a measure of how effective a surface is at absorbing radiant energy, and is given as a fraction of the absorbed Φ_e^a to incident Φ_e^i light at that surface. The key word here is surface. While absorption describes how a photon might be affected while traveling through a matter, absorptance describes how it might experience the encounter with an interface.

$$\text{Absorbance} = -log\left(\frac{\Phi_e^t}{\Phi_e^i}\right) \tag{4.4}$$

Absorbance comes from the Beer-Lambert law which reads $T = \frac{\Phi_e^t}{\Phi_e^i} = e^{\tau} = 10^{-A}$, where T is transmittance, Φ_e^t and Φ_e^i is transmitted and incident radiant power, τ is optical depth and A is absorbance. It is a measure of the optical depth of a matter, but is unitless. The analogy of density might help.

The same confusion may occur between transmittance and transmission coefficients, or reflectance and reflection coefficients. Transmittance and reflectance is the ratio of transmitted and reflected radiant power to incident power respectively. The transmission and reflection coefficients are the ratio of transmitted and reflected electric fields to an incident electric field, at an interface.

When dealing with nanoparticles, as an alternative to the absorption, scattering and extinction, the coefficients β can be expressed as cross sections σ or efficiencies Q. They are related by:

$$\beta = N\sigma \tag{4.5}$$

$$Q = \frac{\sigma}{A} \tag{4.6}$$

where N is the number of particles per unit volume $N = n/V$, and A is the cross sectional area of the absorbing and/or scattering particles [72]. In this context, the concentration affects the amount of light being absorbed or scattered as well. Concentrations can be expressed by volume, by cross section or by weight:

$$f_v = n\frac{V_{np}}{V_m} \tag{4.7}$$

$$f_c = n\frac{A_{np}}{A_m} \tag{4.8}$$

$$f_w = \frac{m_{np}}{m_m} = nf_v\frac{g_{np}}{g_m} \tag{4.9}$$

where f is concentration, V is the volume, A is the area, m is the mass, g is the density with unit g/cm^3, and n is the number of particles. Subscript np is nanoparticle, m is matter and refers to the matter the nanoparticle is suspended in or resting on, v is by volume, c is by cross section, and w is by weight.

Appendix IV
Lock-in amplifier

The lock-In Amplifier (LIA) is an instrument that uses phase sensitive detection to measure small signal amplitudes buried in noise. It can detect signals buried in noise thousands of times larger. The LIA requires a reference frequency. In article D, the frequency is obtained from a chopper.

Consider a reference signal $C_r sin(\omega_r t + \phi_r)$ and a measured signal $C_s sin(\omega_s t + \phi_s)$. ω_r, ω_s, ϕ_r, ϕ_s, C_r and C_s are the reference and measured signal frequencies, phases and amplitudes respectively, and t is time. In the LIA, the two signals are multiplied to make the output C.

$$\begin{aligned} C &= C_s C_r sin(\omega_s t + \phi_s) sin(\omega_r t + \phi_r) \\ &= \frac{1}{2} C_s C_r cos([\omega_s - \omega_r]t + \phi_s - \phi_r) \\ &\quad -\frac{1}{2} C_s C_r cos([\omega_s + \omega_r]t + \phi_s + \phi_r) \end{aligned} \tag{4.10}$$

Since the reference frequency is taken from the chopper, the reference signal and the measured signal has the same frequency. Equation 4.10 is therefore reduced to a signal with a constant term $\frac{1}{2} C_s C_r cos(\phi_s - \phi_r)$ and a time varying term $\frac{1}{2} C_s C_r cos(2\omega t + \phi_s + \phi_r)$. The signal is then passed through a low pass filter eliminating the time varying term, and the phase of the reference is adjusted in the LIA, making $\phi_s - \phi_r = 0$. The only term left in the signal is then:

$$C = \frac{1}{2} C_s C_r \tag{4.11}$$

The strength of this signal treatment is that the low pass filter will only allow

frequencies very close to the reference frequency to pass through. Even when high levels of noise is introduced will neither $(\omega_{noise} - \omega_r)$ nor $(\omega_{noise} + \omega_r)$ generally be close to 0. Only noise frequencies very close to the reference will be able to pass through the filter. This is advantageous when measuring very low currents.

Three parameters are important to optimize the signal recovery. The time constant of the low pass filter and the roll-off determines the attenuation of the alternating signal. The time constant should be chosen high enough and the roll-off steep enough to give an acceptable signal-to-noise ratio. The dynamic reserve is the ratio of the largest tolerable noise signal to the full-scaled signal, and is controlled by the sensitivity/gain. The sensitivity should be chosen large enough for the analog to digital converter noise not to be a problem, but not so large that the output signal saturates [83].

Appendix V
PCI components

This appendix contains table 4.1, listing all optical and electrical components used in the University of Bergen PCI. Posts, post holders, clamps, lens and mirror mounts etc. are not included in this list. Figure 4.1 show the PCI with the components numbered according to table 4.1.

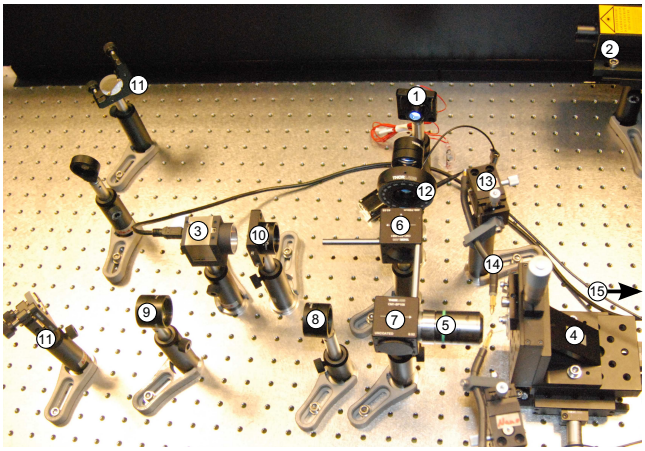

Figure 4.1: Photocurrent instrument at the University of Bergen with components numbered according to table 4.1.

nr.	equipment	name	comments
1	white light LED	Thorlabs LEDWE-15	
2	laser (temporary)	MRL-III-655	655 nm, 1W round beam
3	camera	Thorlabs DCU224C	CCD, 1280x1024, Color, USB2.0
4	xyz translation stage	Thorlabs PT3/M	Manual
5	microscope objective	Nicon plan ELWD 20X0.40	
6	beam-splitter 1	Thorlabs CM1-BP145B1	cube mounted pellicle BS 45:55 400-700 nm
7	beam-splitter 2	Thorlabs CM1-BP108	cube mounted pellicle BS 8:92 uncoated
8	lense 1	Thorlabs AC254-050-A-ML	Ø1.0", efl = 50 mm, 350-700 nm
9	lense 2	Thorlabs AC254-100-A-ML	Ø1.0", efl = 100 mm, 350-700 nm
10	lense 3	Thorlabs AC254-075-A-ML	Ø1.0", efl = 75 mm, 350-700 nm
11	mirrors	Thorlabs PF10-03-P01	Ø1.0", Protected Silver
12	polarizer	Thorlabs LPVISE100-A	400-700 nm
13	xyz mini stages	Thorlabs DT12XYZ/M	12 mm XYZ Dovetail Translation Stage
14	needle probe holder	Quater Research & Development #20601	with tungsten needle
15	source meter	Keithley 2400	

Table 4.1: University of Bergen PCI components. Lenses and beam-splitters limits the wavelength between 400 - 700 nm. Chromatic aberration should be less than 2.5% within the wavelengths of interest (resulting in $\Delta f = 1.25$ mm for a lens with f=50 mm).

Bibliography

[1] IPCC. *Climate Change 2013: The Physical Science Basis. Contribution of Working Group I to the Fifth Assessment Report of the Intergovernmental Panel on Climate Change*. Cambridge University Press, Cambridge, United Kingdom and New York, NY, USA, 2013. URL www.climatechange2013.org.

[2] Tien Ming Lee, Ezra M. Markowitz, Peter D. Howe, Chia-Ying Ko, and Anthony A. Leiserowitz. Predictors of public climate change awareness and risk perception around the world. *Nature Climate Change*, 5:1014–1020, 2015. URL http://dx.doi.org/10.1038/nclimate2728.

[3] A.K. Pandey, V.V. Tyagi, Jeyraj A/L Selvaraj, N.A. Rahim, and S.K. Tyagi. Recent advances in solar photovoltaic systems for emerging trends and advanced applications. *Renewable and Sustainable Energy Reviews*, 53(Supplement C):859–884, 2016. URL http://www.sciencedirect.com/science/article/pii/S1364032115010138.

[4] Ariana Eunjung Cha. Solar Energy Firms Leave Waste Behind in China. *Washington Post Foreign Service*, 09.03.2008. URL http://www.washingtonpost.com/wp-dyn/content/article/2008/03/08/AR2008030802595.html. Accessed 15.11.2017.

[5] Yao Zhu, Aleksandra Apostoluk, Bruno Masenelli, and Patrice Mélinon. Zinc oxide nanoparticles as luminescent down-shifting layer for solar cells. SPIE Newsroom, 2013. doi: 10.1117/2.1201212.004585.

[6] M.M. Aman, K.H. Solangi, M.S. Hossain, A. Badarudin, G.B. Jasmon, H. Mokhlis, A.H.A. Bakar, and S.N Kazi. A review of Safety, Health and Environmental (SHE) issues of solar energy system. *Renewable and*

Sustainable Energy Reviews, 41(Supplement C):1190–1204, 2015. URL http://www.sciencedirect.com/science/article/pii/S1364032114007734.

[7] Ivo Iavicoli, Veruscka Leso, Walter Ricciardi, Laura L. Hodson, and Mark D. Hoover. Opportunities and challenges of nanotechnology in the green economy. *Environmental Health*, 13(1):78, 2014. URL https://doi.org/10.1186/1476-069X-13-78.

[8] Daniel Weisser. A guide to life-cycle greenhouse gas (GHG) emissions from electric supply technologies. *Energy*, 32(9):1543–1559, 2007. URL http://www.sciencedirect.com/science/article/pii/S036054420700028X.

[9] Best Research-Cell Efficiencies. National Renewable Energy Laboratory (NREL), 2017. URL https://www.nrel.gov/pv/assets/images/efficiency-chart.png. Accessed 15.11.2017.

[10] Andrea Calatroni. Silicon cell convertible spectrum. Soluzione Solare. URL https://www.solarwind-sensor.com/wp-content/uploads/2014/04/Silicon-cell-convertible-spectrum.png. Accessed: 02.11.2017.

[11] William Shockley and Hans J. Queisser. Detailed Balance Limit of Efficiency of p-n Junction Solar Cells. *Journal of Applied Physics*, 32(3):510–519, 1961. URL https://doi.org/10.1063/1.1736034.

[12] Phil Denby. Photovoltaic cell. Patent number AU20100235273, 10.11.2011. URL http://worldwide.espacenet.com/publicationDetails/biblio?CC=AU&NR=2010235273A1&KC=A1&FT=D&ND=3&date=20111110&DB=worldwide.espacenet.com&locale=en_EP.

[13] Vårin R.A. Holm, Martin M. Greve, and Bodil Holst. A theoretical investigation of the optical properties of metal nanoparticles in water for photo thermal conversion enhancement. *Energy Conversion and Management*, 149:536 – 542, 2017. URL http://www.sciencedirect.com/science/article/pii/S0196890417306623.

[14] Vårin R. A. Holm, Martin M. Greve, and Bodil Holst. Temperature induced color change in gold nanoparticle arrays: Investigating the annealing effect on the localized surface plasmon resonance. *Journal of Vacuum Science & Technology B, Nanotechnology and Microelectronics: Materials, Processing, Measurement, and Phenomena*, 34(6):06K501, 2016. URL http://dx.doi.org/10.1116/1.4963153.

[15] Ranveig Flatabø, Vårin R. A. Holm, Håkon Eidsvåg, Bodil Holst, and Martin M. Greve. Light absorption and scattering of 40-170 nm gold nanoparticles on glass substrates. *Journal of Vacuum Science & Technology B, Nanotechnology and Microelectronics: Materials, Processing, Measurement, and Phenomena*, 35(6):06G403, 2017. URL https://doi.org/10.1116/1.4994113.

[16] Naureen Akhtar, Vårin R. A. Holm, Peter J. Thomas, Benny Svardal, Simen H. Askeland, and Bodil Holst. Underwater Superoleophobic Sapphire (0001) Surfaces. *The Journal of Physical Chemistry C*, 119(27):15333–15338, 2015. URL http://dx.doi.org/10.1021/acs.jpcc.5b03741.

[17] Vårin R. A. Holm. Vi er bare i startfasen. *Bergens Tidene*, 16.07.2017. URL https://www.bt.no/btmeninger/debatt/i/bVWLe/Nanoteknologi-er-fremtiden. Accessed: 2017-08-03.

[18] Siu-Fung Leung, Qianpeng Zhang, Mohammad Mahdi Tavakoli, Jin He, Xiaoliang Mo, and Zhiyong Fan. Progress and Design Concerns of Nanostructured Solar Energy Harvesting Devices. *Small*, 12(19):2536–2548, 2016. URL http://dx.doi.org/10.1002/smll.201502015.

[19] Harry A. Atwater and Albert Polman. Plasmonics for improved photovoltaic devices. *Nature Materials*, 9:205–213, 2010. URL https://www.nature.com/nmat/journal/v9/n3/full/nmat2629.html.

[20] D. M. Schaadt, B. Feng, and E. T. Yu. Enhanced semiconductor optical absorption via surface plasmon excitation in metal nanoparticles. *Applied Physics Letters*, 86(6):063106, 2005. URL http://dx.doi.org/10.1063/1.1855423.

[21] D. Derkacs, S. H. Lim, P. Matheu, W. Mar, and E. T. Yu. Improved performance of amorphous silicon solar cells via scattering from surface plasmon polaritons in nearby metallic nanoparticles. *Applied Physics Letters*, 89(9):093103, 2006. URL http://dx.doi.org/10.1063/1.2336629.

[22] P. Matheu, S. H. Lim, D. Derkacs, C. McPheeters, and E. T. Yu. Metal and dielectric nanoparticle scattering for improved optical absorption in photovoltaic devices. *Applied Physics Letters*, 93(11):113108, 2008. URL http://dx.doi.org/10.1063/1.2957980.

[23] Anthony J. Morfa, Kathy L. Rowlen, Thomas H. Reilly III, Manuel J. Romero, and Jao van de Lagemaat. Plasmon-enhanced solar energy conversion in organic bulk heterojunction photovoltaics. *Applied Physics Letters*, 92(1):013504, 2008. URL http://aip.scitation.org/doi/abs/10.1063/1.2823578.

[24] R. B. Konda, R. Mundle, H. Mustafa, O. Bamiduro, A. K. Pradhan, U. N. Roy, Y. Cui, and A. Burger. Surface plasmon excitation via Au nanoparticles in n-CdSe/p-Si heterojunction diodes. *Applied Physics Letters*, 91 (19):191111, 2007. URL http://dx.doi.org/10.1063/1.2807277.

[25] M. Kirkengen, J. Bergli, and Y. M. Galperin. Direct generation of charge carriers in c-Si solar cells due to embedded nanoparticles. *Journal of Applied Physics*, 102(9):093713, 2007. URL http://dx.doi.org/10.1063/1.2809368.

[26] Vivian E. Ferry, Marc A. Verschuuren, Hongbo B. T. Li, Ruud E. I. Schropp, Harry A. Atwater, and Albert Polman. Improved red-response in thin film a-Si:H solar cells with soft-imprinted plasmonic back reflectors. *Applied Physics Letters*, 95(18):183503, 2009. URL http://dx.doi.org/10.1063/1.3256187.

[27] Chuan F. Guo, Tianyi Sun, Feng Cao, Qian Liu, and Zhifeng Ren. Metallic nanostructures for light trapping in energy-harvesting devices. *Light: Science & Applications*, 3, 2014. URL http://www.nature.com/lsa/journal/v3/n4/full/lsa201442a.html.

[28] Boris Luk'yanchuk, Nikolay I. Zheludev, Stefan A. Maier, Naomi J. Halas, Peter Nordlander, Harald Giessen, and Chong Tow Chong. The Fano resonance in plasmonic nanostructures and metamaterials. *Nat Mater*, 9(9): 707–715, 2010. URL http://dx.doi.org/10.1038/nmat2810.

[29] S. Krishnan, H. La Rosa, E. Stefanakos, S. Bhansali, and K. Buckle. Design and development of batch fabricatable metal-insulator-metal diode and microstrip slot antenna as rectenna elements. *Sensors and Actuators A: Physical*, 142(1):40–47, 2008. URL http://www.sciencedirect.com/science/article/pii/S0924424707002373.

[30] Xianliang Liu, Tatiana Starr, Anthony F. Starr, and Willie J. Padilla. Infrared Spatial and Frequency Selective Metamaterial with Near-Unity Absorbance. *Phys. Rev. Lett.*, 104:207403, 2010. URL https://link.aps.org/doi/10.1103/PhysRevLett.104.207403.

[31] Takayuki Okamoto and Ichirou Yamaguchi. Optical Absorption Study of the Surface Plasmon Resonance in Gold Nanoparticles Immobilized onto a Gold Substrate by Self-Assembly Technique. *The Journal of Physical Chemistry B*, 107(38):10321–10324, 2003. URL http://dx.doi.org/10.1021/jp034537l.

[32] W. C. Brown. The History of Power Transmission by Radio Waves. *IEEE Transactions on Microwave Theory and Techniques*, 32(9):1230–1242, 1984. ISSN 0018-9480.

[33] Matthew L. Chin, Prakash Periasamy, Terrance P. O'Regan, Matin Amani, Cheng Tan, Ryan P. O'Hayre, Joseph J. Berry, Richard M. Osgood III, Philip A. Parilla, David S. Ginley, and Madan Dubey. Planar metal-insulator-metal diodes based on the Nb/Nb2O5/X material system. *Journal of Vacuum Science & Technology B, Nanotechnology and Microelectronics: Materials, Processing, Measurement, and Phenomena*, 31(5):051204, 2013. URL https://doi.org/10.1116/1.4818313.

[34] Fatih B. Atar, Enes Battal, Levent E. Aygun, Bihter Daglar, Mehmet Bayindir, and Ali K. Okyay. Plasmonically enhanced hot electron based photovoltaic device. *Opt. Express*, 21(6):7196–7201, 2013. URL http://www.opticsexpress.org/abstract.cfm?URI=oe-21-6-7196.

[35] Koray Aydin, Vivian E. Ferry, Ryan M. Briggs, and Harry A. Atwater. Broadband polarization-independent resonant light absorption using ultrathin plasmonic super absorbers. *Nature Communications*, 2:517, 2011. URL http://dx.doi.org/10.1038/ncomms1528.

[36] Hamidreza Chalabi, David Schoen, and Mark L. Brongersma. Hot-Electron Photodetection with a Plasmonic Nanostripe Antenna. *Nano Letters*, 14(3): 1374–1380, 2014. URL http://dx.doi.org/10.1021/nl4044373.

[37] Fuming Wang and Nicholas A. Melosh. Plasmonic Energy Collection through Hot Carrier Extraction. *Nano Letters*, 11(12):5426–5430, 2011. URL http://dx.doi.org/10.1021/nl203196z.

[38] Prakash Periasamy, Joseph J. Berry, Arrelaine A. Dameron, Jeremy D. Bergeson, David S. Ginley, Ryan P. O'Hayre, and Philip A. Parilla. Fabrication and Characterization of MIM Diodes Based on Nb/Nb2O5 Via a Rapid Screening Technique. *Advanced Materials*, 23(27):3080–3085, 2011. URL http://dx.doi.org/10.1002/adma.201101115.

[39] Changhwan Lee, Ievgen I Nedrygailov, Young Keun Lee, Changui Ahn, Hyosun Lee, Seokwoo Jeon, and Jeong Young Park. Amplification of hot electron flow by the surface plasmon effect on metal-insulator-metal nanodiodes. *Nanotechnology*, 26(44):445201, 2015. URL http://stacks.iop.org/0957-4484/26/i=44/a=445201.

[40] S. Linden, J. Kuhl, and H. Giessen. Controlling the Interaction between Light and Gold Nanoparticles: Selective Suppression of Extinction. *Phys. Rev. Lett.*, 86:4688–4691, 2001. URL https://link.aps.org/doi/10.1103/PhysRevLett.86.4688.

[41] Martin M. Greve, Thomas O. Håvardstun, and Bodil Holst. Measuring the localized surface plasmon resonance effect on large arrays (5 mm x 5 mm) of gold and aluminum nanoparticles on borosilicate glass substrates, fabricated by electron beam lithography. *Journal of Vacuum Science & Technology B, Nanotechnology and Microelectronics: Materials, Processing, Measurement, and Phenomena*, 31(6):06F410, 2013. URL https://doi.org/10.1116/1.4831772.

[42] Mark L. Brongersma, Naomi J. Halas, and Peter Nordlander. Plasmon-induced hot carrier science and technology. *Nature Nanotechnology*, 10:25, 2015. URL http://dx.doi.org/10.1038/nnano.2014.311.

[43] Cesar Clavero. Plasmon-induced hot-electron generation at nanoparticle/metal-oxide interfaces for photovoltaic and photocatalytic devices. *Nature Photonics*, 8:95–103, 2014. URL http://dx.doi.org/10.1038/nphoton.2013.238.

[44] Cláudia Gomes Silva, Raquel Juárez, Tiziana Marino, Raffaele Molinari, and Hermenegildo García. Influence of Excitation Wavelength (UV or Visible Light) on the Photocatalytic Activity of Titania Containing Gold Nanoparticles for the Generation of Hydrogen or Oxygen from Water. *Journal of the American Chemical Society*, 133(3):595–602, 2011. URL http://dx.doi.org/10.1021/ja1086358.

[45] Isabell Thomann, Blaise A. Pinaud, Zhebo Chen, Bruce M. Clemens, Thomas F. Jaramillo, and Mark L. Brongersma. Plasmon Enhanced Solar-to-Fuel Energy Conversion. *Nano Letters*, 11(8):3440–3446, 2011. URL http://dx.doi.org/10.1021/nl201908s.

[46] Shaunak Mukherjee, Linan Zhou, Amanda M. Goodman, Nicolas Large, Ciceron Ayala-Orozco, Yu Zhang, Peter Nordlander, and Naomi J. Halas. Hot-Electron-Induced Dissociation of H2 on Gold Nanoparticles Supported on SiO2. *Journal of the American Chemical Society*, 136(1):64–67, 2014. URL http://dx.doi.org/10.1021/ja411017b.

[47] Mark W. Knight, Heidar Sobhani, Peter Nordlander, and Naomi J. Halas. Photodetection with Active Optical Antennas. *Science*, 332(6030):702–704, 2011. URL http://science.sciencemag.org/content/332/6030/702.

[48] Christophe Voisin, Natalia Del Fatti, Dimitris Christofilos, and Fabrice Vallée. Ultrafast Electron Dynamics and Optical Nonlinearities in Metal Nanoparticles. *The Journal of Physical Chemistry B*, 105(12):2264–2280, 2001. URL http://dx.doi.org/10.1021/jp0038153.

[49] Alejandro Manjavacas, Jun G. Liu, Vikram Kulkarni, and Peter Nordlander. Plasmon-Induced Hot Carriers in Metallic Nanoparticles. *ACS Nano*, 8(8): 7630–7638, 2014. URL http://dx.doi.org/10.1021/nn502445f.

[50] Werner Weiss, Monika Spörk-Dur, and Franz Mauthner. Solar Heat Worldwide, Global Market Development and Trends in 2016 | Detailed Market Figures 2015. Solar Heating & Cooling Programme, International Energy Agency, 2017. URL http://www.iea-shc.org/solar-heat-worldwide. Accessed: 08.12.2017.

[51] H. G. Craighead and R. A. Buhrman. Optical properties of selectively absorbing Ni/Al2O3 composite films. *Applied Physics Letters*, 31(7):423–425, 1977. URL http://dx.doi.org/10.1063/1.89732.

[52] Harish C. Barshilia, N. Selvakumar, G. Vignesh, K.S. Rajam, and A. Biswas. Optical properties and thermal stability of pulsed-sputter-deposited AlxOy/Al/AlxOy multilayer absorber coatings. *Solar Energy Materials and Solar Cells*, 93(3):315–323, 2009. URL http://www.sciencedirect.com/science/article/pii/S0927024808004005.

[53] Manuel Romero and Aldo Steinfeld. Concentrating solar thermal power and thermochemical fuels. *Energy Environ. Sci.*, 5:9234–9245, 2012. URL http://dx.doi.org/10.1039/C2EE21275G.

[54] Pawel Keblinski, Jeffrey A. Eastman, and David G. Cahill. Nanofluids for thermal transport. *Materials Today*, 8(6):36–44, 2005. URL http://www.sciencedirect.com/science/article/pii/S1369702105709366.

[55] Xiang-Qi Wang and Arun S. Mujumdar. Heat transfer characteristics of nanofluids: a review. *International Journal of Thermal Sciences*, 46(1):1–19, 2007. URL http://www.sciencedirect.com/science/article/pii/S1290072906001190.

[56] Meijie Chen, Yurong He, Jiaqi Zhu, and Dong Rip Kim. Enhancement of photo-thermal conversion using gold nanofluids with different particle sizes. *Energy Conversion and Management*, 112:21–30, 2016. URL http://www.sciencedirect.com/science/article/pii/S019689041600025X.

[57] J. Sun and S. L. Simon. The melting behavior of aluminum nanoparticles. *Thermochimica Acta*, 463(1):32–40, 2007. URL http://www.sciencedirect.com/science/article/pii/S004060310700278X.

[58] Michel Bosman, Lei Zhang, Huigao Duan, Shu Fen Tan, Christian A. Nijhuis, Cheng-Wei Qiu, and Joel K. W. Yang. Encapsulated Annealing:

Enhancing the Plasmon Quality Factor in Lithographically-Defined Nanostructures. *Scientific Reports*, 4:5537, 2014. URL http://dx.doi.org/10.1038/srep05537.

[59] Stefan Alexander Maier. *Plasmonics: fundamentals and applications*. Springer, 2007. ISBN 0-387-33150-6.

[60] Anfatec. AFM "Eddy". URL http://www.anfatec.de/anfatec/eddy/eddy.html. Accessed: 2017-02-01.

[61] Collector's corner: Mohs' scale of hardness. Mineralogical Society of America. URL http://www.minsocam.org/MSA/collectors_corner/article/mohs.htm. Accessed: 2017-11-03.

[62] Kiran Kishore Kumar Annamdas and Venu Gopal Annamdas. Review on Developments in Fiber Optical Sensors and Applications. *Proceedings of SPIE*, 7677:76770R, 2010. doi: 10.1117/12.849799.

[63] Mike Crabtree, David Eslinger, Phil Fletcher, Matt Miller, Ashley Johnson, and George King. Fighting Scale: Removal and Prevention. *Oilfield Review*, 11(3), 1999. URL https://www.slb.com/resources/publications/industry_articles/oilfield_review/1999/or1999aut03_fighting_scale_removal.aspx.

[64] Lukas Novotny and Bert Hecht. *Principles of Nano-Optics*. Cambridge University Press, Jun 2006. URL https://www.cambridge.org/core/books/principles-of-nano-optics/EAA3E0D04179A7252088E27483C4ACC1.

[65] Sergey V. Gaponenko. *Introduction to Nanophotonics*. Cambridge University Press, 2010. ISBN 9780521763752.

[66] The British Museum. Lycurgus cup. URL http://www.britishmuseum.org/research/collection_online/collection_object_details.aspx?objectId=61219&partId=1&searchText=lycurgus+cup&page=1. Accessed: 2017-09-19.

[67] Hon. J.W. Strutt. XV. On the light from the sky, its polarization and colour. *Philosophical Magazine*, 41(271):107–120, 1871. URL http://www.tandfonline.com/doi/abs/10.1080/14786447108640452.

[68] Gustav Mie. Beiträge zur Optik trüber Medien, speziell kolloidaler Metallösungen. *Annalen der Physik*, 25:377–445, 1908.

[69] D. Pines. Collective Energy Losses in Solids. *Reviews of Modern Physics*, 28: 184–198, 1956. URL http://adsabs.harvard.edu/abs/1956RvMP...28..184P.

[70] Uwe Kreibig and Peter Zacharias. Surface plasma resonances in small spherical silver and gold particles. *Zeitschrift für Physik A Hadrons and nuclei*, 231(2):128–143, 1970. URL https://doi.org/10.1007/BF01392504.

[71] A. W. Murray and W. L. Barnes. Plasmonic materials. *Advanced Materials*, 19:3771–3782, 2007. URL http://dx.doi.org/10.1002/adma.200700678.

[72] Craig F. Bohren and Donald R. Huffman. *Absorption and Scattering of Light by Small Particles*. Wiley-VCH Verlag GmbH, 1983. URL http://dx.doi.org/10.1002/9783527618156.ch11.

[73] Maxim Sukharev. Software&Computing: Physics of nano-optics spur sophisticated models, 2011. URL http://www.laserfocusworld.com/articles/2011/05/software-computing-physics-of-nano-optics-spur-sophisticated-models.html. Accessed 26.07.2017.

[74] Roger F. Harrington. *Field Computation by Moment Methods*. Wiley-IEEE Press, 1993. ISBN 0780310144.

[75] A. Ruehli. Partial element equivalent circuit (PEEC) method and its application in the frequency and time domain. In *Proceedings of Symposium on Electromagnetic Compatibility*, pages 128–133, 1996.

[76] Daryl L. Logan. *A First Course in the Finite Element Method Using Algor*. Brooks/Cole Publishing Co., Pacific Grove, CA, USA, 2nd edition, 2000. ISBN 0534380689.

[77] Allen Taflove and Susan C. Hagness. *Computational Electrodynamics: The Finite-Difference Time-Domain Method, 3rd edition*, volume 2062. Artech House, Inc., 2005. ISBN 978-1-58053-832-9.

[78] Lumerical Inc. https://www.lumerical.com/. Accessed: 2016-08-31.

[79] COMSOL Multiphysics® Modeling Software. URL https://www.comsol.com/. Accessed: 2017-09-28.

[80] Martin M. Greve and Bodil Holst. Optimization of an electron beam lithography instrument for fast, large area writing at 10 kV acceleration voltage. *Journal of Vacuum Science & Technology B, Nanotechnology and Microelectronics: Materials, Processing, Measurement, and Phenomena*, 31(4): 043202, 2013. URL https://doi.org/10.1116/1.4813325.

[81] A. D. Mcnaught and A. Wilkinson. *IUPAC. Compendium of Chemical Terminology, 2nd ed. (the "Gold Book")*. WileyBlackwell, 1997. URL http://goldbook.iupac.org/.

[82] International Organization for Standardization. Thermal insulation - Heat transfer by radiation - Physical quantities and definitions. ISO catalogue, 1989. URL https://www.iso.org/obp/ui/#iso:std:16943:en.

[83] Vårin Renate Andvik Holm. Detection of CO_2 in N_2 and H_2O using photoacoustics. Master's thesis, University of Bergen, Allégaten 55, 5007 Bergen, Norway, 2013. URL https://bora.uib.no/handle/1956/7510.

Graphic design: Communication Division, UiB / Print: Skipnes Kommunikasjon AS

uib.no

ISBN: 978-82-308-3814-3